THE UNIVERSITY OF CHICAGO

DOMAIN WALL DYNAMICS AND MANY-BODY ECHO IN DRIVEN BOSE EINSTEIN CONDENSATES

A DISSERTATION SUBMITTED TO
THE FACULTY OF THE DIVISION OF THE PHYSICAL SCIENCES
IN CANDIDACY FOR THE DEGREE OF
DOCTOR OF PHILOSOPHY

DEPARTMENT OF PHYSICS

BY
KAI-XUAN YAO

CHICAGO, ILLINOIS
MARCH 2023

To my family

TABLE OF CONTENTS

LIST OF FIGURES

LIST OF TABLES

ACKNOWLEDGMENTS

I would like to thank my advisor, Professor Cheng Chin. His guidance, mentoring, inspiration and support are indispensable in my growth during my PhD study throughout the years. His intuition and methodology towards problem solving have been most enlightening to me, even beyond physics research. His passion towards research and his students is a beacon I shall always look up to.

I would like to thank my lab mate, Dr. Zhendong Zhang. Throughout my time in the Cs lab we have worked together on the experiment, and we would not have kept the experiment running so smoothly and been so productive without his diligence, passion and expertise. We also had many inspiring discussions about our projects and new ideas.

When I first joined the group I started in the quantum matter synthesizer experiment working with Dr. Mickey McDonald and Jonathan Trisnadi. I thank Mickey and Jon for their support and guidance when I first started my journey as an experimentalist, and for the cheerful atmosphere they create in the lab. They showed me the fun in working on experiments as a team. I also thank Drs. Brian DeSalvo, Lei Feng and Krutik Patel, for welcoming me into the group and their help and support throughout the years.

I thank newer members of the Cs lab, Shu Nagata and Jay Jachinowski, for carrying on the amazing research with passion and curiosity. I thank Lauren Weiss, Aditi Goyal, Callum Welsh and Nick Li for our collaboration on the entangled photon source project. Their devotion is essential in our exploration of a technique new to our lab, and they made my first time taking on an supervisory role an enjoyable and educational experience. I thank Henry Ando for taking over my duties as webmaster and setting up an amazing new website. I thank Geyue Cai, Mingjiamei Zhang and the rest of the Chin lab, as well as visiting members throughout the years, for making Chin lab an amazing place to learn and work.

I thank our collaborators Professor Kathryn Levin and Dr. Han Fu, for offering new perspective into our experiments with theoretical and numerical approaches.

Finally I would like to thank my family for their care and love, and their steadfast support during my PhD study and my entire life.

ABSTRACT

Ultracold atoms provide a versatile platform for quantum simulation, offering a great deal of control on system parameters. The potential landscape experienced by the atoms can be precisely controlled with the optical dipole force, especially with the help of a digital micromirror device (DMD). The kinetic property of the atoms can be altered with optical lattices that create band structures with tunable dispersion. The interatomic interaction can also be controlled by magnetic field through Feshbach resonances. One popular method to leverage this high degree of tunability is Floquet engineering, where one periodically drives the system to realize Hamiltonians inaccessible to static systems. On the other hand, Bose-Einstein condensates provide a scalable and clean venue to study many-body physics, where tens of thousands of atoms share the same quantum state while interacting with each other.

With driven Bose-Einstein condensates, we study two novel many-body phenomena. First, we create domain walls in the condensate, which are stable topological defects that behave as emergent particle-like excitations. The domain walls are found to display emergent dynamical properties drastically different from the constituent atoms. Second, we study the time reversal of a many-body system coupled to a continuum. The dynamics of such systems typically exhibit rapidly growing subsystem entropy, which according to classical thermodynamics appears irreversible. We are able to achieve significant reversal of the complex many-body dynamics by devising a technique inspired by the famous 'spin echo', which we call the 'many-body echo'. Our work addresses two major standing questions in quantum many-body physics: emergence and thermalization.

CHAPTER 1

INTRODUCTION

The quantum world is mysterious. At microscopic scales, each particle behaves as an ensemble of many. Even more mysterious is when many quantum particles come together and interact. Quantum many-body physics is notoriously difficult to tackle, primarily due to the exponentially large space of states as the system size grows, manifesting as large scale entanglement. Computational efforts are thus generally limited to prohibitively small system sizes. As an alternative approach, quantum simulation aims to simulate one quantum system with another one, where we have better control and detection tools. Ultracold atoms offer an ideal platform for quantum simulation, thanks to the expansive toolbox developed over the past three decades. We have learned to manipulate atoms using lasers and magnetic fields, not just their internal state, but their motional degrees of freedom, and even inter-particle interaction. Time-dependent driving provides further flexibility in controlling the system, allowing the creation of exotic Hamiltonians otherwise inaccessible through Floquet engineering. Over the years, ultracold atom quantum simulators have simulated a wide range of topics, including Abrikosov lattice of superfluid vortices [1], topological physics of solids in extreme magnetic fields [2], lattice gauge theory [3] and quantum turbulence [4].

Ultracold bosonic atoms, such as ^{133}Cs used in our experiments, form a Bose-Einstein condensate (BEC) at low enough temperatures [5]. In a BEC, a macroscopic number of atoms occupy the same quantum state, providing a particularly pristine environment for studying quantum many-body physics. The particle number can reach 50,000 in our systems, whereas defects and decoherence are suppressed since all atoms occupy the same quantum state. In this thesis, we use driven BECs to study two general quantum many-body phenomena: emergence and thermalization. We create domain walls in our BEC, which are topological defects, and find that they display emergent dynamical properties distinct from that of the constituent atoms. We also study 'many-body echo', time reversal of quantum many-body

dynamics, and find that quantum excitation that appear to be thermal can be reversed, demonstrating the reversibility of thermalization in the quantum world.

This thesis is structured as follows. In chapter 2, we describe the experimental system, including the general setup for preparing ultracold ^{133}Cs BECs, experimental implementation of control on the atoms, and some details on collecting and extracting information from the system. In chapter 3, we discuss the necessary theoretical and numerical background knowledge for describing and understanding our experiments, as well as original analytical derivations related to the experiments. In Chapter 4, we experimentally study the dynamics of domain walls in a BEC driven by density-dependent gauge field. We find that the domain walls, which are topological defects that behave as elementary excitations, exhibit drastically different properties from that of the constituent atoms, a manifestation of emergence. In Chapter 5, we study the time reversal of many-body quantum dynamics. We propose and implement a new scheme called 'many-body echo' which significantly improves the efficiency of reversal of Bose fireworks dynamics. The experiment realizes an instance of Loschmidt echo, which connects the reversal of quantum many-body dynamics to concepts such as chaos. We also utilize the many-body echo to realize a multi-mode SU(1,1) interferometer. In Chapter 6, we present theoretical derivations and analysis procedures which contribute to other projects in the lab, as well as theoretical investigations into new proposals. Finally, in Chapter 7, we present an outlook of future directions of quantum simulation using our driven BEC experiment platform.

CHAPTER 2

SYSTEM

2.1 General setup

Our experiments are performed on Bose-Einstein condensates of ^{133}Cs atoms. Atomic vapor in the vacuum chamber is collected, trapped and cooled with a Zeeman slower and a three dimensional (3D) magneto-opticla trap (MOT). The MOT produces ∼40 million atoms at a temperature of ∼10 mK after 3 seconds of loading. The atoms are further cooled with degenerate Raman sideband cooling (dRSC) to ∼1.5 μK, with a typical atom number of 8 million. Afterwards, the atoms are trapped in a crossed 1064 nm dipole trap and evaporatively cooled deep into degeneracy by ramping down the levitating magnetic gradient, which reduces the trap depth. We end up with an almost pure Bose-Einstein condensate of ∼50,000 atoms at a temperature of ∼10 nK.

After producing the condensate in the crossed diple trap, we adiabatically load it into a vertical lattice with a lattice spacing of ∼4 μm formed by two 1064 nm laser beams at a shallow angle. The condensate is shaped carefully in the vertical direction such that it is loaded into the ground state in a single site of the vertical lattice. This setup allows as to have a much higher trap frequency in the vertical direction than in the horizontal plane, allowing us to restrict the dynamics in the vertical direction. We then adiabatically transfer the condensate to optical traps of the desired final configuration, for example a 2D harmonic trap or a box trap. The box trap is formed by a ring of 780 nm blue detuned light projected by a digital micromirror device (DMD) through a high numerical aperture (NA) microscope objective, allowing us to prepare a condensate with uniform density in the horizontal plane. A diagram of the optical setup that produces the trapping potentials is shown in Fig. 2.1.

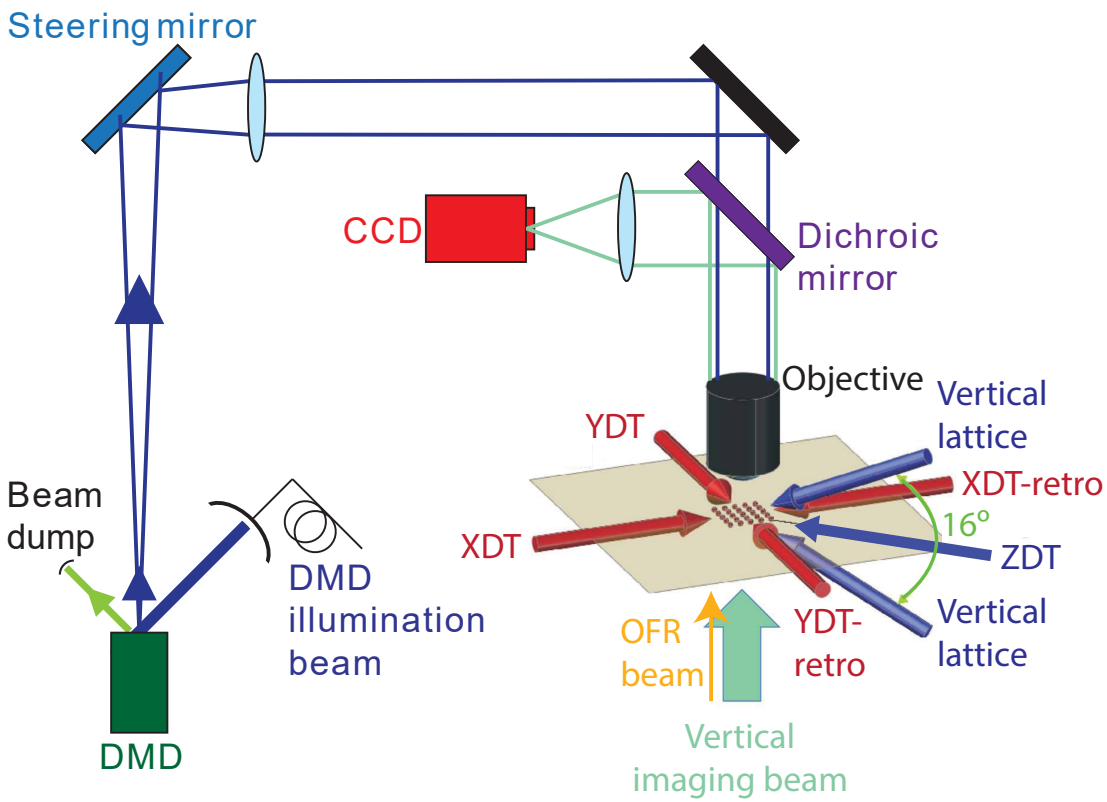

Figure 2.1: **Optical setup of the experiment.** The diagram shows the optical paths of beams used to trap the atoms. The 'OFR beam' is no longer used in this work. This figure is reproduced from [6].

2.2 Controlling the atomic interaction

In ultracold atom experiments, Feshbach resonances allow us to tune the interaction strength between atoms by controlling the magnetic field [7]. At ultracold temperatures, atoms primarily interact through $s-$wave scattering, with strength characterized by the scattering length. A positive scattering length means repulsive interaction, and negative means attractive, with zero scattering length meaning non-interacting. The atomic species we use, ^{133}Cs, has particularly convenient Feshbach resonances. We perform the experiments with magnetic field near 17.2 G, where the scattering length crosses zero. A low scattering length allow for low chemical potential for the condensate even at high densities. Applying an oscillating magnetic field allows us to modulate the scattering length, and we can achieve modulation

amplitudes much larger than the time-average, meaning the interaction alternates between repulsive and attractive.

2.3 Optical lattice

We have the capability create a 2D square optical lattice by retroreflecting two perpendicular 1064 nm diple trap beams. In our experiments we only retroreflect one of the beams to form a 1D lattice. The lattice spacing is 532 nm. The retroreflected beam double-passes two acoustic-optical modulators (AOMs), which allows us to control the phase of the retroreflected beam through the phase of the radio-frequency (RF) signal sent to the AOMs, and in turn control the displacement of the lattice. The intensity of the RF signal also controls the lattice depth. We can phase modulate (PM) the RF signal to modulate the lattice displacement, which forms the basis of our shaken lattice experiments.

The lattice depth is experimentally calibrated by jumping the lattice displacement to excite the BEC to the first excited band. The interference of different band eigenstates results in an oscillation in the strength of Bragg diffraction orders, which allows us to measure the transition frequency between the ground and first excited bands at zero momentum. This band oscillation frequency corresponds uniquely to a lattice depth, which can be obtained from lattice band calculations. An example is shown in Fig. 2.2.

Another effect of turning on the retroreflected beam to form the optical lattice is a shift in the trap center. This is because our lattice is red detuned, and the constructive interference causes the trap potential at the lattice sites to be deeper than without the retroreflected beam. Since our trap center results from the balance of several dipole trap beams as well as the magnetic potential, the trap center moves as a function of the retroreflected beam intensity.

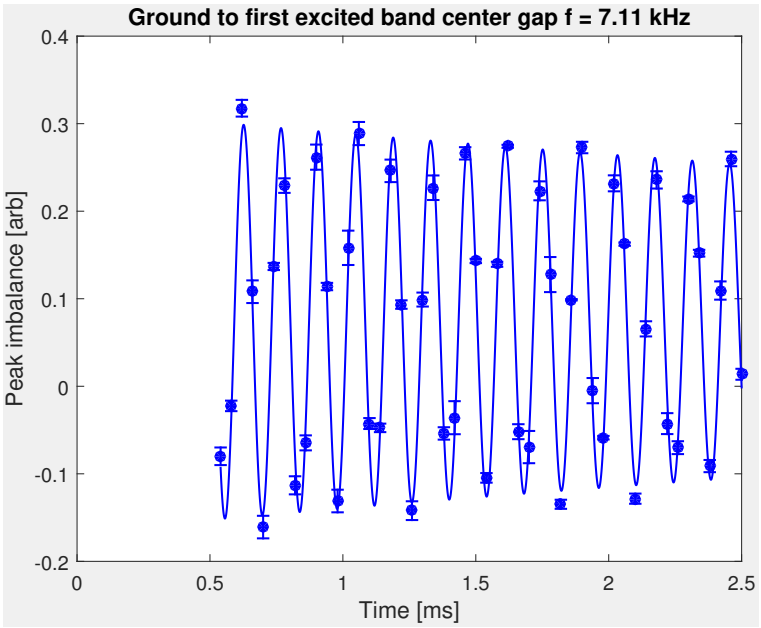

Figure 2.2: **Calibration of the optical lattice depth.** The band oscillation frequency of 7.11 kHz implies a lattice depth of 8.77 E_R, where $E_R = h \times 1326$ Hz is the recoil energy of the 532 nm lattice.

2.4 Imaging and detection

2.4.1 Absorption imaging of atomic density

The primary form of data in our experiments is absorption images of the atomic density. We shine a beam of coherent light resonant with the atomic cycling transition $|F = 4, m_F = 5\rangle \rightarrow |F' = 4, m_{F'} = 5\rangle$, with high intensity compared to the saturation intensity I_{sat} [8]. The atoms during the experiment reside in the state $|F = 3, m_F = 3\rangle$. Therefore, before imaging the atoms are optically pumped into the bright state.

The atoms absorb the resonant light and cast a shadow, which is collected by a high NA objective with NA = 0.5. The atomic density n, column integrated along the imaging beam, is obtained from the collected light intensity with (I_{in}) and without (I_{out}) atoms as [9]

$$n\sigma_0 = -\ln \frac{I_{out}}{I_{in}} + \frac{I_{in} - I_{out}}{I_{sat}}, \tag{2.1}$$

where σ_0 is the resonant scattering cross section.

2.4.2 Heterodyne detection of matter-wave

In our experiments, we often create two-mode squeezed states in the atomic momentum modes. An important observable is the quadrature of the bosonic modes. If the condensate is uniform, the *in situ* atomic density profile provides a heterodyne detection of the atomic modes, since the excited atoms interfere with the condensate and form density waves.

The structure factor is defined from the *in situ* density as

$$\begin{aligned} \hat{S}_{\mathbf{k}} &= N^{-1} \int d\mathbf{r}_1 d\mathbf{r}_2 e^{-i\mathbf{k}(\mathbf{r}_1-\mathbf{r}_2)} \hat{n}(\mathbf{r}_1)\hat{n}(\mathbf{r}_2) \\ &= N^{-1} |\hat{A}_{\mathbf{k}}|^2, \end{aligned} \tag{2.2}$$

where N is the total atom number and $\hat{A}_{\mathbf{k}} = \int d\mathbf{r}\hat{n}(\mathbf{r})e^{-i\mathbf{kr}}$ is the Fourier transform of density. The density is given by the operator

$$\hat{n}(\mathbf{r}) = a^\dagger(\mathbf{r})a(\mathbf{r}), \tag{2.3}$$

where $a(\mathbf{r})$ is the annihilation operator at position $\mathbf{r}$. The real space annihilation operator can be expressed by the momentum space operators $a_{\mathbf{k}}$ as

$$a(\mathbf{r}) = \int d\mathbf{k} a_{\mathbf{k}} e^{i\mathbf{kr}}. \tag{2.4}$$

Substituting in, we have

$$\begin{aligned} \hat{A}_{\mathbf{k}} &= \int d\mathbf{r} d\mathbf{k}_1 d\mathbf{k}_2 e^{i(\mathbf{k}_1-\mathbf{k}_2-\mathbf{k})\mathbf{r}} a^\dagger_{\mathbf{k}_2} a_{\mathbf{k}_1} \\ &= \int d\mathbf{k}_2 a^\dagger_{\mathbf{k}_2} a_{\mathbf{k}_2+\mathbf{k}} \end{aligned} \tag{2.5}$$

and

$$\begin{aligned}\hat{S}_{\mathbf{k}} &= N^{-1}\int d\mathbf{r}_1 d\mathbf{r}_2 d\mathbf{k}_1 d\mathbf{k}_2 d\mathbf{k}_3 d\mathbf{k}_4 e^{-i((\mathbf{k}_1+\mathbf{k}-\mathbf{k}_2)\mathbf{r}_1+(\mathbf{k}_3-\mathbf{k}_4-\mathbf{k})\mathbf{r}_2)} a^\dagger_{\mathbf{k}_1} a_{\mathbf{k}_2} a^\dagger_{\mathbf{k}_3} a_{\mathbf{k}_4} \\ &= N^{-1}\int d\mathbf{k}_1 d\mathbf{k}_4 a^\dagger_{\mathbf{k}_1} a_{\mathbf{k}_1+\mathbf{k}} a^\dagger_{\mathbf{k}_4+\mathbf{k}} a_{\mathbf{k}_4}\end{aligned} \tag{2.6}$$

If the condensate is uniform and excitation population is small compared to the condensate, we can apply Bogoliubov approximation $a_0 = \sqrt{N}$, obtaining for $\mathbf{k} \neq 0$

$$\hat{A}_{\mathbf{k}} = \sqrt{N}(a_{\mathbf{k}} + a^\dagger_{-\mathbf{k}}) \tag{2.7}$$

and

$$\hat{S}_{\mathbf{k}} = (a_{\mathbf{k}} + a^\dagger_{-\mathbf{k}})(a_{-\mathbf{k}} + a^\dagger_{\mathbf{k}}). \tag{2.8}$$

Therefore, the structure factor measures the quadrature of the bosonic modes $\pm\mathbf{k}$. Usually our systems have reflection symmetry, which means that the modes $\pm\mathbf{k}$ have the same states. Note that here we treat single shot as one measurement of the observables, and the expectation value of the observables is the ensemble average over experiment repetitions.

In practice, the observed atomic density is distorted by our finite imaging resolution, captured by the modulation transfer function (MTF) [10]. The modulation transfer function can be calibrated from the density fluctuations of a thermal gas. However, the MTF calibrated from low density thermal gas gives me a structure factor much smaller than 1 for a uniform high density BEC with low chemical potential, where the structure factor is predicted to be 1. Therefore, in practice I use the structure factor measured in the BEC as calibration, see Fig. 2.3. The experimentally measured structure factor is smoothed using the MATLAB `denoiseimage`, and used as the baseline. Measured structure factor of excited condensates are divided by this baseline to calibrate out the distortion.

The advantage of using `denoiseimage`, which is based on neural networks, instead of more traditional methods such as kernel smoothing, is that it removes the noise without

visibly introducing bias. Typical smoothing methods such as a low-pass filter also reduces the magnitude of peak features. Apparently this problem does not occur with `denoiseimage`, as can be seen in Fig. 2.3.

To give direct evidence that the measured atomic density saturates at high OD, we perform a trap expansion test. We first load the atoms into a smaller box trap, then expand the box trap. Supposedly we can never gain particle number during this process. However, we measure a higher particle number in the larger trap, where the OD is smaller. This proves that the atomic density is underestimated at high OD. See Fig. 2.4.

As first realized in [11], measuring the structure factor in a BEC can provide evidence of entanglement of phonon modes. In our system with low chemical potential, high energy phonon modes are equivalent to atomic modes. Therefore, we can employ similar techniques to prove entanglement of counter-propagating jets from Bose fireworks. Furthermore, since we can engineer higher order collisions of the jets [12; 13] in our system, we can potentially create multi-mode entanglement in the jets, which can also be detected through quadrature measurements such as the structure factor [14]. For this purpose, careful understanding and characterization of the MTF as well as any imaging distortions is required.

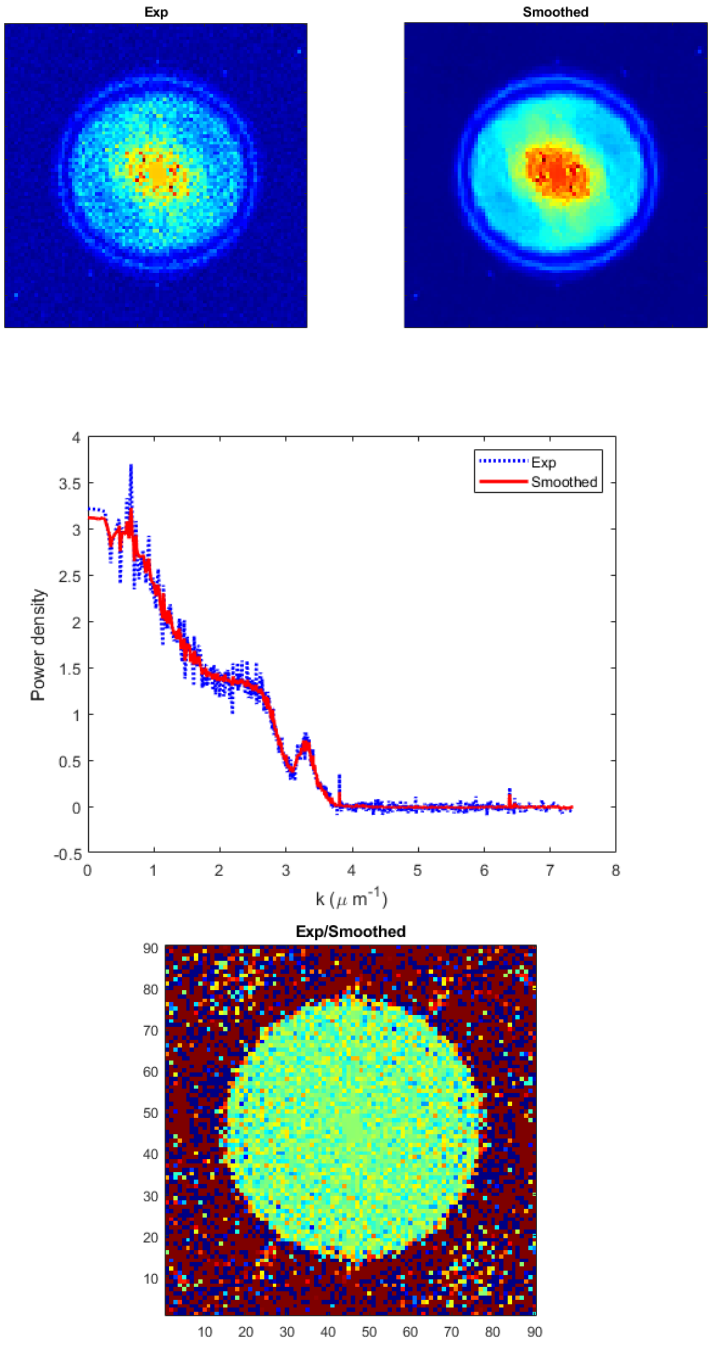

Figure 2.3: **Calibrating MTF using experimentally measured structure factor in a BEC.** Top: experimentally measured structure factor in a uniform BEC with low chemical potential, raw and after smoothing. The horizontal axes are momentum space coordinates. The two plots have different colorbar scales. Middle: a line cut showing low bias caused by smoothing. Bottom: the rescaled raw structure factor, which is noisy around 1, showing low bias of the calibration.

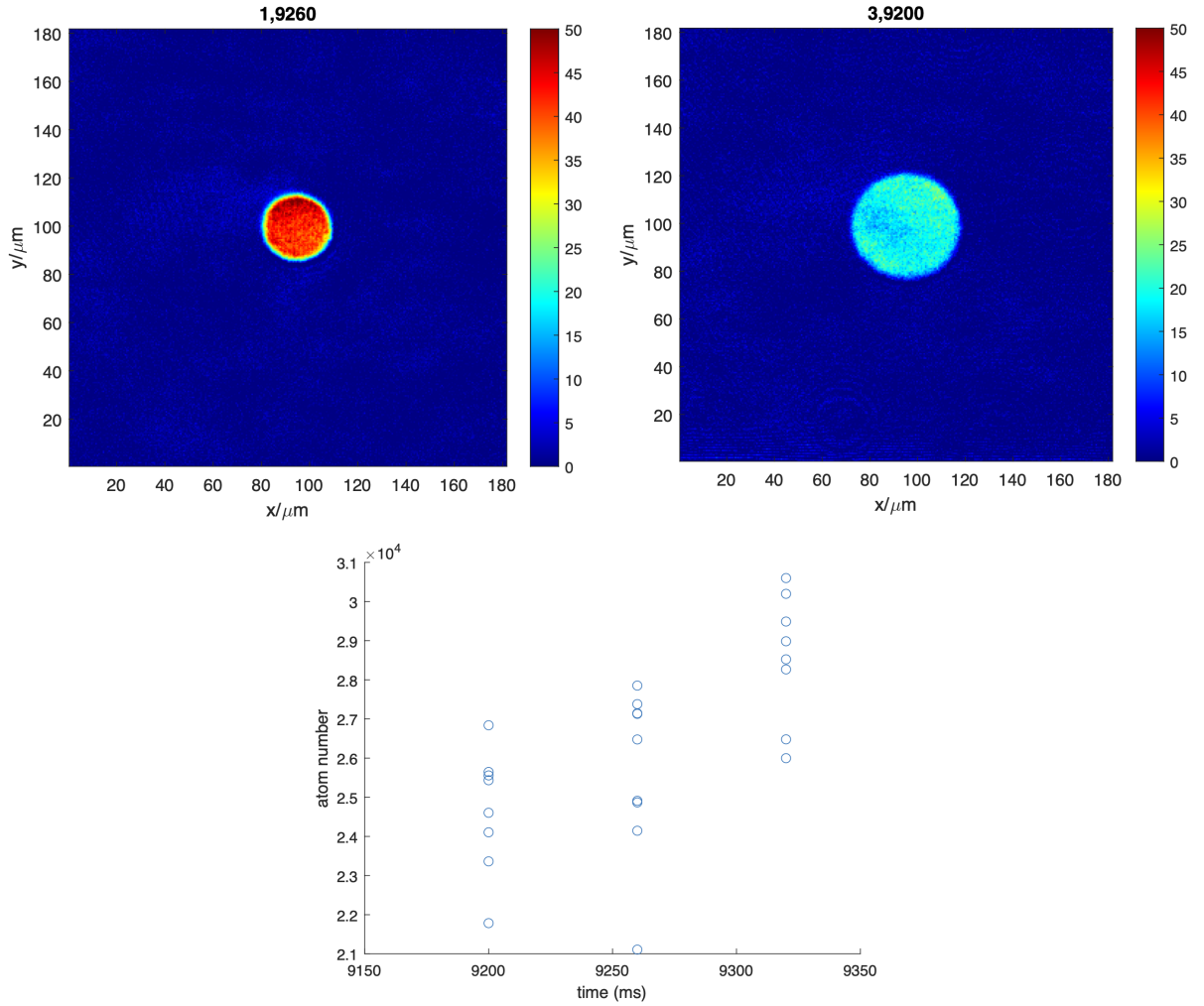

Figure 2.4: **Trap expansion shows saturation of atomic density measurement.** Top: measured atomic density before and after trap expansion. Colorbar shows density in μm^{-1}. Bottom: scatter plot of total atom number during trap expansion, showing an increase in measured atom number.

CHAPTER 3

SHAKEN LATTICE AND BOSE FIREWORKS IN BOSE-EINSTEIN CONDENSATES

3.1 Floquet theory of shaken lattice

Shaken optical lattice has become a powerful tool for engineering novel quantum systems, from artificial gauge fields to topological bands [15]. This technique plays an important role in this thesis. I will give an introduction to the theoretical and numerical treatment, which enables us to engineer desirable properties of atomic dispersion.

3.1.1 Single particle in optical lattice

Floquet systems are typically treated on the single particle level. We start with a single particle trapped in a one-dimensional (1D) optical lattice, described by the Hamiltonian

$$H = \frac{p^2}{2m} + \frac{U}{2}\cos(k_0 x + \phi), \tag{3.1}$$

where p is the momentum operator, m is the atomic mass, U is the lattice depth, k_0 is the lattice wavenumber and ϕ is the lattice phase.

In the context of Floquet engineering, the lattice depth U and phase ϕ may be time-dependent. The system is most easily solved in the momentum space basis $|k\rangle$. The transition elements of the Hamiltonian is

$$\langle k'|H|k\rangle = \frac{\hbar^2 k^2}{2m}\delta_{k,k'} + \frac{U}{4}(e^{i\phi}\delta_{k,k'+k_0} + e^{-i\phi}\delta_{k,k'-k_0}). \tag{3.2}$$

It is clear that the Hamiltonian only couples states with momentum differing by integer multiples of k_0. Therefore, the system factorizes into decoupled subsystems labeled by k modulo k_0, which we call the *quasimomentum*. For each quasimomentum k, the subsystem

Hamiltonian is a matrix of the form

$$H_k = \begin{pmatrix} \ddots & & & & \\ & \frac{\hbar^2(k+k_0)^2}{2m} & \frac{U}{4}e^{-i\phi} & & \\ & \frac{U}{4}e^{i\phi} & \frac{\hbar^2 k^2}{2m} & \frac{U}{4}e^{-i\phi} & \\ & & \frac{U}{4}e^{i\phi} & \frac{\hbar^2(k-k_0)^2}{2m} & \\ & & & & \ddots \end{pmatrix}. \tag{3.3}$$

The system is solved by finding the eigenvectors and eigenvalues,

$$H_k|n,k\rangle = \epsilon_{n,k}|n,k\rangle \tag{3.4}$$

The dispersion of the n-th band is given by $\epsilon_{n,k}$. The components of $|n,k\rangle$ give the Fourier components of the Bloch states. The Wannier function of each band can be obtained as well.

3.1.2 High-frequency expansion

In this section I briefly outline a general method for treating Floquet systems, the *high-frequency expansion* [16]. Consider a time-periodic Hamiltonian,

$$H(t+T) = H(t). \tag{3.5}$$

The periodicity implies a spectral decomposition,

$$H(t) = \sum_m H_m e^{im\omega t}, \tag{3.6}$$

where H_m are time-independent, and $\omega = 2\pi/T$. The Hermitianity implies $H_m = H_{-m}^\dagger$.

The evolution of the system is governed by the unitary

$$U(t_1, t_2) = e^{-i\int_{t_1}^{t_2} H(t')dt'}. \tag{3.7}$$

Since the Hamiltonian is periodic, we have $U(T, 2T) = U(0, T)$. Therefore we have the decomposition

$$U(0, nT + t) = \tilde{U}(0, t)U_T^n, \tag{3.8}$$

where $U_T = e^{-i\int_0^T H(t')dt'}$ is the stroboscopic evolution, and $\tilde{U}(0, t) = e^{-i\int_0^t H(t')dt'}$ is the micromotion with $t < T$. The stroboscopic evolution and the micromotion together completely characterizes a Floquet system.

The stroboscopic evolution can be reformulated in terms of an *effective* Hamiltonian H_{eff}, often simply called the Floquet Hamiltonian,

$$U_T = e^{-iH_{\text{eff}}T}. \tag{3.9}$$

On timescales longer than T, the system behaves like a time-independent system governed by the Hamiltonian H_{eff}, apart from the micromotion.

The high-frequency expansion gives an expansion for the effective Hamiltonian H_{eff} in terms of the spectral components H_m, in orders of the inverse driving frequency $1/\omega$.

$$H_{\text{eff}} = H_0 + \sum_{m\neq 0} \frac{H_m H_{-m}}{m\hbar\omega} + \mathcal{O}(\frac{1}{\omega^2}) \tag{3.10}$$

The expansion works best when the driving frequency is higher than the energy scale of the static Hamiltonian. It doesn't work well for near resonant driving. However, it provides a theoretical way of understanding how the driving dresses the static system.

3.1.3 Numerical calculation of Floquet bands

In this thesis lattice shaking is used to engineer the atomic dispersion, and it is important to predict the Floquet bands resulting from each driving scheme. For this purpose, we combine the previous two chapters into a numerical method that first calculates the effective Hamiltonian H_{eff} directly from the time-dependent driving, then from which calculates the band structure.

Each quasimomentum is treated in terms of the subsystem Hamiltonian H_k Eq. (3.3), with the time-dependent driving encoded into $U(t)$ and $\phi(t)$. Since the Hamiltonian matrix is infinite-dimensional, the Hilbert space is truncated to include only a finite number of momentum states, typically between $\pm 7k_0$. The truncation is chosen such that including even more states does not significantly alter the result. The stroboscopic evolution operator $U_T(k)$ Eq. (3.9) is numerically integrated from the time-dependent Hamiltonian.

The Floquet Hamiltonian $H_{\text{eff}}(k)$ is the logarithm of the stroboscopic evolution operator $U_T(k)$. As a result, diagonalizing the Hamiltonian $H_{\text{eff}}(k)$ can be achieved by diagonalizing $U_T(k)$. Given

$$U_T(k) = \sum_j e^{-i\epsilon_j(k)T/\hbar} |\psi_j(k)\rangle\langle\psi_j(k)|, \tag{3.11}$$

we have

$$H_{\text{eff}}(k) = \sum_j \epsilon_j(k) |\psi_j(k)\rangle\langle\psi_j(k)|. \tag{3.12}$$

A caveat here is that we need to carefully choose the branch cut for the logarithm, since the quasienergy $\epsilon_j(k)$ is only defined modulo $\hbar\omega$. One approach is to manually place the cut in a Floquet band gap, which can only be done with trial and error as the gap's location is not known *a priori*. Alternatively, one can modify the energy continuity condition for the definition of bands to use the periodic distance for measure of closeness, to allow for bands

to 'wrap around the torus'. Another issue is the numbering of bands, since the ordering based on energy into the ground, first excited, etc. bands is no longer applicable. One heuristic approach is to count the number of nodes (zeros) in the real-space wavefunction of the eigenstates. Alternatively one can order based on overlap with the eigenstates of the static band in the absence of driving. In any case, one needs to manually inspect the band labeling, to ensure that avoided crossings are treated properly. Some avoided crossings are essential to the qualitative features of the engineered dispersion, whereas others are due to weak coupling to very high lying bands, which should be ignored. Properly distinguishing the two is the root of the difficulty here.

So far the discussion is restricted to a simple sinusoidal lattice in 1D, as it is sufficient for the work in this thesis. Extensions to higher dimensions and more complicated lattice structures is straightforward.

3.2 Bose fireworks and the SU(1,1) representation

When a uniform disk shaped BEC is subject to oscillating interaction strength, jets of atoms emit in all directions in the plane. This phenomenon is called Bose fireworks [17]. Since its discovery in 2017, numerous followup experiments have been done [13; 18; 12]. Meanwhile, the theoretical aspect of this phenomenon has also attracted much attention [19; 20], and one result is a description in terms of the SU(1,1) algebra [21]. This description has greatly simplified our theoretical and numerical understanding of our experiments based on Bose fireworks, and inspired us to find a few-dimensional matrix representation of the physical states in infinite-dimensional Hilbert spaces. In this section, I will describe the theoretical framework for Bose fireworks, the description in terms of SU(1,1), and a resulting simple numerical method for simulating the system, which allows for application of pulse engineering techniques.

3.2.1 Bogoliubov approximation and two-mode squeezing

The physical system is a BEC subject to oscillating interaction strength, which is fundamentally described by the Hamiltonian

$$\mathcal{H} = \int dx \left(\Psi(x)^\dagger \frac{\hat{p}^2}{2m} \Psi(x) + \frac{g(t)}{2} \Psi(x)^\dagger \Psi(x)^\dagger \Psi(x) \Psi(x) \right), \tag{3.13}$$

where $\Psi(x)$ is the creation operator of a boson at position x (in any dimension), $\hat{p}$ is the momentum operator, m is atomic mass and $g(t)$ is the interaction strength. The system forms a BEC with condensate wavefunction $\psi_0(x)$. After Bogoliubov approximation [5] and going to momentum space, the Hamiltonian becomes

$$H = \sum_k \left(\epsilon_k a_k^\dagger a_k + \frac{g(t)}{2} (a_k^\dagger a_{-k}^\dagger + a_k a_{-k} + 2 a_k^\dagger a_k) \right), \tag{3.14}$$

where $g(t)$ is redefined to absorb the condensate density, $\epsilon_k = \frac{\hbar^2 k^2}{2m}$ is the kinetic energy and $a_k = \int e^{-ikx} \Psi(x)$ is the creation operator of a boson with momentum k. Rearranging the terms, we have

$$H = \frac{1}{2} \sum_k \left((\epsilon_k + g(t))(a_k^\dagger a_k + a_{-k}^\dagger a_{-k}) + g(t)(a_k^\dagger a_{-k}^\dagger + a_k a_{-k}) \right). \tag{3.15}$$

Under single frequency drive $g(t) = 2(g e^{i\omega t} + g^* e^{-i\omega t})$, one can perform rotating wave approximation (RWA), arriving at

$$H = \frac{1}{2} \sum_k \left((\epsilon_k - \hbar\omega/2)(a_k^\dagger a_k + a_{-k}^\dagger a_{-k}) + (g^* a_k^\dagger a_{-k}^\dagger + g a_k a_{-k}) \right) \tag{3.16}$$

Considering only one pair of resonant modes with $\epsilon_k = \hbar\omega/2$, we have

$$H = g^* a_k^\dagger a_{-k}^\dagger + g a_k a_{-k}. \tag{3.17}$$

This Hamiltonian describes two-mode squeezing. Starting from vacuum (no excitations), the system evolves into a two-mode squeezed state

$$|f\rangle = e^{-iHt}|0\rangle = \frac{1}{\sqrt{1-z^2}} \sum_n z^n |n,n\rangle, \tag{3.18}$$

where $z = \frac{g}{|g|} \tanh |g|t$ is the squeezing parameter and $|n,n\rangle$ denotes the state with n particles each in k and $-k$ mode.

The two-mode squeezed state is of wide interest and applications. It is a thermofield double state of two harmonic oscillators [22], which becomes a mixed state with Boltzman distribution when one subsystem is traced out. Thermofield double states are of central interest in quantum information theory, connecting to black holes and quantum chaos [23]. It also carries EPR entanglement, and experimental verification of the entanglement remains an important experimental goal in our lab.

3.2.2 Finite chemical potential and phonon fireworks

The above treatment assumes zero mean (DC) chemical potential. It turns out that the situation remains largely the same when the mean chemical potential is nonzero. Taking one pair of modes, we now have the Hamiltonian

$$H = (\epsilon_k + g(t))(a_k^\dagger a_k + a_{-k}^\dagger a_{-k}) + g(t)(a_k^\dagger a_{-k}^\dagger + a_k a_{-k}) \tag{3.19}$$

with $g(t) = g_0 + 2(ge^{i\omega t} + g^* e^{-i\omega t})$. We can no longer directly apply RWA, as the DC chemical potential would be a problem. However, we can first apply a Bogoliubov transformation to the phonon basis,

$$\alpha_k = \sqrt{\frac{\epsilon_k + g_0 + \tilde{\epsilon}_k}{2\tilde{\epsilon}_k}} a_k + \sqrt{\frac{\epsilon_k + g_0 - \tilde{\epsilon}_k}{2\tilde{\epsilon}_k}} a_{-k}^\dagger, \tag{3.20}$$

where $\tilde{\epsilon}_k = \sqrt{\epsilon_k^2 + 2\epsilon_k g_0}$ is the phonon energy.

The Hamiltonian is rewritten as

$$H = (\tilde{\epsilon}_k + \tilde{g}(t)\frac{\epsilon_k}{\tilde{\epsilon}_k})(\alpha_k^\dagger \alpha_k + \alpha_{-k}^\dagger \alpha_{-k}) + \tilde{g}(t)\frac{\epsilon_k}{\tilde{\epsilon}_k}(\alpha_k^\dagger \alpha_{-k}^\dagger + \alpha_k \alpha_{-k}), \tag{3.21}$$

where $\tilde{g}(t) = g(t) - g_0$. Comparing with Eq. (3.15), we can see that the effect of finite DC chemical potential is simply a change to the phonon basis and a scaling factor $\epsilon_k/\tilde{\epsilon}_k$ on the interaction driving amplitude. Therefore, in this case we would have Bose fireworks of phonons.

A caveat is that this derivation assumes a uniform BEC with infinite size. In reality for BECs with boundaries, the phonons would be reflected by the boundary which introduces complicated coupling between all momentum modes. The free bosons, on the otherhand, would not be reflected by the BEC boundary.

3.2.3 SU(1,1) representation and the Poincare disk

In this section we describe the SU(1,1) representation of the Bose fireworks, as detailed in [21].

Consider the RWA Hamiltonian Eq. (3.16). Since different pairs of momentum modes are decoupled, consider one pair k and $-k$.

$$H = (\epsilon_k - \hbar\omega/2)(a_k^\dagger a_k + a_{-k}^\dagger a_{-k}) + g^* a_k^\dagger a_{-k}^\dagger + g a_k a_{-k} \tag{3.22}$$

Define $K_0 = (a_k^\dagger a_k + a_{-k} a_{-k}^\dagger)/2$, $K_1 = (a_k^\dagger a_{-k}^\dagger + a_k a_{-k})/2$, $K_2 = (a_k^\dagger a_{-k}^\dagger - a_k a_{-k})/(2i)$, $K_+ = K_1 + iK_2$ and $K_- = K_1 - iK_2$. The Hamiltonian is rewritten as

$$H = 2\Delta K_0 + g^* K_+ + g K_-, \tag{3.23}$$

where $\Delta = (\epsilon_k - \hbar\omega/2)$ is the detuning. The operators $K_{0,1,2}$ form the $\mathfrak{su}(1,1)$ algebra, defined by the commutation relations

$$\begin{aligned} [K_0, K_1] &= iK_2 \\ [K_2, K_0] &= iK_1 \\ [K_1, K_2] &= -iK_0 \end{aligned} \tag{3.24}$$

Therefore the Hamiltonian H is an element of the $\mathfrak{su}(1,1)$ algebra, the time evolution operator $U = e^{-iHt}$ is an element of the SU(1,1) group, and the dynamics it generates is a representation of the SU(1,1) group.

It is known that one representation of the SU(1,1) group is the Poincare disk, which is a 2D unit disk equipped with a hyperbolic metric. On the Poincare disk, geodesics are circular arcs that perpendicularly intersect with the boundary circle. The distance of a point to the origin goes to infinity as it approaches the boundary. In fact, there is a simple correspondence between the dynamically accessible states and the Poincare disk. Starting from the vacuum, the Hamiltonian Eq. (3.23) generates two-mode squeezed states Eq. (3.18). The squeezing parameter z, which is a complex number with $||z|| < 1$, gives the coordinate on the Poincare disk as its real and imaginary parts. The vacuum is at the origin of the Poincare disk. The polar angle of z gives the phase of the two-mode squeezed state. Operator K_0 generates rotation around the origin, which corresponds to phase winding. Operator $K_{1,2}$ generates boost along two different directions. The population is $n = \langle a_k^\dagger a_k \rangle = \frac{||z||^2}{1-||z||^2}$. The structure factor is $S = \langle (a_k + a_{-k}^\dagger)(a_{-k} + a_k^\dagger) \rangle = \ 1 + 2n \left(1 + \mathrm{Re}\frac{1}{z}\right)$.

In the Poincare disk representation of SU(1,1), elements of SU(1,1) acts on the Poincare disk as Mobius transformations written as 2×2 complex matrices,

$$\begin{bmatrix} a & b \\ c & d \end{bmatrix} : z \to \frac{az + b}{cz + d}. \tag{3.25}$$

Writing the generators $K_{0,1,2}$ in terms of 2×2 matrices, we have

$$K_0 = \frac{1}{2}\begin{bmatrix} 1 & 0 \\ 0 & -1 \end{bmatrix} = \frac{1}{2}\sigma_z, \tag{3.26}$$

$$K_1 = \frac{1}{2}\begin{bmatrix} 0 & 1 \\ -1 & 0 \end{bmatrix} = \frac{i}{2}\sigma_y, \tag{3.27}$$

$$K_2 = \frac{1}{2}\begin{bmatrix} 0 & -i \\ -i & 0 \end{bmatrix} = -\frac{i}{2}\sigma_x, \tag{3.28}$$

where σ denotes Pauli matrices. The time evolution operator $U = e^{-iHt}$ is then written as

$$U = \begin{bmatrix} \cosh\kappa t - \frac{i\Delta}{\kappa}\sinh\kappa t & -\frac{ig^*}{\kappa}\sinh\kappa t \\ \frac{ig}{\kappa}\sinh\kappa t & \cosh\kappa t + \frac{i\Delta}{\kappa}\sinh\kappa t \end{bmatrix}, \tag{3.29}$$

where $\kappa = \sqrt{|g|^2 - \Delta^2}$.

This means that the dynamics of the system can be represented by two-dimensional matrices instead of a infinite-dimensional Hilbert space, although the 2D matrices are no longer Hermitian or unitary. As we will see in the section below, there is actually a much simpler way to represent the system by few-dimensional matrices, which proves very convenient for numerical simulations.

Since the mean population of a two-mode squeezed state $|z\rangle$ is $||z||^2/(1-||z||^2)$, states with significant excitation population are very close to the boundary, making the Poincare disk a poor visualization. Alternatively, one can parameterize the state $|z\rangle$ with the expectation values of $K_{1,2}$, similar to how spin-1/2 states are parameterized by expectation values of Pauli matrices, forming the Bloch sphere.

3.2.4 Numerical simulation of the Heisenberg equation

Consider a quadratic Hamiltonian of two bosonic modes a_k and a_{-k},

$$H = A^{\dagger T} F A + \frac{1}{2} A^{\dagger T} G A^{\dagger} + \frac{1}{2} A^T G^* A, \tag{3.30}$$

where $A = \begin{bmatrix} a_k \\ a_{-k} \end{bmatrix}$ is a vector of the bosonic annihilation operators and F, G are coefficient matrices. In the case of Hamiltonian Eq. (3.22), we would have

$$F = \begin{bmatrix} \epsilon_k - \hbar\omega/2 & 0 \\ 0 & \epsilon_k - \hbar\omega/2 \end{bmatrix}$$

$$G = \begin{bmatrix} 0 & g \\ g & 0 \end{bmatrix}.$$

The Heisenberg equations are

$$\begin{aligned} \dot{A} &= -iFA - iGA^{\dagger} \\ \dot{A}^{\dagger} &= iF^* A^{\dagger} + iG^* A \end{aligned} \tag{3.31}$$

Constructing vector $V = \begin{bmatrix} A \\ A^{\dagger} \end{bmatrix}$ and matrix $M = \begin{bmatrix} F & G \\ -F^* & G^* \end{bmatrix}$, the equations are rewritten as

$$\dot{V} = -iMV, \tag{3.32}$$

which is solved as

$$V(t) = e^{-iMt} V(0). \tag{3.33}$$

This solution expresses the operators $a_{\pm k}(t)$ as a function of the initial operators $a_{\pm k}(0)$. From here the correlation functions as a function of time can be readily computed, as the expectation values of the initial operators are evaluated in the vacuum.

In particular, expressing the solution as $a(t) = u(t)A(0) + v(t)A^\dagger(0)$, where $a(t)$ is the annihilation operator of a particular mode, and $u(t), v(t)$ are coefficient vectors, we have

$$\langle a^\dagger(t)a(t)\rangle = ||v(t)||^2. \tag{3.34}$$

The coefficient vectors $u(t), v(t)$ are slices of the matrix $U = e^{-iMt}$. It is straightforward to obtain all correlators from the matrix U. Therefore, numerically the system can be solved through a matrix exponentiation. Time dependent Hamiltonian can be solved through Trotterization.

This method can be applied to solve any quadratic Hamiltonian, not only ones in SU(1,1). For example, it can deal with terms like $a_k^\dagger a_{-k}$, generated by for example Bragg diffraction with an optical lattice of wavevector $2k$. In addition, the system can involve more than two modes. Solving m modes coupled together by a quadratic Hamiltonian becomes $2m \times 2m$ matrix algebra.

3.2.5 Pulse engineering with JAX

During the many-body echo project, one research objective was to reverse the excitation as much as possible by changing the reversal driving pulse. This can be formulated as a *pulse engineering* problem. A pulse engineering problem is generally formulated as the following. Given an initial state $|i\rangle$, a tunable Hamiltonian $H(\lambda)$ and a target state $|t\rangle$, find an optimal time series of $\lambda(t)$ (a *pulse*), such that the final state $|f\rangle = e^{-i\int Hdt}|i\rangle$ is as close to the target $|t\rangle$ as possible. In our case, the target state is the vacuum $|0\rangle$, the Hamiltonian is Eq. (3.15), and the pulse is $g(t)$. The initial state is obtained by driving the system with a sinusoidal pulse. A more convenient formulation is to have both the initial state and the

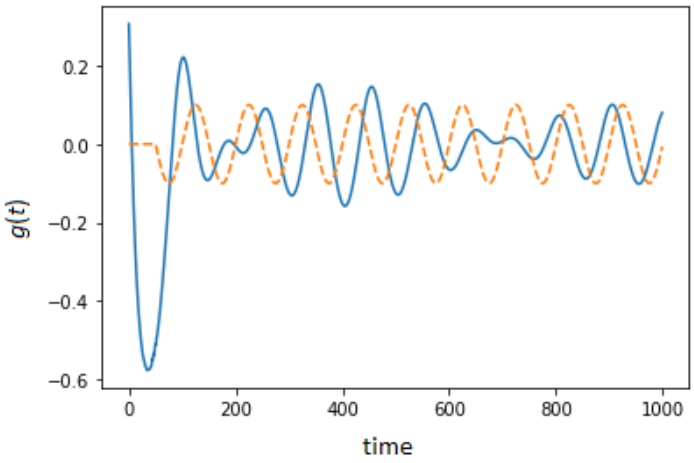

Figure 3.1: **Optimal reversal pulse found by pulse engineering.** Blue curve is the optimized pulse $g(t)$. Yellow dotted curve is the heuristic initial guess, which is shifting the fixed sinusoidal excitation pulse by half a period.

target state be the vacuum, and have the first part of the pulse be fixed as sinusoidal.

Pulse engineering see wide applications in quantum optimal control, for optimizing gate pulses for qubit operations in the quantum information processing context [24]. Many techniques have been introduced for efficient optimization of a continuous time series [25]. With recent advances in the machine learning community, particularly in the area of automatic differentiation [26], gradient optimization in high dimensional parameter spaces has become easier than ever. One toolbox for easy implementation of automatic differentiation is JAX, developed by Google [27]. It also has the added benefit of enabling parallel computation with both CPUs and GPUs.

Computationally carrying out the pulse engineering optimization with JAX requires several modules. First, a module needs to carry out the numerical simulation of the system dynamics, given a specific pulse. This is achieved by the matrix algebra described in the previous section. Since the total system contains many independent pairs of momentum modes, each pair is computed separately, where parallelization can significantly improve efficiency. Second, another module needs to evaluate the objective function given the final state

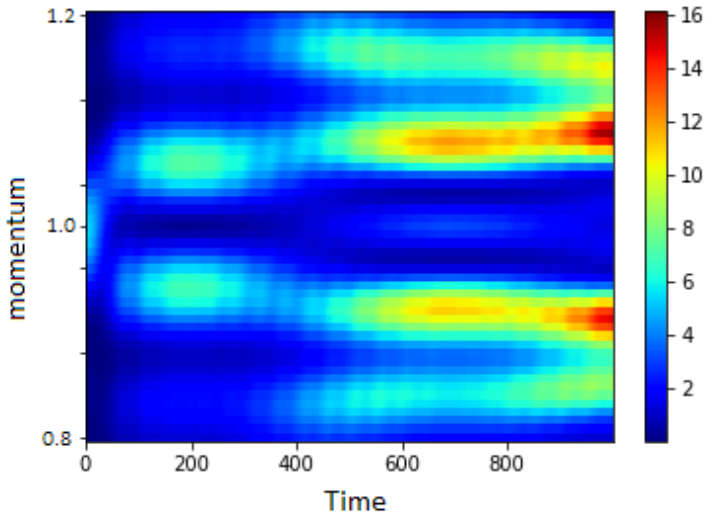

Figure 3.2: Evolution of excitation population for each momentum as a function of time.

produced by the previous module. The objective function can be the overlap with the target state, or more heuristic like the total excitation population of the final state, along with regularization constraints such as strength and smoothness of the pulse. The two modules need to be wrapped together to evaluate the objective function for each trial pulse. For gradient based optimizers, normally gradients of the objective function also need to be computed. With auto-differentiation with JAX, the gradient can be computed automatically using the chain rule on each elementary operation carried out by the function, such as addition and multiplication. This can be achieved by building the function using only JAX-compatible operations. The objective function and gradient evaluations can then be fed into a gradient based optimizer which is prevalent in machine learning, which produces an optimal pulse.

In my attempt, the final total population over a range of momentum modes is minimized. The optimal pulse is shown in Fig. 3.1, along with the heuristic initial guess. The evolution of excitation population for each momentum as a function of time is shown in Fig. 3.2. The final population as a function of momentum is plotted against the initial population (after the fixed sinusoidal pulse) in Fig. 3.3. The objective function is the sum of population between momentum 0.95 and 1.05, and we can see that the optimal pulse pushes the excitation

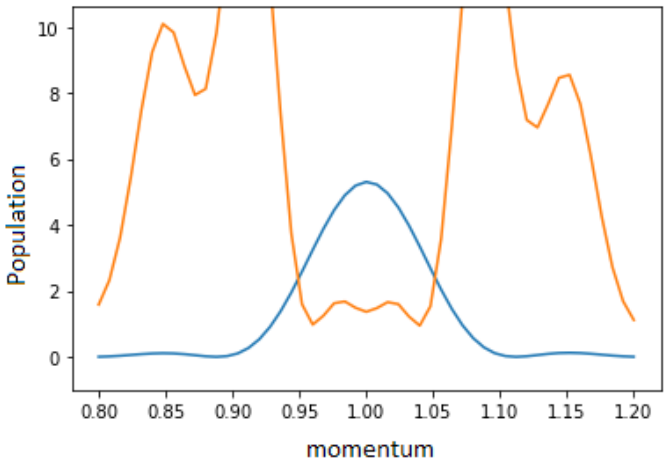

Figure 3.3: **Initial and final population as a function of momentum.** The blue curve shows the initial population as a function of momentum, after the fixed sinusoidal driving. Yellow curve shows the final population. Excitation within the optimization window of momentum, 0.95 to 1.05, is reversed, whereas outside the window the excitation grows.

outside of the target momentum window. This result, on one hand, shows the ability of the optimizer to produce effective and nontrivial pulse shapes. On the other hand, it also suggests that by controlling the interaction strength $g(t)$ alone, it is impossible to reverse the excitation for all momentum modes. Indeed, in the many-body echo project described in section 5, we can achieve the reversal of all momentum modes only by additional means of controlling the system.

3.3 Reconstruction of condensate wavefunction from Bose fireworks

In the experiment, we typically observe Bose fireworks emitted from a uniform ground state condensate. Theoretically we often consider the condensate as occupying the $k = 0$ state. However, in some experiments we observe Bose fireworks emitted from excited condensates, for example ones hosting solitons or vortices. The pattern in the jets differ significantly from that emitted by a ground state condensate. In the study of the patterns of emitted

jets from various excited condensates [28], I derived a theoretical correspondence between the condensate wavefunction and correlations in jets. This section presents the derivation in further detail.

3.3.1 Introduction

To first order in Bogoliubov approximation, a condensate with wavefunction Ψ with modulated interaction undergoes firework described by Hamiltonian

$$H = \frac{1}{2}\sum_{jl} F_{jl} a_j a_l + h.c. \tag{3.35}$$

Here a_j annihilates a particle in the plane wave state $\psi_j = e^{ik_j r}$, and $F_{jl} = \int dr \psi_j \psi_l \Psi^{*2}(r) = \int dr e^{i(k_j+k_l)r} \Psi^{*2}(r)$ is the overlap function. By measuring the distribution of particle number in the momentum space n_j, we hope to gain information of $\Psi(r)$.

Below, we will prove that if we knew, instead of the particle number n_j, correlations such as $\langle a_j a_k \rangle$ and $\langle a_j^\dagger a_k \rangle$, we would be able to fully reconstruct $\Psi(r)$. But more importantly, even only knowing n_j, we will show that we still can reconstruct $|F_{jl}|$, which is the fourier space power spectrum of Ψ^2. The phases of F_{jl}, however, will be shown to be impossible to recover from n_j only.

3.3.2 Reconstructing squeezing Hamiltonian from final state correlations

Result

Consider a system of N bosonic modes $a_j, j = 1, 2, 3, ..., N$. Consider the squeezing Hamiltonian

$$H = \frac{1}{2}\sum_{jk} F_{jk} a_j a_k + h.c. \tag{3.36}$$

Choose F_{jk} be symmetric. Let $A = (a_1, a_1^\dagger, ..., a_N, a_N^\dagger)^T$.

As the vector space for A is $2N$ dimensional, where each mode has two degrees of freedom, there is a natural decomposition for any matrix K acting on A, into $K = \hat{K} \otimes \sigma$, where $\hat{K}$ is an $N \times N$ matrix describing the mixing of different modes and σ is a 2×2 matrix describing mixing of a and $a^\dagger$ within each mode.

Define $G = -(\mathrm{Re}F) \otimes \sigma_x - (\mathrm{Im}F) \otimes \sigma_y$, where σ_i are the Pauli matrices. Then the Hamiltonian can be written as

$$H = -\frac{1}{2} A^\dagger G A^T \tag{3.37}$$

Define matrix S.

$$S = I_N \otimes \frac{1}{\sqrt{2}} \begin{pmatrix} 1 & 1 \\ -i & i \end{pmatrix} \tag{3.38}$$

Let $g_{jk} = \langle A_j A_k + A_k A_j \rangle$, which are correlations like $\langle a_j a_k \rangle$ and $\langle a_j^\dagger a_k \rangle$. Define K,

$$K = \frac{1}{2} \ln S g S^T \tag{3.39}$$

From experimental measurements of correlations g (assuming this is possible for the moment), the coefficients F can be obtained through

$$\mathrm{Re}F = -\frac{1}{2} \mathrm{Tr}_\sigma K (I \otimes \sigma_x) \tag{3.40}$$

$$\mathrm{Im}F = -\frac{1}{2} \mathrm{Tr}_\sigma K (I \otimes \sigma_z) \tag{3.41}$$

where Tr_σ means trace over the Pauli matrices (tracing over each 2-by-2 block).

Previously we have been able to predict correlations given the form of F, but not the other

way around. Here is the solution to the inverse problem, solving for F given correlations g.

Example

As a simple example, let $N = 2$, and

$$F = \begin{pmatrix} 0 & f \\ f & 0 \end{pmatrix} \tag{3.42}$$

$$H = f^* a_1^\dagger a_2^\dagger + h.c. \tag{3.43}$$

Heisenberg equations of motion:

$$\dot{a}_1 = i[H, a_1] = -if^* a_2^\dagger \tag{3.44}$$

$$\dot{a}_2 = i[H, a_2] = -if^* a_1^\dagger \tag{3.45}$$

Solution:

$$a_1(t) = \cosh|f|t \; a_1(0) - i\sqrt{\frac{f^*}{f}} \sinh|f|t \; a_2^\dagger(0) \tag{3.46}$$

$$a_2(t) = \cosh|f|t \; a_2(0) - i\sqrt{\frac{f^*}{f}} \sinh|f|t \; a_1^\dagger(0) \tag{3.47}$$

Let $t = 1$. Correlation matrix

$$g = \begin{pmatrix} 0 & \cosh 2|f| & -i\sqrt{\frac{f^*}{f}}\sinh 2|f| & 0 \\ \cosh 2|f| & 0 & 0 & i\sqrt{\frac{f}{f^*}}\sinh 2|f| \\ -i\sqrt{\frac{f^*}{f}}\sinh 2|f| & 0 & 0 & \cosh 2|f| \\ 0 & i\sqrt{\frac{f}{f^*}}\sinh 2|f| & \cosh 2|f| & 0 \end{pmatrix} \tag{3.48}$$

Mathematica tells me

$$K = \frac{1}{2}\ln SgS^T = \begin{pmatrix} 0 & 0 & -\mathrm{Im}f & -\mathrm{Re}f \\ 0 & 0 & -\mathrm{Re}f & \mathrm{Im}f \\ -\mathrm{Im}f & -\mathrm{Re}f & 0 & 0 \\ -\mathrm{Re}f & \mathrm{Im}f & 0 & 0 \end{pmatrix} \tag{3.49}$$

$$= -\mathrm{Im}F \otimes \sigma_z - \mathrm{Re}F \otimes \sigma_x$$

$$K(I \otimes \sigma_x) = \begin{pmatrix} 0 & 0 & -\mathrm{Re}f & -\mathrm{Im}f \\ 0 & 0 & \mathrm{Im}f & -\mathrm{Re}f \\ -\mathrm{Re}f & -\mathrm{Im}f & 0 & 0 \\ \mathrm{Im}f & -\mathrm{Re}f & 0 & 0 \end{pmatrix} \tag{3.50}$$

$$K(I \otimes \sigma_z) = \begin{pmatrix} 0 & 0 & -\mathrm{Im}f & \mathrm{Re}f \\ 0 & 0 & -\mathrm{Re}f & -\mathrm{Im}f \\ -\mathrm{Im}f & \mathrm{Re}f & 0 & 0 \\ -\mathrm{Re}f & -\mathrm{Im}f & 0 & 0 \end{pmatrix} \tag{3.51}$$

Therefore

$$-\frac{1}{2}\mathrm{Tr}_\sigma K(I \otimes \sigma_x) = \begin{pmatrix} 0 & \mathrm{Re}f \\ \mathrm{Re}f & 0 \end{pmatrix} = \mathrm{Re}F \tag{3.52}$$

$$-\frac{1}{2}\mathrm{Tr}_\sigma K(I\otimes\sigma_z)=\begin{pmatrix}0 & \mathrm{Im}f\\ \mathrm{Im}f & 0\end{pmatrix}=\mathrm{Im}F \tag{3.53}$$

Derivations

With vacuum as the initial state, the system evolves to

$$\rho = U\rho_0 U^\dagger \tag{3.54}$$

, where $U = e^{-iHT}$. Rescale F_{jk} such that $T = 1$.

Since the Hamiltonian is quadratic and the initial state is the vacuum, it is convenient to use the formalism of Gaussian states. Here we follow the treatment described in [29]. In particular section 1.2 contains many important concepts.

Any Gaussian states can be fully described by a displacement d and a covariance matrix γ. It is straight forward to see that the displacement $d = 0$ for all states concerned here. According to Theorem 3, Eq (3.54) implies a relationship between the covariance matrices of the vacuum state and the final state,

$$\gamma = M\gamma_0 M^T \tag{3.55}$$

where M is given by

$$U^\dagger R U = MR \tag{3.56}$$

and $R = (x_1, p_1, ..., x_N, p_N)^T$, $x_j = (a_j + a_j^\dagger)/\sqrt{2}, p_j = (a_j - a_j^\dagger)/\sqrt{2}i$. Note that $R = SA$.

Our goal is to derive the coefficients F_{jk} from the correlation functions. The covariance matrix can be obtained from the correlation functions, which is related to the time evolution operator U by Eq (3.55) and Eq (3.56), which in turn gives F_{jk}.

Step 1: From M to F

We can solve Eq (3.56) with the BCH formula,

$$e^{iH}Re^{-iH} = R + [iH, R] + \frac{1}{2}[iH, [iH, R]] + ... \tag{3.57}$$

We need commutators $[H, R]$.

We have

$$[A, A] = I_N \otimes i\sigma_y \tag{3.58}$$

$$[A, A^\dagger] = I_N \otimes \sigma_z \tag{3.59}$$

Therefore we have

$$[H, A] = \frac{1}{2}\left((I \otimes \sigma_z)G + (I \otimes i\sigma_y)G^T(I \otimes \sigma_x)\right)A = -i(\mathrm{Re}F \otimes \sigma_y - \mathrm{Im}F \otimes \sigma_x))A \tag{3.60}$$

And

$$[H, R] = -i\hbar\dot{R} = -i\hbar S\dot{A} = S[H, A] \tag{3.61}$$

$$S[H, A] = -iS(\mathrm{Re}F \otimes \sigma_y - \mathrm{Im}F \otimes \sigma_x)S^{-1}R = i(\mathrm{Re}F \otimes \sigma_x + \mathrm{Im}F \otimes \sigma_z)R \tag{3.62}$$

Therefore, let $K = -\mathrm{Re}F \otimes \sigma_x - \mathrm{Im}F \otimes \sigma_z$,

$$[iH, R] = KR \tag{3.63}$$

Eq (3.57) becomes

$$R + KR + \frac{1}{2}KKR + ... = e^K R = MR \tag{3.64}$$

Therefore

$$M = e^K \tag{3.65}$$

Step 2: From γ to M

As K is obviously symmetric, we have

$$\gamma = e^K \gamma_0 e^K \tag{3.66}$$

The covariance matrix for vacuum is just the identity, $\gamma_0 = I$.

$$\gamma = e^{2K} \tag{3.67}$$

Therefore

$$K = \frac{1}{2} \ln \gamma \tag{3.68}$$

The covariance matrix is given by

$$\gamma_{jk} = \langle R_j R_k + R_k R_j \rangle \tag{3.69}$$

$$R = SA \tag{3.70}$$

where $A = (a_1, a_1^\dagger, ..., a_N, a_N^\dagger)^T$ and

$$S = I \otimes \frac{1}{\sqrt{2}} \begin{pmatrix} 1 & 1 \\ -i & i \end{pmatrix} \tag{3.71}$$

Therefore,

$$\gamma_{jk} = \sum_{pq} S_{jp} S_{kq} \langle A_p A_q + A_q A_p \rangle \tag{3.72}$$

Writing $g_{jk} = \langle A_j A_k + A_k A_j \rangle$, which are correlations like $\langle a_j a_k \rangle$ and $\langle a_j^\dagger a_k \rangle$,

$$\gamma = S g S^T \tag{3.73}$$

Finally,

$$K = \frac{1}{2} \ln S g S^T \tag{3.74}$$

From which we have

$$\mathrm{Re}F = -\frac{1}{2} \mathrm{Tr}_\sigma K (I \otimes \sigma_x) \tag{3.75}$$

$$\mathrm{Im}F = -\frac{1}{2} \mathrm{Tr}_\sigma K (I \otimes \sigma_z) \tag{3.76}$$

3.3.3 Two point correlator from population measurements

Suppose we have a Gaussian state, and measurements of n_j and its correlators. Can we figure out what g is? If not, what can we tell about F_{jl}?

Let me argue first that, unfortunately, we cannot fully reconstruct g. Consider basis transformation $a'_j = e^{i\theta_j} a_j$, where θ_j is different for different j. Under this transformation, obviously n_j is invariant. However, g is not. It's more obvious to see how F_{jl} transforms.

The basis transformation transforms the state $\psi'_j = e^{i\theta_j}\psi_j$, and thus the overlap function transforms as $F'_{jl} = e^{i(\theta_j+\theta_l)}F_{jl}$. Therefore the magnitude $|F_{jl}|$ is invariant under this transformation, but the phase is not.

This means that from observations of n_j, it's impossible to determine the phase of F. However, this also means that we can choose arbitrary θ_j when trying to obtain $|F|$ from n_j. Below I show how this is done.

For the rest of this section I will make a change of notation. Let $g_{jk} = \langle a_j^\dagger a_k \rangle$ be the normal correlator, and $h_{jk} = \langle a_j a_k \rangle$ be the anomolous correlator. Note that $g_{jk} = g_{kj}^*$ and $h_{jk} = h_{kj}$. Then we have

$$\langle n_j \rangle = g_{jj} = n_j \tag{3.77}$$

where I denote the expection value as n_j when it's not in an operator expression.

Let's do some Wick contraction:

$$\langle n_j n_k \rangle = n_j n_k + |g_{jk}|^2 + |h_{jk}|^2 \tag{3.78}$$

$$\langle n_j n_j \rangle = 2n_j^2 + |h_{jj}|^2 \tag{3.79}$$

Since we can make an arbitrary basis transformation of the form $a'_j = e^{i\theta_j}a_j$, we can choose θ_j such that all $h_{jj} \in \mathbb{R}$. Then we have

$$h_{jj} = \sqrt{\langle n_j n_j \rangle - 2n_j^2} \tag{3.80}$$

Define connected correlators

$$\langle n_j n_k \rangle_c = \langle n_j n_k \rangle - n_j n_k \tag{3.81}$$

$$\langle n_j^2 n_k\rangle_c = \langle n_j^2 n_k\rangle - 2n_j\langle n_j n_k\rangle_c - n_k\langle n_j^2\rangle_c - n_j^2 n_k \tag{3.82}$$

Then we have

$$\langle n_j^2 n_k\rangle_c = 2n_j\langle n_j n_k\rangle_c + 2h_{jj}\left(g_{jk}h_{jk}^* + c.c.\right) \tag{3.83}$$

$$\langle n_k^2 n_j\rangle_c = 2n_k\langle n_j n_k\rangle_c + 2h_{kk}\left(g_{jk}h_{jk} + c.c.\right) \tag{3.84}$$

$$\begin{aligned}\langle n_j^2 n_k^2\rangle &= 4n_j\langle n_j n_k^2\rangle_c + 4n_k\langle n_k n_j^2\rangle_c + 4\langle n_j n_k\rangle_c^2 \\ &+ \langle n_j^2\rangle_c\langle n_k^2\rangle_c + n_j^2\langle n_k^2\rangle_c + n_k^2\langle n_j^2\rangle_c + 5n_j^2 n_k^2 \\ &+ 8|g_{jk}|^2|h_{jk}|^2 + 2h_{jj}h_{kk}\left(g_{jk}^2 + h_{jk}^2 + c.c.\right)\end{aligned} \tag{3.85}$$

Therefore, for each pair of modes a_j, a_k, we have the following set of equations.

$$g_{jj} = \langle n_j\rangle = n_j \tag{3.86}$$

$$h_{jj} = \sqrt{\langle n_j n_j\rangle_c - n_j^2} \tag{3.87}$$

$$|g_{jk}|^2 + |h_{jk}|^2 = \langle n_j n_k\rangle_c = A \tag{3.88}$$

$$g_{jk}h_{jk}^* + c.c. = \frac{1}{2h_{jj}}\left(\langle n_j^2 n_k\rangle_c - 2n_j\langle n_j n_k\rangle_c\right) = B \tag{3.89}$$

$$g_{jk}h_{jk} + c.c. = \frac{1}{2h_{kk}}\left(\langle n_k^2 n_j\rangle_c - 2n_k\langle n_j n_k\rangle_c\right) = C \tag{3.90}$$

$$
\begin{aligned}
8|g_{jk}|^2|h_{jk}|^2 + 2h_{jj}h_{kk}\left(g_{jk}^2 + h_{jk}^2 + c.c.\right) =& \langle n_j^2 n_k^2\rangle - 4n_j\langle n_j n_k^2\rangle_c - 4n_k\langle n_k n_j^2\rangle_c \\
& - 4\langle n_j n_k\rangle_c^2 - \langle n_j^2\rangle_c\langle n_k^2\rangle_c \\
& - n_j^2\langle n_k^2\rangle_c - n_k^2\langle n_j^2\rangle_c - 5n_j^2 n_k^2 \\
=& D
\end{aligned}
\tag{3.91}
$$

Eq (3.86) gives g_{jj} and g_{kk}. Eq (3.87) gives h_{jj} and h_{kk}. Eq (3.88) to (3.91) can be solved to give g_{jk} and h_{jk}. Here's how.

Let $g_{jk} = ge^{i\theta}$ and $h_{jk} = he^{i\phi}$. Let $\kappa = h_{jj}h_{kk}$. Then we have

$$g^2 + h^2 = A \tag{3.92}$$

$$gh\cos(\theta - \phi) = B \tag{3.93}$$

$$gh\cos(\theta + \phi) = C \tag{3.94}$$

$$8g^2h^2 + 2\kappa\left(2g^2\cos 2\theta + 2h^2\cos 2\phi\right) = D \tag{3.95}$$

This set of equations can be reduced to a nonlinear equation of g, which is readily solved by numerical methods. The only remaining question is how many roots there are. I don't know yet.

The above equations give all correlations between all pairs a_j and a_k in terms of n_j and n_k, up to a phase choice θ_j. From this correlation matrix, using Eq (3.74), we can reconstruct an $\tilde{F}$. From previous arguments, it's guaranteed that $|\tilde{F}_{jk}| = |F_{jk}|$. However, the phase of F_{jk} cannot be reconstructed.

3.4 Gross-Pitaevskii equation simulation of driven Bose-Einstein condensates

The time-dependent Gross-Pitaevskii equation describes the dynamics of a Bose-Einstein condensate [5],

$$i\partial_t\psi = \left(\frac{\hbar^2\nabla^2}{2m} + V + g|\psi|^2\right)\psi, \tag{3.96}$$

where ψ is the condensate wavefunction, m is the atomic mass, V is the external potential, $g = 4\pi\hbar^2 a/m$ is the interaction strength, and a is the scattering length.

The Gross-Pitaevskii equation is a powerful tool to theoretically and numerically describe our experimental systems, since we work mostly with Bose-Einstein condensates. It is capable of not only describing the ground state wavefunctions, but also dynamically driven states, and even non-condensed systems through the truncated Wigner method. In this chapter I will describe an efficient numerical method for simulating the Gross-Pitaevskii equation, which allows us to microscopically directly simulate Floquet driven condensates, its extension in the presence of a density-dependent gauge field, and the truncated Wigner method which simulates quantum fluctuation using classical noise.

3.4.1 Efficient numerical simulation based on GPU-accelerated fast Fourier Transform

Numerically, the Gross-Pitaevskii equation Eq. (3.96) is discretized on a spatial-temporal grid, $\psi(x_i, t_j) \mapsto \psi_{i,j}$. Here a 1D case is used as an example, but generalization to 2D and 3D is straightforward. The temporal discretization is performed through Trotterization,

$$\psi(t + dt) = e^{-iHdt}\psi(t), \tag{3.97}$$

where $H = \frac{\hbar^2\nabla^2}{2m} + V + g|\psi|^2$ is the nonlinear 'Hamiltonian' and dt is the temporal stepsize. In principle, from here one can express the discretized wavefunction as a vector, and the Hamiltonian as a matrix. Then one need to exponentiate the Hamiltonian to solve for the dynamics. However, matrix exponentiation is computationally intensive, and the matrix size scales as the square of the grid size.

In our algorithm we overcome this challenge by utilizing the split-step Fourier method [30]. The Hamiltonian has three terms. The kinetic term $\frac{\hbar^2\nabla^2}{2m}$ is diagonal in the Fourier space, as its eigenvectors are momentum states. The external potential V and the interaction term $g|\psi|^2$ are diagonal in the real space. We perform another Trotterization,

$$e^{-iHdt} \mapsto e^{-i\frac{\hbar^2\nabla^2}{2m}dt} e^{-i(V+g|\psi|^2)dt}, \tag{3.98}$$

splitting the Hamiltonian exponentiation into a step diagonal in real space and a step diagonal in Fourier space. Exponentiation of a diagonal matrix is simply the exponentiation of each diagonal element, so the operation no longer requires matrix exponentiation, but rather reduces to element-wise exponentiation, which allows for parallelization and is computationally efficient. In each time step, we now need to Fourier transform the wavefunction into the Fourier space, and inverse Fourier transform back to real space. Denoting the Fourier transform operation as $\mathcal{F}$, the time step becomes

$$e^{-iHdt} \mapsto \mathcal{F}^{-1} e^{-i\frac{\hbar^2 k^2}{2m}dt} \mathcal{F} e^{-i(V+g|\psi|^2)dt}, \tag{3.99}$$

where k is the momentum space coordinate.

Since element-wise exponentiation is computationally cheap, the efficiency bottleneck is now the Fourier transform. Fast Fourier transform (FFT) algorithms enjoy significant speedup from GPU acceleration, for example through the CUDA toolkit cuFFT package, which we can access through Python cupy module. We can therefore easily write efficient

code in Python to simulate the Gross-Pitaevskii equation.

It is suggested that the simulation error can be further reduced by splitting the real space step into two, and put one before and one after the Fourier space step [31]. In practice the improvement I observe is not significant enough to warrant the additional complications.

The high efficiency of the algorithm allows us to perform the simulation on a large spatial grid, for a large number of temporal steps. As a result, we can directly microscopically simulate driven condensates. We can directly include the sinusoidal optical lattice in V by resolving the lattice sites with the spatial grid. We typically place 16 spatial grid steps for each lattice site. We can also directly include the interaction modulation in the time dependence of g. We typically resolve each interaction modulation period by 100 time steps.

From the time dependent Gross-Pitaevskii equation Eq. (3.96), we can also numerically obtain the ground state wavefuction, through simulated annealing. The ground state wavefunction is described by the time independent Gross-Pitaevskii equation,

$$\mu\psi = \left(\frac{\hbar^2\nabla^2}{2m} + V + g|\psi|^2\right)\psi, \tag{3.100}$$

where μ is the chemical potential. The ground state minimizes the chemical potential μ. Simulated annealing performs imaginary time evolution,

$$\psi \mapsto e^{-H\tau}\psi, \tag{3.101}$$

where τ is the imaginary time. The wavefunction is renormalized after each imaginary time step to preserve the norm. If the system were linear, it is clear that any excited state decays faster than the ground state, and after long enough imaginary time we arrive at the ground state. For our nonlinear system, this still holds in practicality.

In practice, the annealing may be 'stuck' by topological defects such as vortices, since they cannot be eliminated continuously. We 'shake' the solution out of these local minimum

by adding noise to the wavefunction before each time step. We start the annealing process with either a random initial wavefunction, or a uniform initial wavefunction. Starting with a uniform initial wavefunction results in less topological defects that need to be eliminated, but in some cases the ground state actually does contain topological defects, making a uniform initial wavefunction unsuitable.

3.4.2 Density-dependent gauge field

The Gross-Pitaevskii equation can be extended to describe condensates subject to gauge fields. We know that the Hamiltonian of a charged particle in a vector potential is

$$H = \frac{(p - A)^2}{2m}, \tag{3.102}$$

where p is the momentum, A is the vector potential and m is the particle mass. We absorb the charge into the vector potential. Therefore, the energy density of a Bose-Einstein condensate in a vector potential is

$$\mathcal{E} = \psi^* \frac{(p - A)^2}{2m} \psi + V|\psi|^2 + \frac{1}{2} g|\psi|^4, \tag{3.103}$$

where ψ is the condensate wavefunction, V is the external potential, g is the interaction strength and p is the momentum operator. The Gross-Pitaevskii equation is obtained from the energy density by applying the variational principle to the Lagrangian.

Since the vector potential A is local in real space, the kinetic term is no longer diagonal in either real space or Fourier space, and the split step Fourier method cannot be directly applied. In particular, terms such as $\psi^* A p \psi$ in the energy density results in terms such as $A\nabla\psi$ in the Gross-Pitaevskii equation. The operator $A\nabla$ in the Hamiltonian is neither diagonal in real space nor in momentum space. However, in the case of a density-dependent gauge field where $A = \eta|\psi|^2$, η being a vector representing the strength and direction of

the gauge field, the term in the Gross-Pitaevskii equation becomes $|\psi|^2\eta\nabla\psi$, which can be rewritten as $\psi^*\eta(\nabla\psi)\psi$. The corresponding operator in the Hamiltonian is now $\psi^*\eta(\nabla\psi)$, which is local in real space. We can evaluate $\nabla\psi$ in real space through the fast Fourier transform.

In summary, our algorithm using the split step Fourier method cannot deal with spatially varying static gauge fields. However, in our case with density-dependent gauge fields where the spatial dependence is only inherited from the condensate wavefunction itself, we can still apply our algorithm.

3.4.3 Truncated Wigner method

The Gross-Pitaevskii equation is supposed to describe the dynamics of a condensate. In our Bose fireworks experiment, the jets are excited out of the condensate to form two-mode squeezed states. Since the jets and the rest of the condensate do not share the same wavefunction, the Gross-Pitaevskii equation does not readily apply. This is to be expected since the jets are amplified from quantum fluctuations, whereas the Gross-Pitaevskii equation is deterministic. Remarkably, we only need a simple extension to the Gross-Pitaevskii equation to be able to simulate Bose fireworks. Instead of starting the simulation with the deterministic initial state such as the ground state in a trap, classical noise is added to the initial state. Several realizations of the classical noise is evolved using the Gross-Pitaevskii equation, and the resulting ensemble is used to calculate observable expectation values, in a Monte-Carlo manner. Heuristically we consider each realization of the noise to be one 'experimental shot', similar to how single shot in our experiment samples the amplified quantum fluctuation. This approach is called the truncated Wigner method [32]. Theoretically there is a 'correct' amount and form of classical noise that reproduces the quantum effects. In practice we hand tune the strength of noise to match experimental observations.

CHAPTER 4

DOMAIN WALL DYNAMICS DRIVEN BY DENSITY-DEPENDENT GAUGE FIELD

Emergence of exotic particles in complex many-body systems is ubiquitous in condensed matter and high energy physics. For example, mesons in quantum chromodynamics and composite fermions in fractional quantum Hall systems arise from the dynamical coupling between matter and gauge fields [33; 34]. Ultracold atoms offer a versatile platform to simulate matter-gauge interaction by creating artificial gauge fields. An important stepping stone to access the physics of the exotic emergent particles relies on the synthesis of a gauge field that depends on the matter. Here we demonstrate deterministic formation of domain walls in a stable Bose-Einstein condensate with a gauge field which is determined by the atomic density. The density-dependent gauge field is created by simultaneous modulations of an optical lattice potential and interatomic interactions, and results in domains of atoms condensed into two different momenta. Modeling the domain walls as elementary excitations, we find that the domain walls respond to synthetic electric field with a charge-to-mass ratio larger than and opposite to that of the bare atoms. Our work offers promising prospects to simulate the dynamics and interactions of novel excitations in quantum systems with dynamical gauge fields.

This chapter is based on my published work on *Nature* [35].

4.1 Introduction

Gauge theories form a cornerstone in our understanding of condensed matter systems [36] and fundamental particles [37]. A complete theoretical understanding of many-body systems subject to gauge fields, however, faces significant analytical and numerical challenges [38; 39]. Experiments with ultracold atoms offer an alternative approach by quantum simulating gauge

theory models, where gauge fields can be artificially synthesized [40; 41; 15]. Tremendous progress has been made in the past years on creating static artificial gauge fields in atomic quantum gases [42], enabling the realization of, for instance, the iconic Haldane [43] and Hofstadter models [2; 44].

Fundamentally, gauge fields are dynamical with quantum degrees of freedom that interact with matter [45; 46; 47; 48; 49]. An intriguing consequence of the dynamical feedback between the matter and gauge field is the formation of novel particle-like excitations with emergent properties, for example, mesons in the standard model [33] and composite fermions in the fractional quantum Hall effect [34]. Recently, several experiment groups have realized density-dependent gauge fields [50; 51; 52], where the strength of the field depends on the density of matter [53], as well as lattice gauge theory models [3; 54; 55].

4.2 Bose-Einstein condensate under density-dependent gauge field

We quantum simulate a Bose-Einstein condensate (BEC) subject to a density-dependent gauge field, which is described by the energy density functional

$$\mathcal{H} = \frac{1}{2m^*}|(\mathbf{p} - \mathcal{A})\psi|^2 + \frac{1}{2}g|\psi|^4, \tag{4.1}$$

where ψ is the condensate wavefunction, $\mathbf{p}$ is the momentum operator, m^* is the mass of the particle, $\mathcal{A}$ is the density-dependent gauge field, and g is the interaction strength. We engineer a gauge field that takes one of two values according to the density $n = |\psi|^2$,

$$\mathcal{A} = \hbar k^* \text{ sign}(n - n_c)\hat{x}, \tag{4.2}$$

where $k^* > 0$ is a constant, $\text{sign}(x) = x/|x|$ is the sign function and $\hbar$ is the reduced Planck constant. The gauge field is along the $+\hat{x}$ direction when the density exceeds the critical value n_c, and along $-\hat{x}$ at lower densities, see Fig. 4.1. We observe the formation of stable domain

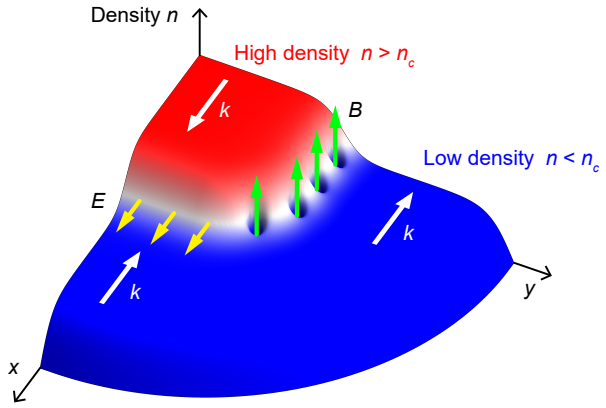

Figure 4.1: **Illustration of a Bose-Einstein condensate with density-dependent gauge field.** A condensate with inhomogeneous density profile is subject to a density-dependent gauge field $\mathcal{A}$, which changes sign when the density n exceeds a critical value n_c. The high density (red) and low density (blue) regions of the condensate form domains with distinct momenta $k = k^*$ and $-k^*$ in the $x-$direction (white arrows), respectively. Along the domain wall (white) parallel to the gauge field, an array of vortices form as a consequence of phase continuity, which is a manifestation of the effective magnetic field $B \propto \partial_y n$ (green arrows). On the other hand, dynamics of the condensate density can induce an effective electric field $E \propto \partial_t n$ (yellow arrows). In this work, we observe the formation and dynamics of domain walls perpendicular to the gauge field.

walls in the BEC, which are topological defects [56], and extract an effective charge-to-mass ratio from their dynamical response to the gauge field.

In the BEC described by Eq. (4.1), the local phase gradient of the ground state wavefunction follows the gauge field, $\partial_x \phi = k^* \text{ sign}(n - n_c)$, in order to minimize the kinetic energy. The condensate can support two types of domains with momentum $k = +k^*$ for density n exceeding the critical value n_c and momentum $k = -k^*$ for lower density $n < n_c$. The density-dependent magnetic field $\mathbf{B} = \nabla \times \mathcal{A} = -2\hbar k^* \delta(n - n_c) \partial_y n \hat{z}$ is concentrated on domain walls parallel to the gauge field, and $\delta(x)$ is the Dirac delta function . On the other hand, dynamics of the density generates an electric field $\mathbf{E} = -\partial_t \mathcal{A} = -2\hbar k^* \delta(n - n_c) \partial_t n \hat{x}$. The electromagnetic fields E and B can induce Lorentz force on the atoms, simulating charged particles in the gauge field.

4.3 Experiment setup

We load a nearly pure BEC of around 40,000 ^{133}Cs atoms into a one-dimensional (1D) optical lattice along the $x-$direction with an additional weak harmonic confinement in the $x-y$ plane at the radial trap frequency $2\pi \times 8$ Hz and a tight vertical confinement at trap frequency $2\pi \times 223$ Hz. The condensate remains in the 3D regime, with a chemical potential $2\pi \times 170$ Hz. Using Floquet engineering [57], we realize the gauge field in Eq. (4.2) by generating a tilted double well dispersion ϵ_k along the lattice direction, where the energy offset of the two wells depends on the density of the sample. The dispersion can be modeled by

$$\epsilon_k = \alpha(k^2 - k^{*2})^2 - \frac{\hbar}{m^*} kA(n). \tag{4.3}$$

Here k is the wavenumber, α and k^* can be controlled by lattice shaking along the $x-$direction, m^* is the effective mass near $k = \pm k^*$, and the gauge field $A = A_s + A_d(n)$ contains the static and density-dependent contributions A_s and $A_d(n)$, respectively, which we generate from a synchronous modulations of the lattice potential and the interatomic interaction, respectively [50], see Fig. 4.2. The presence of the gauge field A shifts the local minima of the dispersion to $k = \pm k^* + A$ to leading order.

4.3.1 Lattice shaking

We modulate the lattice position δx in time t at two frequencies according to $\delta x(t) = X_1 \sin \omega t + X_2 \sin 2\omega t$, see Fig. 4.2a, where the modulation amplitude X_1 determines α and k^* of the double well dispersion, and the amplitude X_2 imbalances the two minima [58]. The fundamental frequency ω is red detuned to the second excited band of the lattice at zero momentum, see Fig. 4.2b and supplement. The shaking induces a direct single photon coupling at frequency ω and coupling strength Ω_1, as well as a Raman coupling involving both an ω photon and a 2ω photon with coupling strength Ω_2. The direct coupling Ω_1 has an

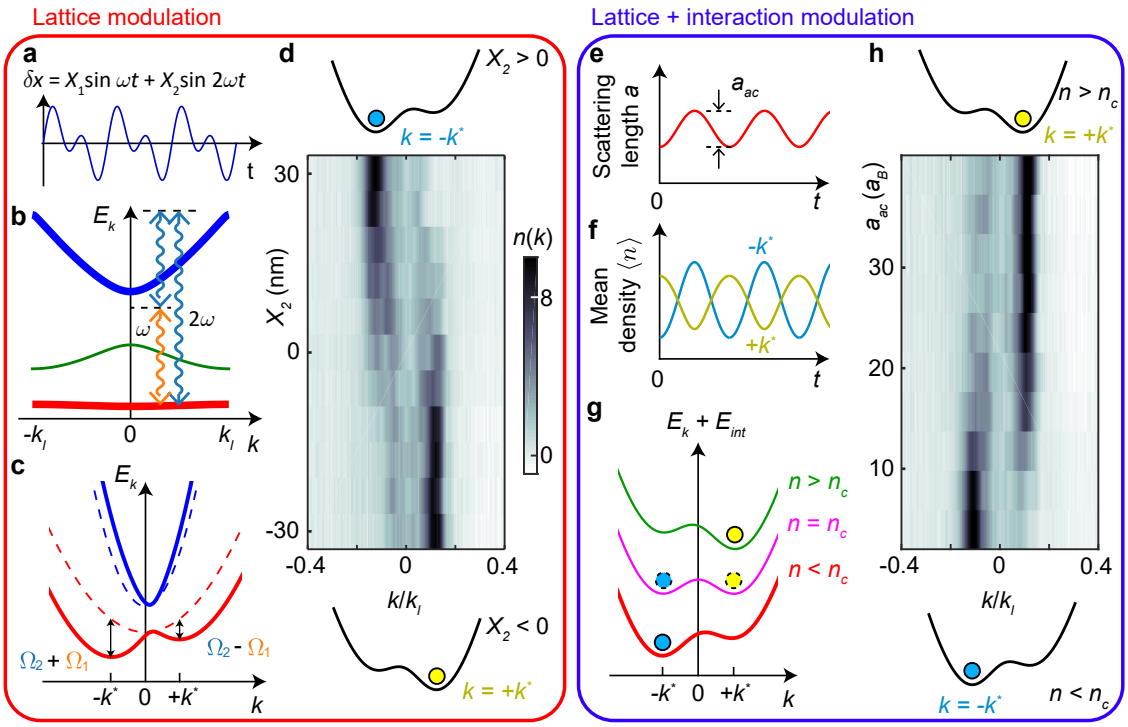

Figure 4.2: **Creation of static (a-d) and density-dependent (e-h) gauge fields. a**, We periodically translate the 1D optical lattice by $\delta x = X_1 \sin\omega t + X_2 \sin 2\omega t$ with $X_1 = 21$ nm and variable X_2. **b**, The frequency ω is slightly red detuned from the transition between the ground (red) and the second excited band (blue). The first excited band (green) is only weakly coupled. Here $k_l = \pi/(532\text{ nm})$. The shaking introduces a direct coupling Ω_1 (orange arrow) and a Raman coupling Ω_2 (blue arrows). **c**, In the Floquet picture, the two couplings destructively (constructively) interfere for positive (negative) k when $X_2 > 0$. The couplings hybridize the bare bands (dashed lines), and the resulting ground band (red line) forms a tilted double well with minima at $k \approx \pm k^* = \pm 0.15 k_l$. **d**, Time-of-flight images show a jump of the BEC momentum when X_2 flips sign. See illustrations for the dispersions with $X_2 > 0$ and $X_2 < 0$. The 1D momentum distribution $n(k)$ is normalized over the first Brillouin zone. **e**, The scattering length a is modulated at frequency ω. **f**, The micromotion of the atomic density $\langle n \rangle$ at $k = \mp k^*$ oscillates in and out of phase with the scattering length modulation. This results in a higher interaction energy for $k = -k^*$ than for $k = +k^*$. **g**, Combining both modulations yields a dispersion whose minimum position depends on the density as $k = k^* \text{sign}(n - n_c)$. **h**, The momentum distribution of the BEC displays a jump when a_{ac} exceeds 14(2) a_B. See illustrations for the dispersions with $n > n_c$ and $n < n_c$.

odd parity that only mixes states with non-zero momentum $k \neq 0$, essential for the creation of the double well dispersion, see Fig. 4.2c. On the other hand, the Raman coupling Ω_2 has an even parity. The interference of the two couplings Ω_1 and Ω_2 with opposite parities results in the imbalance of the two dispersion minima. We control the imbalance in our experiment with the amplitude of the second harmonic modulation X_2, which results in a static gauge field $A_s \propto -X_2$. See supplement for details.

The static gauge field A_s manifests in the momentum distribution of the BEC. Based on the focused time-of-flight method [59], we see that the condensate momentum indeed takes on values $k = \pm k^*$ depending on the sign of X_2, see Fig. 4.2d. For the rest of this work, we choose $X_2 = 23$ nm, which imbalances the two wells by $h \times 3$ Hz.

4.3.2 Interaction modulation

The density-dependent part of the gauge field A_d is created by modulating the scattering length a with an external magnetic field [50] at the same fundamental frequency as the lattice shaking $a(t) = a_{dc} - \frac{1}{2} a_{ac} \cos \omega t$, see Fig. 4.2e, where $a_{dc} = 50\ a_{\mathrm{B}}$ and a_{ac} are the mean scattering length and the amplitude of the modulation, respectively, and a_{B} is the Bohr radius. To understand the density dependence of the gauge field, we note that the atoms in the $k = \pm k^*$ states acquire a time dependent micromotion from the lattice shaking. Within a Floquet cycle, the atomic density of the two states $k = \pm k^*$ oscillates at frequency ω with opposite phase [50], see Fig. 4.2f. We modulate the scattering length in phase with the atomic density in the state $k = -k^*$, which raises the time-averaged interaction energy for $k = -k^*$ and lowers that for $k = +k^*$. This results in a coupling between the density and momentum, favoring the $k = +k^*$ state. The coupling gives the density-dependent part of the gauge field $A_d = \eta g_{ac} n$, where $g_{ac} = 4\pi\hbar^2 a_{ac}/m_0$ is the AC coupling constant, m_0 is the mass of the cesium atom and η can be calculated from the micromotion, see supplement.

Combining the lattice and interaction modulations, we can write the resulting gauge field

as

$$A = A_s + A_d(n) = \eta g_{ac}(n - n_c), \tag{4.4}$$

where the critical density n_c, at which the gauge field switches sign, is given by

$$n_c = \epsilon / g_{ac}, \tag{4.5}$$

and $\epsilon = -A_s/\eta$. When the atomic density exceeds the critical density n_c, the dispersion minimum switches from $k = -k^*$ to $+k^*$. For a BEC residing at the lowest energy state, its momentum also changes sign when the density exceeds the critical value, see Fig. 4.2g. Thus the BEC can be effectively described by the energy functional Eq. (4.1) with the gauge field $\mathcal{A}$ in Eq. (4.2) that has a step function dependence on the density.

To demonstrate the effect of the density-dependent gauge field, we measure the condensate momentum in the presence of both lattice and interaction modulations. We find that the condensate momentum indeed changes sign from $k = -k^*$ to $+k^*$ at $a_{ac} = 14(2)\ a_{\mathrm{B}}$, where the critical density n_c is comparable to the density of the sample, see Fig. 4.2h. Our observation is consistent with the dispersion ϵ_k in Eq. (4.3) with the density-dependent gauge field $A(n)$ in Eq. (4.4).

4.4 Domain structure and domain wall

In a trapped gas, where the condensate has non-uniform density, see Fig. 4.3a, we expect the condensate momentum to develop spatial structures in the presence of the density-dependent gauge field. In the following, we investigate the formation and dynamics of domains with different momentum in the condensate.

Starting with a regular BEC in a stationary 1D lattice, we slowly ramp up the lattice and interaction modulations over 300 ms. At the end of the ramp, the dispersion has two minima at $k = \pm k^*$ around which the effective mass is $m^* = 0.7 m_0$. The BEC has a $1/e$ lifetime

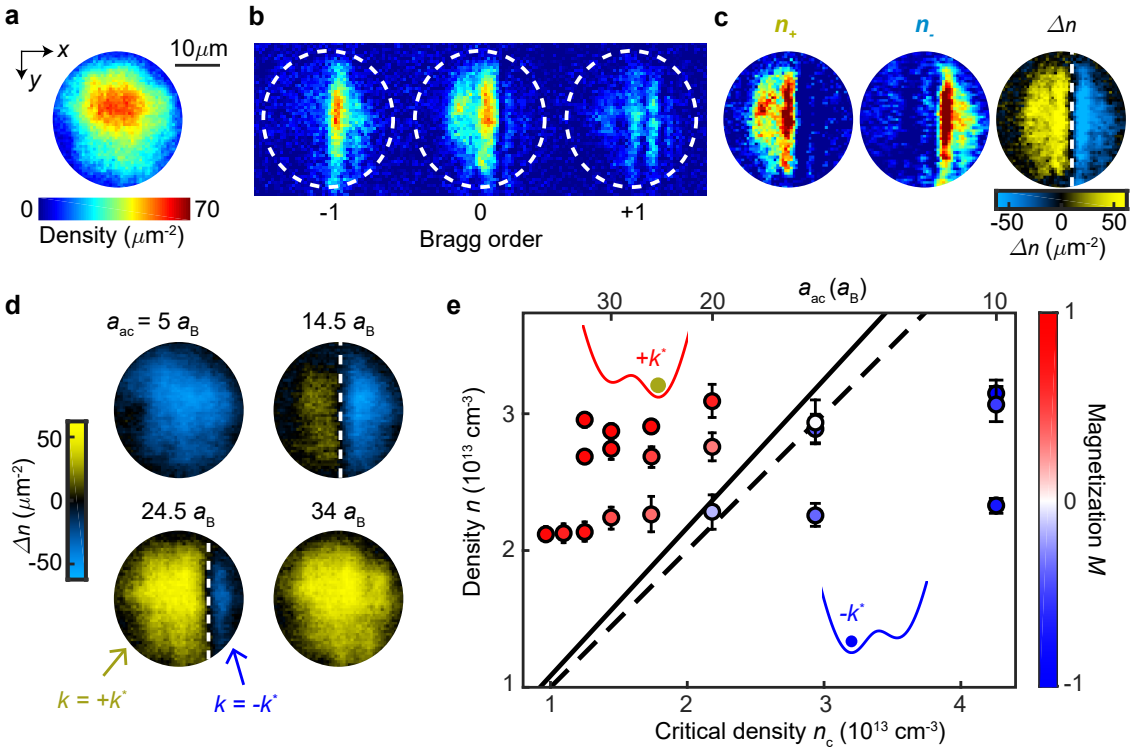

Figure 4.3: **Domains and domain walls in the presence of density-dependent gauge field.** **a**, *In situ* image of the BEC in a harmonic trap shows a nonuniform density profile. The scale bar applies to all images in panels **a-d**. **b**, The BEC is Bragg diffracted by the lattice after a 6 ms time-of-flight expansion. Atomic populations in $k = \pm k^*$ states are transferred to different Bragg orders. Here a single shot image is shown. **c**, From the image we reconstruct the density profiles $n_\pm(\mathbf{r})$ of the $\pm k^*$ domains. The difference $\Delta n = n_+ - n_-$ reveals the domain structure, and $\Delta n = 0$ indicates the domain wall (white dashed line). **d**, Examples of the domain structure are shown at various modulation amplitudes a_{ac}. Each image is an average over 15 realizations. **e**, The magnetization M near the center of the cloud is compared for different critical density n_c and atomic density n. The dotted line indicates the predicted location for $M = 0$, with $n = n_c = \epsilon/g_{ac}$ and $\epsilon = h \times 21.5$ Hz. Experimental fit (solid line) yields $\epsilon_{\text{exp}} = h \times 23(1)$ Hz. See supplement for details. Each data point is an average of 15 samples. Error bars denote one standard deviation.

of 700 ms under the driving. We measure the spatial distribution $n_{\pm}(\mathbf{r})$ of the atoms in the $k = \pm k^*$ states by first transferring the population in the two states to different Brillouin zones, followed by a short time-of-flight which maps the population to different Bragg orders [60], see Fig. 4.3(b,c) and supplement. Domain structures of the condensate are revealed by the density difference $\Delta n(\mathbf{r}) = n_+(\mathbf{r}) - n_-(\mathbf{r})$.

For moderate interaction modulation amplitudes $14\ a_B < a_{ac} < 25\ a_B$ we observe regions of atoms in the same momentum state separated by a domain wall in over 90% of the samples, see Fig. 4.3d. The separation of domains results from effective ferromagnetic interactions between the $+k^*$ and $-k^*$ states [61]. The domain wall forms perpendicular to the lattice direction. We do not observe parallel domain walls with the predicted vortex arrays, likely due to their higher energy cost under our conditions. In addition, we see that the left (right) side of the condensate tends to occupy rightward (leftward) momentum, see Fig. 4.3d, which we attribute to the shrinkage of the cloud during the ramp that preferentially pulls atoms towards the center. See supplement for details. The position of the domain wall depends on the density and the interaction modulation amplitude a_{ac}, providing a test of the strength of the density-dependent gauge field.

We analyze the momentum distribution in the condensate through the local magnetization defined as

$$M(\mathbf{r}) = \frac{n_+(\mathbf{r}) - n_-(\mathbf{r})}{n_+(\mathbf{r}) + n_-(\mathbf{r})}. \tag{4.6}$$

A value of $M = +1$ indicates that all atoms condense in the $+k^*$ state, $M = -1$ indicates the condensate in the $-k^*$ state, and $M = 0$ indicates a domain wall.

We perform the experiment with different atom numbers and modulation amplitudes a_{ac}. We extract the magnetization M near the center of the condensate for various atomic density $n = n_+ + n_-$ and critical density $n_c = \epsilon/g_{ac}$, see Fig. 4.3e. We find that the local momentum indeed settles to $+k^*$ for densities exceeding n_c, and to $-k^*$ for $n < n_c$. From the experimental data we also extract the coefficient ϵ, and the result $\epsilon_{\mathrm{exp}} = h \times 23(1)$ Hz is

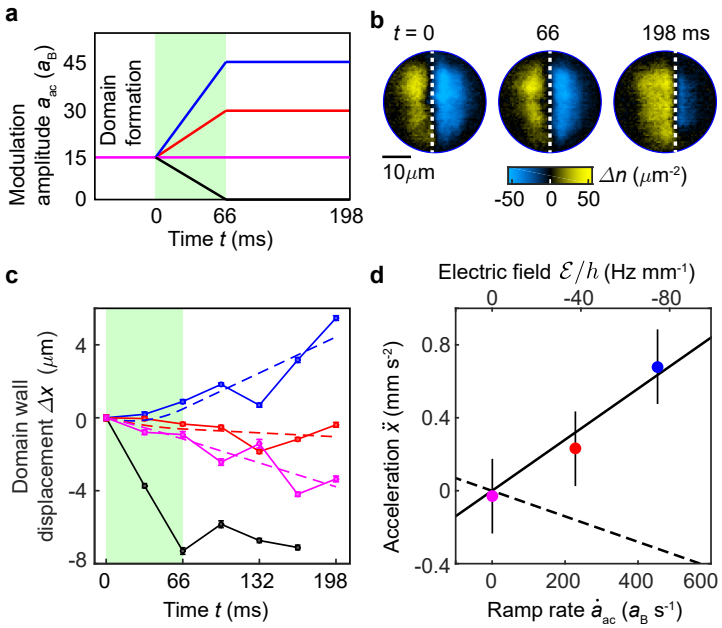

Figure 4.4: **Dynamics of the domain wall in response to a synthetic electric field $\mathcal{E}$.** **a**, After forming the domains at modulation strength $a_{ac} = 15\ a_B$, we ramp to $a_{ac} = 0$ (black), 15 (magenta), 30 (red) or 45 a_B (blue) over 66 ms and hold for 132 ms. The ramp induces an electric field $\mathcal{E} \propto \dot{a}_{ac}$ (green shaded area). Example images for the ramp to $a_{ac} = 45\ a_B$ are shown in **b**. The white dashed lines mark the positions of the domain walls. Each image is the average of 15 samples. Panel **c** shows the domain wall dynamics; dashed lines are fits based on Eq. (4.8). The black data points are excluded from the fit because the domain wall moves out of the cloud. **d**, The acceleration $\ddot{x}$ extracted from the fit shows a linear dependence on the ramp rate $\dot{a}_{ac}$ and the electric field $\mathcal{E}$. The linear fit $\ddot{x} = \beta \dot{a}_{ac}$ (black line) gives $\beta = -26(6)$ ms^{-1}. The prediction for bare atoms gives $\beta_{\text{atom}} = 13$ ms^{-1} (dashed line). Error bars indicate one standard deviation.

in good agreement with the prediction $\epsilon = h \times 21.5$ Hz.

4.5 Domain wall dynamics

The deterministic formation of domains offers an opportunity to study the domain walls as elementary objects, which is of fundamental interest to condensed matter physics [62], high energy physics [63] and cosmology [64]. We introduce a phenomenological model that describes the domain wall as an elementary excitation with charge Q and mass M interacting

with the same gauge field $\mathbf{A}$ experienced by the underlying atoms, with energy

$$E = \sigma\Lambda + \frac{(\mathbf{P} - Q\mathbf{A})^2}{2M}, \tag{4.7}$$

where $\mathbf{P} = M\mathbf{v} + Q\mathbf{A}$ and $\mathbf{v}$ are the canonical momentum and the velocity of the domain wall, Λ is the area of the domain wall, the surface tension $\sigma = \frac{8}{3}\varepsilon n/k^*$ is calculated in [56], and ε is the barrier height of the double well dispersion. For our parameters $\varepsilon = h \times 4$ Hz and the rest energy of the domain wall $\sigma\Lambda$ is $\approx k_B \times 1$ nK per atom in the domain wall.

For our observed domain walls perpendicular to the lattice along the $x-$axis, their motion is restricted to the same direction. The dynamics is driven by the Lorentz force with only the electric field in the $x-$direction $\mathcal{E} = -\partial_t A$, with A given in Eq. (4.4). We derive

$$\begin{aligned} \ddot{x} &= \frac{Q}{M}\mathcal{E} \\ \mathcal{E} &= -\frac{\partial\eta(g_{ac}n - \epsilon)}{\partial t}. \end{aligned} \tag{4.8}$$

To study the dynamical response of the domain wall to the electric field $\mathcal{E}$, we ramp the density-dependent gauge field and monitor the motion of the domain wall. After preparing one domain wall in the BEC at the modulation strength $a_{ac} = 15\ a_{\mathrm{B}}$, we ramp a_{ac} to different values over 66 ms, which induces an electric field $\mathcal{E}$. We then hold for another 132 ms during which the domain wall can freely propagate, see Fig. 4.4a.

We observe that the domain wall moves in the lattice direction in response to the ramp, see Fig. 4.4(b,c), consistent with the direction of the electric field. The motion persists in the same direction after the ramp stops. From Eq. (4.8) we expect that the domain wall accelerates during the ramp $\ddot{x} = \beta\dot{a}_{ac}$, where $\beta \propto Q/M$, and maintains a constant velocity during the hold time. (The atomic density n remains almost a constant to within 20% during the dynamics, and η and ϵ are constants.) We fit the domain wall trajectories to extract the acceleration $\ddot{x}$, which indeed shows a linear dependence on the ramp rate $\dot{a}_{ac}$,

see Fig. 4.4d. From the linear fit we extract the charge-to-mass ratio of the domain wall to be $Q/M = -2.8(7)\ {m_0}^{-1}$, where m_0 is the mass of a cesium atom.

Our measurements present an interesting result where the topological defect in the BEC with density-dependent gauge field behaves very differently from the bare atoms. A bare atom residing near a local minimum of the double-well dispersion described in Eq. (4.3) also accelerates under the electric field $\mathcal{E}$ because the gauge field A shifts the minima to $k = \pm k^* + A$. To leading order in the electric field $\mathcal{E}$ the charge-to-mass ratio of an atom is $1/m^* = 1.4\ {m_0}^{-1}$. This suggests that the electric field propels the domain wall in the opposite direction compared to the bare atoms at 2.0(5) times the acceleration. Notably, the direction of domain wall motion is consistent with the condensate relaxing to the momentum state with lower energy. A quantitative understanding of the different responses between the domain wall and the bare atoms demands further theoretical and experimental investigation.

In summary, we demonstrate deterministic creation of domain walls in a BEC with density-dependent gauge field, created by simultaneous modulations of the lattice potential and the interaction strength. The domain walls remain stable in the BEC and behave like elementary excitations. Their dynamical response to the gauge field is observed to be drastically different from the bare atoms. Our work offers promising prospects of Floquet engineering of optical lattices and atomic interactions as a powerful tool to simulate the dynamics and interactions of topological defects such as domain walls and vortex lines. Synthesis of dynamical gauge fields that respect local gauge symmetry can also be realized with Floquet engineering of spin-dependent optical lattices [65].

4.6 Additional details

4.6.1 Floquet engineering of the gauge fields A_s and A_d

An atom in our shaken optical lattice evolves according to the following Hamiltonian,

$$H = \frac{p^2}{2m} + \frac{U}{2}\cos k_0(x - \delta x),$$

where p is the 3D momentum of the atom, U is the lattice depth, k_0 is the lattice wavenumber, $\delta x = X_1 \sin\omega t + X_2 \sin 2\omega t$ is the lattice displacement. On the single particle level, the dynamics in the $y-$ and $z-$ direction are decoupled, and we focus on the $x-$ direction. The time dependent Hamiltonian has discrete translational symmetry of the lattice, and the Hamiltonian separates for different quasi-momentum quantum numbers k as $H = \bigotimes_k H(k)$. We numerically calculate the dispersion of the Floquet bands by diagonalizing the Floquet operator $U_F(k) = e^{-i\int_0^T H(k)dt}$ in momentum space, including the first 15 bands in the Hilbert space, and Trotterizing the time evolution into 100 steps.

The operator is diagonalized as $U_F(k) = \sum_j e^{-i\epsilon_j(k)T/\hbar}|\psi_j(k)\rangle\langle\psi_j(k)|$. The eigenvalues $\epsilon_j(k)$ are the quasi-energies, giving the effective dispersion of the hybridized bands. The eigenvectors contain the micromotion of the Floquet eigenstates $|\Psi_j(k,t)\rangle = e^{-i\int_0^t H(k)d\tau}|\psi_j(k)\rangle$, from which we calculate the micromotion of the density $\langle n(t)\rangle = \int |\Psi_j(x,t)|^4 dx$ shown in Fig. 4.2f.

The scattering length is modulated as $a(t) = a_{dc} - \frac{1}{2}a_{ac}\cos\omega t$. The time averaged interaction energy (chemical potential) is $E_{\text{int}} = \frac{N}{V}\frac{1}{T}\frac{4\pi\hbar^2}{m_0}\int\langle n(t)\rangle a(t)dt$, for N atoms in volume V, corresponding to experimentally measured atomic density N/V, which is averaged over length scales larger than the lattice constant.

Comparing the interaction energy E_{int} for $k = \pm k^*$ states, we obtain the factor η in the expression of the density-dependent gauge field A_d Eq. (4.4). This approach treats the interaction effects to zeroth order in perturbation since we neglect the deviation in density

profile from the single particle eigenstates due to interactions.

Analytically we can obtain a qualitative understanding of the creation of the tilted double well dispersion from perturbation theory. Performing the Jacobi-Anger expansion on the lattice potential, we arrive at

$$H = -\frac{\hbar^2}{2m}\partial_x^2 + \frac{U}{2}\cos k_0 x + H_1 = H_0 + H_1,$$

where H_0 describes the static lattice, and H_1 describes the driving,

$$H_1 = \frac{U}{4}(e^{ik_0 x} f + e^{-ik_0 x} f^*),$$

$$f = -\frac{1}{4}(\alpha^2 + \beta^2) + 2i\alpha \sin\omega t - 2\alpha\beta\cos\omega t.$$

Here $\alpha = k_0 X_1$, $\beta = k_0 X_2$, and we keep terms up to second order in α and β, and up to ω in frequency.

The eigenstates of H_0 are the Bloch waves. Consider the states $|0, k\rangle$ and $|2, k\rangle$ in the ground and second excited bands at quasimomentum k. Under rotating wave approximation, the effective Hamiltonian is

$$H_{\text{eff}} = \begin{pmatrix} E_0 & \Omega \\ \Omega^* & E_0 + \Delta \end{pmatrix},$$

where $E_0 = \langle 0, k|H_0|0, k\rangle$ is the bare energy of the ground band, Δ is the detuning, and the coupling is

$$\Omega = \alpha\Omega_- - \alpha\beta\Omega_+.$$

Here $\Omega_\pm = \langle 0, k|e^{ik_0 x} \pm e^{-ik_0 x}|2, k\rangle$. From here we can see that the coupling has two contributions, one is the direct coupling $\Omega_1 = \alpha\Omega_-$, the other is the Raman coupling $\Omega_2 = -\alpha\beta\Omega_+$. The parity of Ω_- is odd, and that of Ω_+ is even, because the ground and second excited bands both have even parity wavefunctions.

Near $k = 0$, to first order the matrix elements depend on quasimomentum k as $\Omega = \alpha\omega_0 k - \alpha\beta\omega_1$, $E_0 = \epsilon_0 k^2$ and $\Delta = \epsilon_1 k^2 + \Delta_0$. Then the hybridized ground band dispersion is

$$E_g = \epsilon_0 k^2 + \frac{1}{2}\left(\epsilon_1 k^2 + \Delta_0 - \sqrt{4(\alpha\omega_0 k - \alpha\beta\omega_1)^2 + (\epsilon_1 k^2 + \Delta_0)^2}\right).$$

The dispersion has the shape of a double well because the coupling has a zero crossing near $k = 0$. Since the fundamental shaking frequency is red detuned, the coupling pushes down the ground band energy. The tilt is a result of the constructive and destructive interference of Ω_1 and Ω_2 at positive and negative quasi-momentum, which pushes down the ground band energy more on one side than the other. To lowest order, this tilt is given by a linear term in the dispersion $2\alpha^2\beta\omega_0\omega_1 k/\sqrt{4(\alpha\beta\omega_1)^2 + \Delta_0^2}$, which effectively generates a static gauge field $A_s \propto \beta = k_0 X_2$. The sign of the gauge field depends on the phase between the X_1 and X_2 lattice modulation components.

The numerical Floquet calculation indicates that the modulation weakly couples the ground band to the first excited band in addition to the second excited band. The coupling to the first excited band mostly contributes to a constant energy shift, and does not qualitatively change the shape of the dispersion.

4.6.2 System preparation

In our experiment, the optical lattice is formed by a pair of counter-propagating 1064 nm lasers, with lattice constant 532 nm. We use parameters lattice depth $U = 8.9E_R$, where $E_R = h \times 1.3$ kHz is the recoil energy, and $\omega = 2\pi \times 9091$ Hz. Under our conditions, the factor η in Eq. (4.4) is $\eta = 0.07m^*/\hbar k^*$, where $m^* = 0.7m_0$ and $k^* = 0.15k_l$.

After loading the atoms into the 1D optical lattice with harmonic confinement formed by 1064 nm lasers, we prepare the BEC under density-dependent gauge field by slowly ramping up the modulation amplitudes. We ramp up the amplitude X_1 to 7 nm over 11 ms (100 oscillation periods). Since the critical shaking amplitude for the formation of double

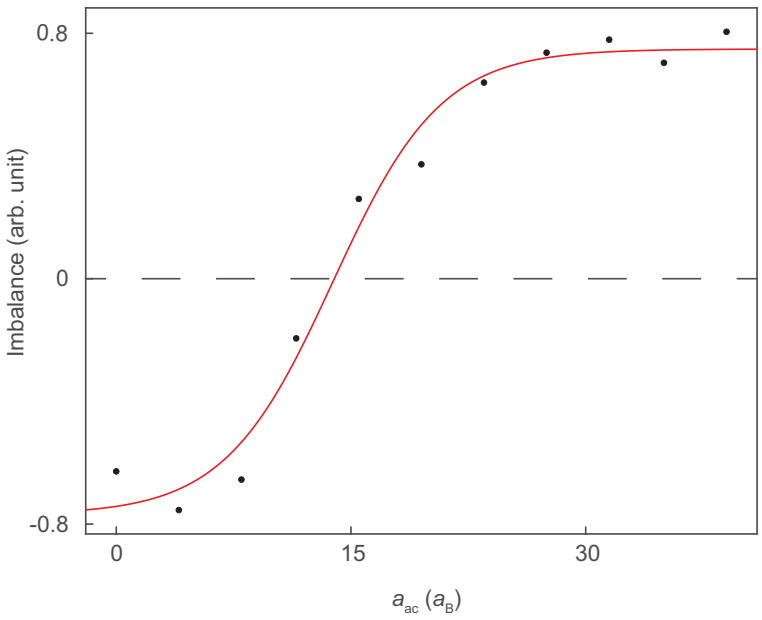

Figure 4.5: Fit to the population imbalance between the $\pm k^*$ states in Fig 2h for the estimation of the zero-crossing position.

well dispersion is 14 nm (obtained from the Floquet calculation of dispersion), the effective dispersion changes very little during this time, and we ramp quickly to reduce particle loss. We then ramp up the amplitude X_1 to 21 nm over another 289.3 ms (2630 oscillation periods), which gives a ramp rate slow enough to suppress fluctuations from the Kibble-Zurek mechanism [60] and allow for deterministic evolution of the system. The amplitudes X_2 and a_{ac} are ramped to the final value over the first 11 ms. This ramp procedure turns on the gauge field slowly over time, and results in a roughly constant critical density n_c throughout the ramp.

In Fig. 4.2h, the modulation amplitude at which the BEC momentum changes sign is estimated to be 14(2) a_{B}. To obtain this value, we fit the momentum space distribution with two Gaussians and extract the population imbalance between the $\pm k^*$ states. We plot the imbalance against the modulation amplitude a_{ac} and fit with a hyperbolic tangent curve, see Fig. 4.5. From the fitted position of the zero-crossing we obtain the value 14(2) a_{B}.

Although the dynamics during the ramp on of the gauge is deterministic, it is not quite

adiabatic since the two momentum minima are only offset by $h \times 3$ Hz, comparable to the ramp time 300 ms, and we do not arrive at the ground state. During the ramp fields, the cloud systematically shrinks, in part due to particle loss which reduces the chemical potential, and in part due to the reduction of quantum pressure as the dispersion crosses the critical point from parabolic to double well, during which the effective mass diverges and the quantum pressure drops to zero. Since we are in the Thomas-Fermi regime, the quantum pressure is usually negligible, but in this case its reduction is significant enough to bias the domain formation because a slow ramp across the critical point is very susceptible to any bias. We have confirmed this effect in experiments with no gauge field (balanced double well dispersion), and in numerical simulations without particle loss.

In Fig. 4.3e, we repeat the experiment at three different total particle numbers $4.8, 3.6, 2.5 \times 10^4$. The data shown in Fig. 4.3(a-d) are from the dataset with particle number 4.8×10^4.

4.6.3 Extracting the domain densities from Bragg peaks

We extract the spatial distribution of the atoms in the $k = \pm k^*$ states following the technique in [60]. At the time of detection, we switch off X_2 and a_{ac} and ramp the modulation amplitude X_1 to 140 nm over 0.8 ms. This pulse of lattice shaking excites the atoms from the ground band to superposition states of excited bands at the same quasi-momentum, which have oscillating projections to each Brillouin zone. Atoms in different quasi-momentum states have different oscillations. We image the atoms at the time when the projections of $k = \pm k^*$ states are maximally different. We perform a 6 ms time-of-flight to map the Brillouin zones to Bragg diffraction orders.

The densities in the Bragg diffraction orders

$$\vec{n}(x, y) = (n_{-1}(x, y), n_0(x, y), n_1(x, y)) \,,$$

is the sum of the contributions from atoms in the $k = \pm k^*$ states,

$$\vec{n} = n_+ \hat{e}_+ + n_- \hat{e}_-,$$

where the basis vectors $\hat{e}_\pm$ describe the distribution over the three Bragg diffraction orders of atoms in the $k = \pm k^*$ states. We calibrate the basis vectors $\hat{e}_\pm$ by biasing the entire condensate into $k = \pm k^*$ and performing the same time-of-flight measurement. The basis vectors $\hat{e}_\pm$ are L^1 normalized such that the components sum to 1. We determine the densities $n_\pm$ by fitting under the positivity constraint $n_\pm > 0$.

The Bragg peaks of atoms in the $k = \pm k^*$ states are shifted relative to each other during the TOF, because of the difference in quasi-momentum. We take this shift into account when reconstructing the domain densities. Additionally, this shift may cause originally disjoint domains to overlap during the TOF. The coherent domains interfere in the overlapping region, forming density waves at wavenumber $2k^*$. This effect does not significantly alter the extracted domain structure or domain wall position, and we neglect it in our analysis.

4.6.4 Analysis of the domain structures

Since we observe that the domain walls are mostly perpendicular to the lattice direction, in our analysis we treat the domain structures as 1D. For the analysis in Fig. 4.3e of the main text, we integrate the mean and difference of the domain densities, $n = n_+ + n_-$ and $\Delta n = n_+ - n_-$, over the $y-$direction, then select the central 10% of the cloud. Effectively we select a central vertical stripe of the cloud. We have checked that our results are not sensitive to the chosen stripe width. From each experimental realization we calculate the magnetization $M = \Delta n/n$, and we plot the average of n and M for each set of modulation amplitude a_{ac} and particle number N. We convert the 1D density to 3D density by dividing with the length scales in the y and z directions, l_y and l_z. Since the chemical potential is not

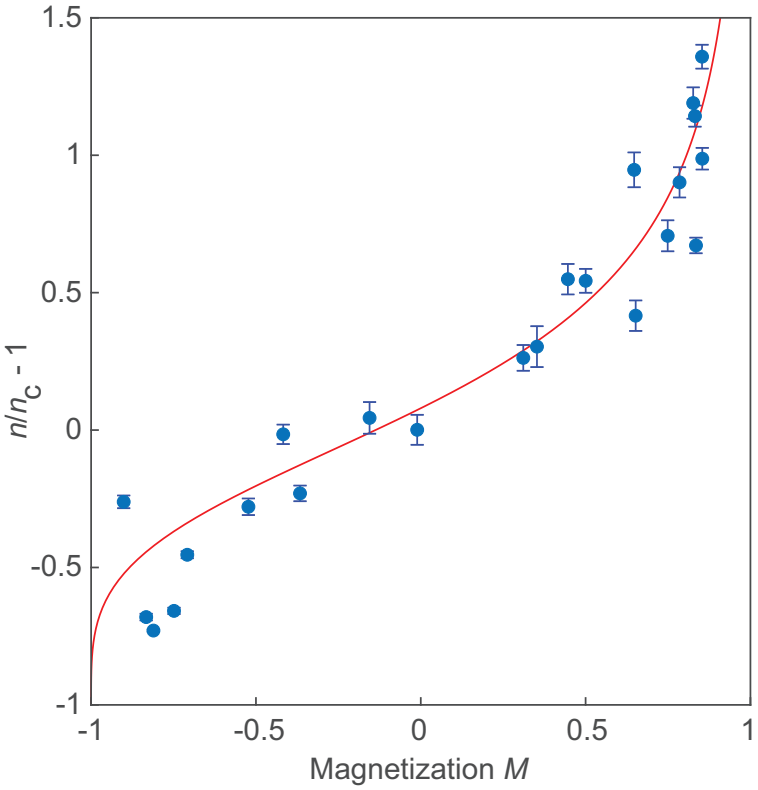

Figure 4.6: Fit to experiment data in Fig. 3e for the extraction of ϵ_{exp}.

larger than the trap frequency in the $z-$direction, we use the length scale of the harmonic oscillator ground state $l_z = \sqrt{h/m\omega}$. We obtain the length scale $l_y = (\int ndy)^2 / \int n^2 dy$ from the measured density profiles n.

From the experiment data in Fig. 4.3e, we extract a value of ϵ_{exp} in Eq. (4.5) by fitting to the expression

$$M = \tanh \frac{\ln n - \ln(\epsilon_{\text{exp}}/g_{ac})}{C},$$

with each data point in Fig. 4.3e corresponding to a magnetization M, a density n, and a modulation strength g_{ac}. This expression represents the relation $M = \text{sign}(n - \epsilon_{\text{exp}}/g_{ac})$, but smooths the step function by a width parameter C. We present our fit to experiment data in Fig. 4.6.

For the analysis in Fig. 4.4c, we integrate the difference of the domain densities Δn over the $y-$direction. We then extract the position of the zero crossing of the integrated 1D

domain density, by fitting a straight line to the six data points (each corresponding to a pixel in the image) around the numerical zero crossing, in order to improve accuracy. The error bars shown in Fig. 4.4c are 68% confidence intervals of this fit. With this procedure we determine the domain wall position with an uncertainty of around 0.3 microns.

We fit the domain wall trajectories in Fig. 4.4c by assuming a common initial velocity for all ramp rates, a constant acceleration during the ramp which is independently varied for each ramp rate, and a constant velocity after the ramp stops. The fitted initial velocity is $-17(10)$ $\mu m/\mathrm{s}$, which we attribute to residual dynamics during the domain formation process.

The conversion of the ramp rate $\dot{a}_{ac}$ to the electric field $\mathcal{E}$ is derived from Eq. (4.4). We have

$$\mathcal{E} = \frac{4\pi\hbar^2}{m_0} n\eta\dot{a}_{ac},$$

with density $n = 2.8 \times 10^{13}$ cm^{-3} from the experiment. The prediction of parameter β for bare atoms is obtained from this relation and the charge-to-mass ratio $1/m^*$.

CHAPTER 5

MANY-BODY ECHO OF PARAMETRICALLY AMPLIFIED MATTER-WAVE

5.1 Introduction

Reversibility of many-body dynamics is a highly debated question over the past 100 years. While thermal ensembles evolve toward states with high entropy, dictated by the second law of thermodynamics. Evolutions that reverses the dynamics toward the initial state are permitted by physics laws that govern the microscopic interactions of particles.

In quantum mechanics, the recipe of reversing dynamics is in principle straightforward. Evolution from an initial state $|i\rangle$ to the final state $|f\rangle = U|i\rangle$ is given by the unitary operator $U = e^{-iHt/\hbar}$, where H is the Hamiltonian, t is the time and $\hbar$ is the Planck constant. To evolve the system back to the initial state, we only need to reverse the sign of the Hamiltonian $H \to -H$ because of the identify $e^{iHt/\hbar}e^{i-Ht/\hbar} = 1$.

Practically the challenges to perform reversal are two folds. First of all, the reversal process can be extremely sensitive to imperfect control of the Hamiltonian, especially for interacting systems that couple to many degrees of freedom, examples include chaotic system and quantum critical dynamics. See Fig. 5.1a. Second, the fidelity of reversal is frequently exponentially suppressed in the limit of large particle number and long evolution time.

To quantify the fidelity of reversing many-body quantum dynamics, one introduces the Loschmidt echo as the probability to bring the system back to the initial state

$$L = |\langle i|e^{iH't/\hbar}e^{-iHt/\hbar}|i\rangle|^2, \tag{5.1}$$

where $H' = -H + \delta H$ is assumed to slightly deviate from $-H$ by the imperfection δH. The effectiveness of second law comes from the conjecture that the presence of imperfection

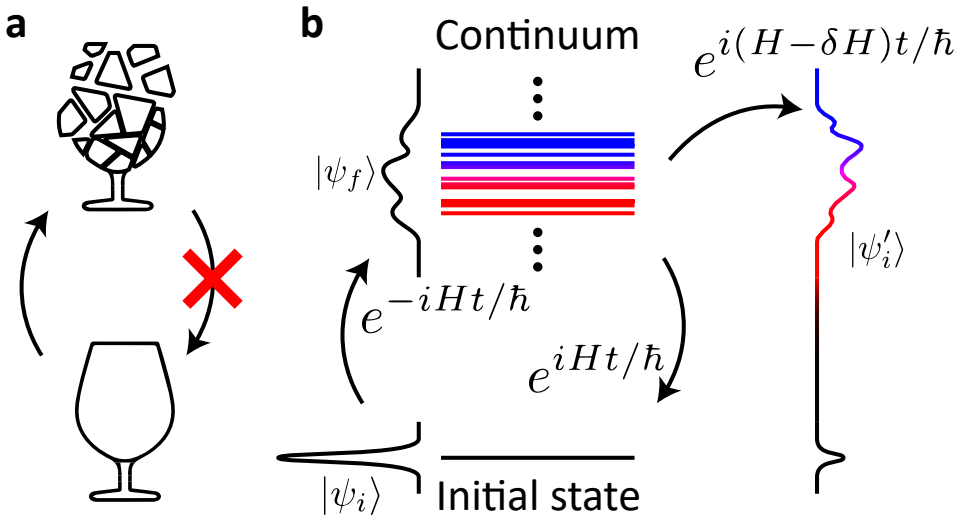

Figure 5.1: **Difficulty in reversing complex many-body dynamics.** **(a)** A broken glass does not spontaneously come together, which is an example of irreversible many-body classical dynamics. **(b)** Time evolution of a complex many-body quantum system $e^{-iHt/\hbar}$ takes a well-prepared initial state $|\psi_i\rangle$ to a final state $|\psi_f\rangle$ spread across a continuum, formed by a large number of states with different energies. Successful time reversal of the dynamics requires precise inversion of the Hamiltonian $H \to -H$. In a realistic scenario, the Hamiltonian is inverted imperfectly $H \to -H + \delta H$. The phase of the system is scrambled in the continuum and the reversal is ineffective, ending in a state $|\psi_i'\rangle$ away from the initial state.

strongly suppressed the probability to observe any success of reversal in the limit of large particle number (large particle number) and long evolution time. For system that are classically chaotic, in the critical regime, Loschmidt echo is expected follow $L \to \exp(-\alpha N \delta H t)$, where α is a constant.

5.2 Experiment setup

In our experiment, we load a nearly pure BEC of around 40,000 ^{133}Cs atoms into a two-dimensional (2D) circular box trap, with vertical trap frequency $\omega_z = 2\pi \times 826$ Hz and radius R around 20 μm. The box is deep enough to confine the BEC, but not to confine the excitations, such that the unbound excitations form a continuum. The condensate is in the quasi-2D regime, with a low chemical potential $\mu < h \times 15$ Hz. We modulate the

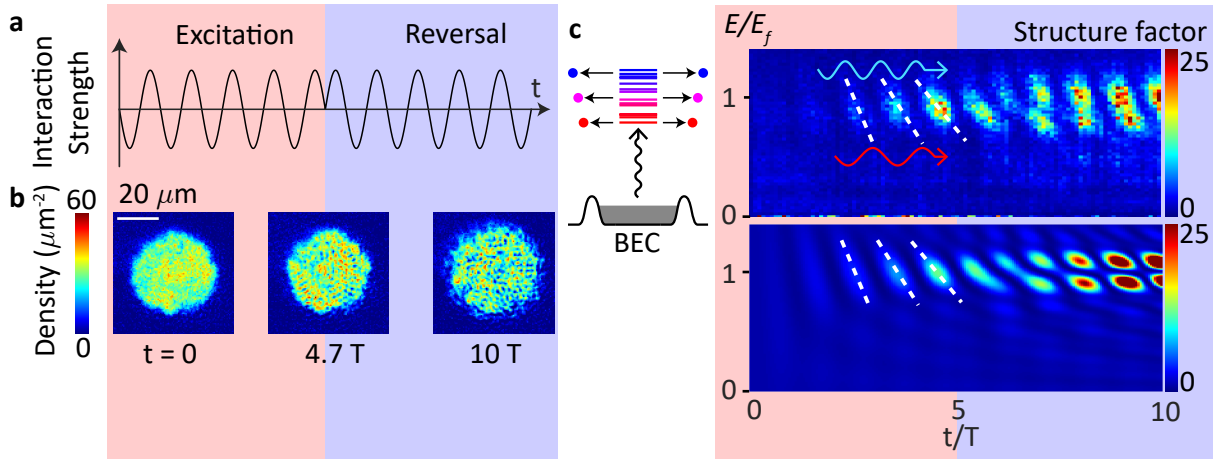

Figure 5.2: **Difficulty in reversal of Bose fireworks due to dephasing.** **(a)** We periodically modulate the interaction strength at frequency $f = 500$ Hz to excite the system (red). Afterwards we invert the driving to reverse the driven dynamics (blue). **(b)** The disk shaped BEC is nearly uniform before driving ($t = 0$). After the excitation pulse, the BEC develops strong excitations in the form of density waves ($t = 4.7T$). At the end of the reversal pulse, the excitations remain strong ($t = 10T$). The images are examples of single shots. **(c)** The diagram on the left illustrates that the BEC is coupled to a continuum of excited pairs of particles with opposite momentum. We show the time evolution of the structure factor for momentum modes with different energy E in the experiment (top) and simulation (bottom). The resonance energy is denoted by $E_f = hf/2$. White dashed lines mark the phase gradient across excitations with different energy. The higher energy modes exhibit faster phase winding (blue wavy arrow) than the lower energy modes (red wavy arrow). The experiment data is averaged over 2 repetitions.

interaction strength at frequency f through an oscillating magnetic field near a Feshbach resonance[7]. The modulation induces stimulated emission of pairs of atoms in the BEC into counter-propagating momentum modes, a process called Bose fireworks[17]. Since the unbound momentum modes form a continuum, there is not only a resonant process exciting the modes with energy $E_f = hf/2$, but also off-resonant processes exciting modes with detuned energy $E = E_f + \Delta$. The pair production process leads to two-mode squeezed states in the momentum continuum. These states are maximally entangled, and the reduced density matrix of each individual momentum mode is thermal with large subsystem entropy[18]. The Hamiltonian is

$$H = \sum_{\mathbf{k}} \Delta_{\mathbf{k}} a^\dagger_{\mathbf{k}} a_{\mathbf{k}} + g(a^\dagger_{\mathbf{k}} a^\dagger_{-\mathbf{k}} + a_{\mathbf{k}} a_{-\mathbf{k}})). \tag{5.2}$$

5.3 Simple reversal

We attempt to reverse the many-body dynamics by inverting the modulation, see Fig. 5.2a. Under rotating wave approximation, the inverted modulation corresponds to inverting the interaction term g in the Hamiltonian Eq. (5.2). We record the evolution by imaging the density waves that develop in the BEC, which result from the interference between the excited atoms and the BEC[19], see Fig. 5.2b. From the density wave patterns we extract the structure factor $S_{\mathbf{k}} = \langle (a_{\mathbf{k}} + a^\dagger_{-\mathbf{k}})(a_{-\mathbf{k}} + a^\dagger_{\mathbf{k}}) \rangle$, which measures the quadrature of the momentum modes. See supplement for details.

Time evolution of the structure factor $S_{\mathbf{k}}$ for momentum modes with different energies E reveals that excited atoms occupy many modes with different detuning develop different phases, with blue detuned modes advancing faster than red detuned modes, see Fig. 5.2c. During the reversal pulse, only the resonant modes have their excitations reversed, whereas the off-resonant modes are excited even further. The theoretical calculation predicts that the resonant mode can be almost perfectly reversed back to the vacuum, while the population in off-resonant modes grows exponentially. The poor reversal of many-body dynamics is a consequence of not inverting the detuning term $\Delta_{\mathbf{k}}$ in the Hamiltonian Eq. (5.2), which is an example of Loschmidt echo.

Previous studies have shown that a simple reversal scheme like that shown in Fig. 5.2 can only reverse as much as 20% of excited atom population[18], limited by the detuning $\Delta_{\mathbf{k}}$. There has been several theoretical proposals on improving the reversal efficiency. Careful adjustments of the reversal pulse is proposed to mitigate the effect of counter-rotating terms under strong driving[20]. A formulation of the many-body dynamics in terms of the SU(1,1) group revealed a general class of time reversal schemes[21]. However, these schemes do not

offer a significant improvement in reversal efficiency in our experiment, because they do not address the core issue of combating the detuning in the continuum.

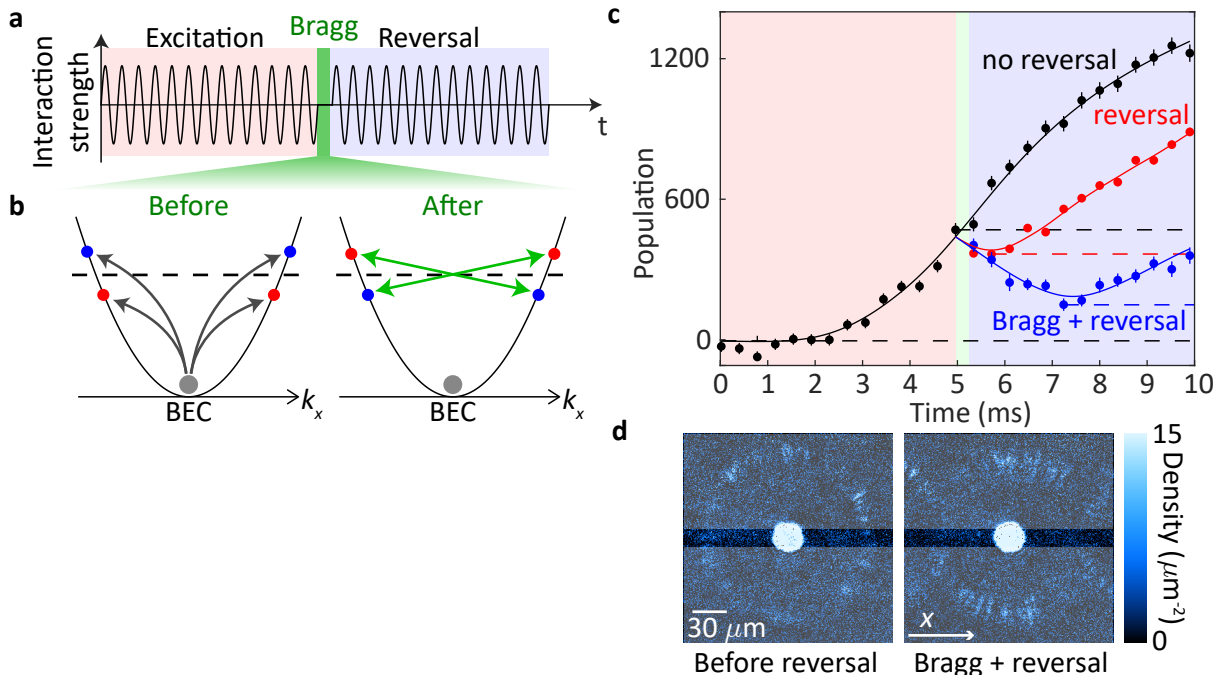

Figure 5.3: **Many-body echo.** **(a)** A pulse of interaction modulation excites the system (red), followed by a Bragg pulse of optical lattice (green). Another pulse of interaction modulation reverses the dynamics (blue). **(b)** During the excitation pulse, pairs of atoms are excited from the BEC (gray). Some pairs (blue) have higher energy than the resonance (dashed line), while some have lower energy (red). The Bragg pulse (green arrows) swaps excitations in blue and red detuned modes. **(c)** Single shot images from the experiment illustrate the effect of the Bragg pulse. The red boxes show the region of interest in which we count the population of excited atoms for **d**. **(d)** We monitor the evolution of excitation population over time, comparing schemes with no reversal (black), no Bragg pulse only reversal (red), and both Bragg and reversal (blue). Solid curves are guides to the eye. Dotted lines mark population levels that signify the reversal efficiency of each scheme. Each data point is averaged from 22 repetitions. Error bars denote one standard deviation.

5.4 Many-body echo

We can achieve a much improved reversal performance by swapping the atoms in blue detuned and red detuned modes in the continuum, which effectively inverts the detuning $\Delta_{\mathbf{k}}$, before applying the reversal pulse, see Fig. 5.3a. The swapping is implemented by a Bragg pulse of

two counter-propagating laser beams along the $x-$direction with wavelength $\lambda = 1064\ nm$, which transfer momentum to the atoms through Bragg diffraction. The momentum transfer $k_L = 4\pi/\lambda$ is chosen to be twice the resonance momentum $k_f = \sqrt{2mE_f}/\hbar$ for modulation frequency $f = 2652$ Hz, such that the momentum mode $k = k_f + \delta k$ is coupled to $k = -k_f + \delta k$, see Fig. 5.3b. To leading order, the two modes have equal and opposite detuning. The length and strength of the Bragg pulse is carefully tuned to realize a $\pi-$pulse, which swaps the population in the two coupled modes, while simultaneously realizing a $2\pi-$pulse for the BEC at $k = 0$, such that the disturbance to the BEC is minimal. See supplement for details. After the Bragg pulse, atoms in off-resonant modes are put into modes with equal and opposite detuning, and evolve with inverted detuning during the reversal pulse. We call this method of reversing many-body dynamics in a continuum the 'many-body echo'.

To benchmark the performance of the many-body echo, we measure the time evolution of the population of atoms excited along the $x-$direction, and compare three different schemes, see Fig. 5.3c. In the 'no reversal' scheme, we extend the excitation pulse to continuously drive the system. The population exponentially grows until saturation, when the BEC starts to deplete. In the 'reversal' scheme, after the excitation pulse we apply a reversal pulse that is phase shifted by 180°, which is similar to the scheme in Fig. 5.2. Finally, for the many-body echo scheme, we apply the Bragg pulse after the excitation pulse, followed by a reversal pulse phase shifted by 273.6°. The difference in reversal phase shift is due to the phase imprinted by the Bragg pulse. Starting with a population 469(29) before reversal, without the Bragg pulse the lowest excitation population we achieve is 366(15), a reversal efficiency of 22(6)%. With the Bragg pulse, the many-body echo reverses the excitation population down to 149(7), a reversal efficiency of 68(2)%, see Fig. 5.3d. The factor of 3 improvement in reversal efficiency implies an improvement of the Loschmidt echo by the same factor for each mode. The many-body echo effectively reduces the subsystem entropy of each excited mode by 1.14(6) k_B, compared to the entropy reduction of 0.25(8) k_B with the simple

reversal scheme. Theoretically the reversal efficiency of many-body echo can reach 99%, see supplement. However, the experiment is limited by primarily the depletion of the BEC and the escape of the excited atoms from the BEC, which can be seen from the saturation of growth in the 'no reversal' scheme.

5.5 SU(1,1) interferometer

We can take advantage of the many-body echo to improve the performance of SU(1,1) interferometry, similar to how spin echo is widely adopted to improve $SU(2)$ interferometers. We realize an SU(1,1) interferometer with a contrast of 90% and up to 2000 particles. The particle number we achieve is 100 times higher than state-of-the-art using nonlinear optics and cold atoms, thanks to the many-body and continuum nature of our system. The setup for the SU(1,1) interferometer is largely the same as Fig. 5.3, except that the phase shift of the reversal pulse ϕ is varied by changing its delay time, see Fig. 5.4a. In the language of SU(1,1) interferometry, our system uses the BEC as the pump. The excitation pulse results in a parametric amplifier (PA) that creates two-mode squeezed states in pairs of momentum modes. The Bragg pulse imprints phases on the BEC as well as the excited atoms. The reversal pulse realizes another PA, after which the total excitation population is measured, see Fig. 5.4b. The population displays interference fringes as a function of the phase of the reversal pulse, which provides a measurement of the phase imprinted by the Bragg pulse, see Fig. 5.4c. Note that we stop the reversal pulse after 6 periods, which is when the reversal efficiency is highest.

The phase shift at the minimum of the interference fringes $\phi_{\min}$ measures the phase difference between the excited atoms and the BEC,

$$\phi_{\min} = \theta_k + \theta_{-k} - 2\theta_0 - \pi, \tag{5.3}$$

where θ_0 is the phase shift of the BEC and $\theta_{\pm k}$ are the phase shift of the excited atoms. Fitting a sinusoidal curve to the data yields the measurement $\phi_{\text{min}} = -79(1)^\circ$, which is in good agreement with the prediction -74.2°, see supplement. The maximum measured excitation population is 2000(140) atoms, whereas the minimum is 196(48) atoms, giving a contrast of 90(3)%, see Fig. 5.4d.

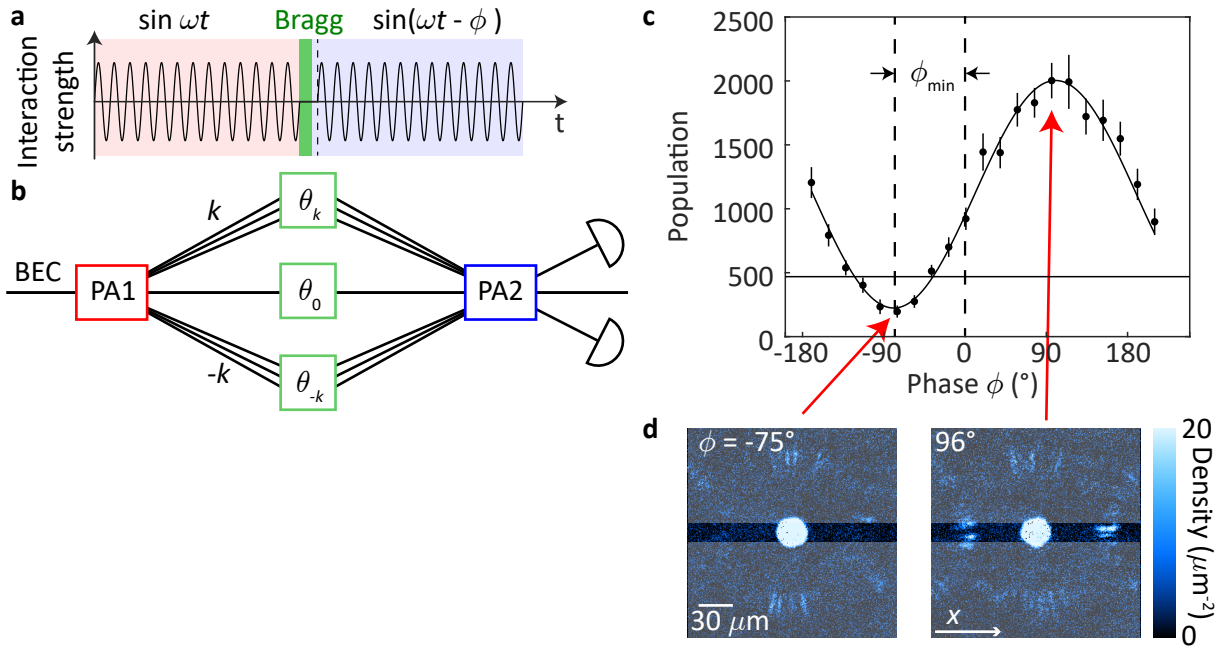

Figure 5.4: **SU(1,1) inteferometry.** **(a)** We apply the same driving scheme as shown in Fig. 5.3, and scan the phase shift ϕ of the reversal pulse. **(b)** We realize a multi-modal SU(1,1) interferometer, where the BEC serves as the pump for the parametric amplifier (PA1) representing the excitation pulse. The Bragg pulse imprints a phase θ_0 on the BEC, and $\theta_{\pm k}$ on the excited atoms. The second parametric amplifier (PA2) represents the reversal pulse. We measure the final total excitation population. **(c)** The final population forms interference fringes as a function of the phase shift ϕ. The phase shift at the minimum is $\phi_{\text{min}} = \theta_k + \theta_{-k} - 2\theta_0 - \pi$, which measures the difference in phase shift between the BEC and excited atoms imprinted by the Bragg pulse. The reversal pulse is stopped after 6 periods, when the reversal efficiency is highest. The black curve is a sinusoidal fit with period fixed at 360°. The horizontal line denotes the population before reversal. Each data point is averaged from 14 repetitions. Error bars denote one standard deviation. **(d)** Example single shot images at destructive and constructive interference show clear distinction in excitation population. The red boxes mark the region of interest.

5.6 Additional information

5.6.1 Bragg pulse with optical lattice

The Bragg pulse is a square pulse of optical lattice formed by retroreflected 1064 nm laser for a duration of 140 μs. The strength of the pulse is calibrated experimentally from the Rabi oscillation. Since the pulse is short and strong, the BEC is excited through off-resonant transitions to higher momentum states. The duration 140 μs is chosen according to numerical simulation, such that the pulse strength that realizes a $\pi-$pulse for atoms at $k = \pm k$ also realizes a $2\pi-$pulse for the BEC at $k = 0$. The simulation suggests that the BEC returns to the initial state with $> 99.9\%$ fidelity. The $k = -k_f$ atoms are transfered to $k = +k_f$ with 93.4% fidelity, with 3.2% each ending up in $k = +3k_f$ and $k = -3k_f$, and 0.05% remaining in $k = -k_f$. Since $k = +3k_f$ and $k = -3k_f$ don't participate in the reversal dynamics and essentially no atom remains in $k = -k_f$, the Bragg $\pi-$pulse can be considered nearly perfect. The simulation describes a single particle starting from a momentum eigenstate that evolves in the presence of an optical lattice. The time trace of population in each Bragg order is shown in Fig. 5.5.

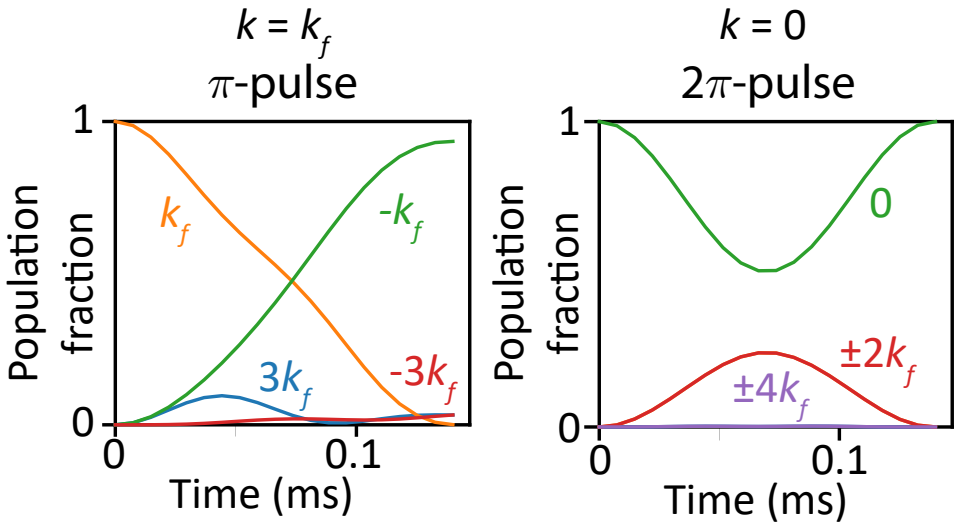

Figure 5.5: Time trace of population fraction in each momentum state during the Bragg pulse, for the excited atoms ($k = k_f$) and the BEC ($k = 0$).

The simulation also predicts the phase shift imprinted onto the BEC and the excited atoms near the band edge. The phase shift on excited atoms should be -90° since they complete a $\pi-$pulse. However, since the system is not 2-level, this phase shift is actually predicted to be -142.1°. The phase shift on the BEC is predicted to be $\theta_0 = 51.8^\circ$.

In the context of the SU(1,1) interferometer, a time delay τ of the reversal pulse realizes a phase shift $\phi = \omega\tau$ in the rotating frame, where $\omega = 2\pi f$, $f = 2652$ Hz. During this time, in the lab frame the resonantly excited atoms acquire a phase $\delta = -\omega\tau/2$, whereas the BEC acquire no phase shift. Maximum excitation is achieved when the BEC and excited atoms have the same phase. At the end of the Bragg pulse, the phase of the BEC is 51.8°, and that of the excited atoms is -142.1°. After another $\Delta\tau = (166.1^\circ/360^\circ) \times (f/2) = 348$ μs, the phase of the excited atoms becomes 51.8°, same as that of the BEC, and this is the time delay that results in maximum excitation. Since the Bragg pulse is $\tau_0 = 140$ μs long, the total time delay is $\tau = 488$ μs, which gives $\phi_{\max} = 465.9^\circ = 105.9^\circ$. The minimum excitation is achieved when the phase is shifted from the maximum by 180°, $\phi_{\min} = -74.1^\circ$.

Another way to derive this result is that during the Bragg pulse, the rotating frame acquires a phase shift of $\tau_0 \times (f/2) \times 360^\circ = -66.8^\circ$, which means that in the rotating frame the Bragg pulse imprints a phase of $\theta_{\pm k} = -75.3^\circ$ on the excited atoms. Given $\theta_0 = 51.8^\circ$, we have $\phi_{\min} = \theta_k + \theta_{-k} - 2\theta_0 + \pi = -75.3^\circ$

5.6.2 Numerical simulation of many-body echo

In the many-body echo scheme, the Bragg pulse couples two pairs of momentum modes, $\pm k_f \pm \delta k$. We number the modes as 1 to 4, with $1 : -k_f - \delta k, 2 : k_f + \delta k, 3 : k_f - \delta k, 4 : -k_f + \delta k$. Then the Hamiltonian during the excitation (H_1), Bragg (H_2) and reversal (H_3) pulses are

$$H_{1,3} = \Delta_1(a_1^\dagger a_1 + a_2^\dagger a_2) + \Delta_3(a_3^\dagger a_3 + a_4^\dagger a_4) + g(a_1^\dagger a_2^\dagger + a_1 a_2 + a_3^\dagger a_4^\dagger + a_3 a_4) \qquad (5.4)$$

$$H_2 = \Delta_1(a_1^\dagger a_1 + a_2^\dagger a_2) + \Delta_3(a_3^\dagger a_3 + a_4^\dagger a_4) + \Omega(a_1^\dagger a_3 + a_3^\dagger a_1 + a_2^\dagger a_4 + a_4^\dagger a_2) \tag{5.5}$$

Here $\Delta_1 = \frac{\hbar^2(2k_f\delta k+\delta k^2)}{2m}$ is the detuning of modes 1 and 2, $\Delta_3 = \frac{\hbar^2(-2k_f\delta k+\delta k^2)}{2m}$ is that of modes 3 and 4, g is the interaction modulation strength and Ω is the Bragg optical lattice strength. The coupling strengths Ω and g are chosen to be real by redefinition of phase reference for the modes. The Hamiltonian is quadratic in the bosonic operators during the entire sequence. Therefore, the Heisenberg equation is linear, and can be solved by matrix algebra. We numerically solve the Heisenberg equations for each quadruplet of modes with a certain δk, and collect the result for all momentum to simulate the entire continuum. An example of simulation result is shown in Fig. 5.6.

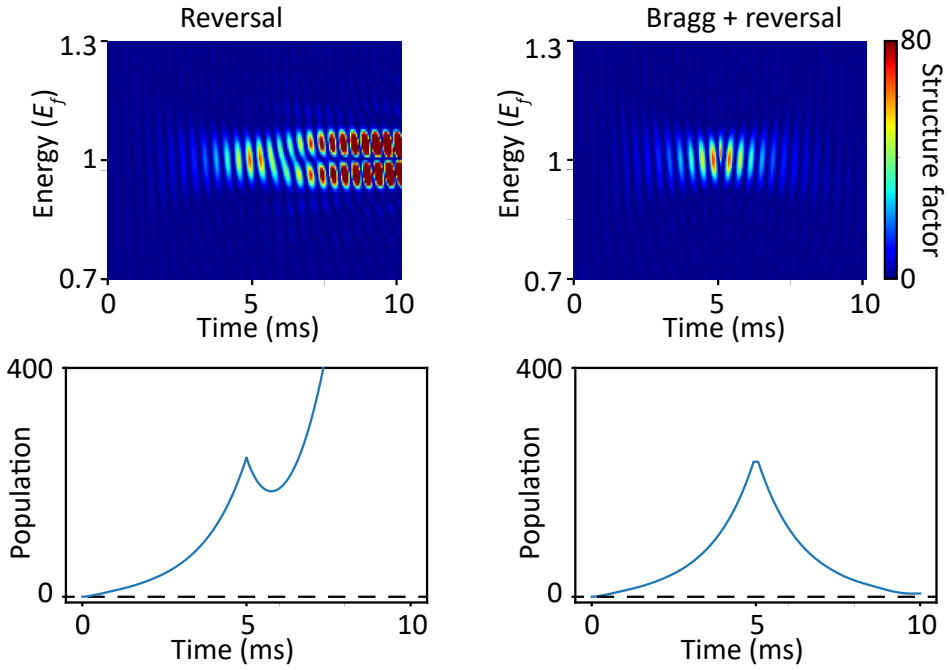

Figure 5.6: Simulation of many-body echo. Top panel shows the evolution of structure factor for different momentum. Bottom panel shows the time trace of the total population. In the simulation we set the modulation frequency at 2652 Hz and modulation strength $g = h \times 70$ Hz. Left side shows the simulation for many-body echo (Bragg and reversal). Right side shows reversal only, for comparison.

5.6.3 SU(1,1) representation and interferometry

The Hamiltonian for one pair of momentum modes $k = \pm k$ is

$$H = \Delta(a_k^\dagger a_k + a_{-k}^\dagger a_{-k}) + g(a_k^\dagger a_{-k}^\dagger + a_k a_{-k}), \tag{5.6}$$

where $\Delta = \frac{\hbar^2 k^2}{2m} - \frac{hf}{2}$ is the detuning, a_k is the annihilation operator for momentum k and g is 1/8 times the peak-to-peak modulation amplitude of chemical potential. Define $K_0 = (a_k^\dagger a_k + a_{-k} a_{-k}^\dagger)/2$, $K_1 = (a_k^\dagger a_{-k}^\dagger + a_k a_{-k})/2$ and $K_2 = (a_k^\dagger a_{-k}^\dagger - a_k a_{-k})/(2i)$. The Hamiltonian is rewritten as

$$H = 2\Delta K_0 + 2gK_1. \tag{5.7}$$

The operators $K_{0,1,2}$ form the $\mathfrak{su}(1,1)$ algebra, defined by the commutation relations

$$\begin{aligned} [K_0, K_1] &= iK_2 \\ [K_2, K_0] &= iK_1 \\ [K_1, K_2] &= -iK_0 \end{aligned} \tag{5.8}$$

Therefore the Hamiltonian H is an element of the $\mathfrak{su}(1,1)$ algebra, the time evolution operator e^{-iHt} is an element of the SU(1,1) group, and the dynamics it generates is a representation of the SU(1,1) group. The Hamiltonian acting on the vacuum generates two-mode squeezed states parametrized by the squeezing parameter z,

$$|z\rangle = \frac{1}{\sqrt{1-z^2}} \sum_n z^n |n, n\rangle. \tag{5.9}$$

The parameter z is a complex number with norm $||z|| < 1$, which can be thought of as a point on the Poincare disk. The Poincare disk is a representation of SU(1,1) [21]. Elements of SU(1,1) acts on the Poincare disk as Mobius transformations written as 2×2 complex

matrices,

$$\begin{pmatrix} a & b \\ c & d \end{pmatrix} : z \to \frac{az+b}{cz+d}. \tag{5.10}$$

The operators $K_{0,1,2}$ are written as

$$K_0 = \frac{1}{2}\begin{bmatrix} 1 & 0 \\ 0 & -1 \end{bmatrix} = \frac{1}{2}\sigma_z, \tag{5.11}$$

$$K_1 = \frac{1}{2}\begin{bmatrix} 0 & 1 \\ -1 & 0 \end{bmatrix} = \frac{i}{2}\sigma_y, \tag{5.12}$$

$$K_2 = \frac{1}{2}\begin{bmatrix} 0 & -i \\ -i & 0 \end{bmatrix} = -\frac{i}{2}\sigma_x, \tag{5.13}$$

where σ denotes Pauli matrices. It can be derived that the time evolution operator $U = e^{-iHt}$ is

$$\begin{aligned} U &= \begin{bmatrix} \cosh\kappa t - \frac{i\Delta}{\kappa}\sinh\kappa t & -\frac{ig}{\kappa}\sinh\kappa t \\ \frac{ig}{\kappa}\sinh\kappa t & \cosh\kappa t + \frac{i\Delta}{\kappa}\sinh\kappa t \end{bmatrix} \\ &= e^{-i\theta K_0} e^{-i\eta K_1} e^{-i\theta K_0} \end{aligned} \tag{5.14}$$

where $\kappa = \sqrt{g^2 - \Delta^2}$, $\theta = \tan^{-1}\left(\frac{\Delta}{\kappa}\tanh\kappa t\right)$ and $\eta = -2\sinh^{-1}\left(\frac{g}{\kappa}\sinh\kappa t\right)$.

In the context of SU(1,1) interferometry, we start from a two-mode squeezed state $|z\rangle = e^{-i\phi K_0} e^{-i\xi K_1} e^{-i\phi K_0}|0\rangle$ with $z = e^{i(\phi-\pi/2)}\tanh\xi/2$. After evolution with U, we end up with $|w\rangle = U|z\rangle$, with

$$w = e^{i\theta}\frac{e^{i\theta}z\cosh\frac{\eta}{2} - i\sinh\frac{\eta}{2}}{ie^{i\theta}z\sinh\frac{\eta}{2} + \cosh\frac{\eta}{2}}. \tag{5.15}$$

The final population is $n_f = |w|^2/(1-|w|^2)$, and can be derived to be

$$n_f = \frac{1}{2}\left(\cosh\xi\cosh\eta - 1\right) + \frac{1}{2}\cos(\theta+\phi)\sinh\xi\sinh\eta. \tag{5.16}$$

It is clear that the final population depends sinusoidally on the phase of the state $|z\rangle$, giving interference fringes. In our experiment, the time delay of the reversal pulse changes the phase of the reversal pulse in the rotating frame. In the lab frame, it instead changes the phase of the excited atom (due to energy difference with the BEC), which is equivalent to changing the phase of the two-mode squeezed state $|z\rangle$.

5.6.4 Visualization of many-body echo dynamics

Inspired by how spin echo can be better understood with the help of visualizing $SU(2)$ on the Bloch sphere, we develop a visualization of the many-body echo dynamics. The governing Hamiltonians are given in Eq. (5.4) and (5.5). The Hamiltonian Eq. (5.4) generates dynamics in SU(1,1), whereas the hamiltonian Eq. (5.5) generates dynamics in $SU(2)$. The $SU(2)$ generators are $S_x = a_1^\dagger a_3 + a_3^\dagger a_1$, $S_y = (a_1^\dagger a_3 - a_3^\dagger a_1)/i$, $S_z = a_1^\dagger a_1 - a_3^\dagger a_3$. Therefore, the many-body echo dynamics is a representation of $SU(1,1)\times SU(2)$. Similar to how $SU(2)$ can be visualized on the Bloch sphere with coordinates given by the expectation value of the generators, we can compute the expectation values of the following generators,

$$\begin{aligned} K_x &= \frac{1}{2}(a_1^\dagger a_2^\dagger + a_1 a_2) \\ K_y &= \frac{1}{2i}(a_1^\dagger a_2^\dagger - a_1 a_2) \\ S_x &= a_1^\dagger a_3 + a_3^\dagger a_1 \end{aligned} \tag{5.17}$$

We have $\langle S_y\rangle = 0$, and the other expectation values can be computed from conservation laws. The vacuum is at the origin with all expectation values being 0.

The expectation values Eq. (5.17) allow us to represent each state as a point in a three

dimensional space. For simplicity we only show the two dimensions spanned by K_x and K_y. At each instant of time, the continuum of modes with different detuning occupy a family of different states. In Fig. 5.7, we plot the state of each mode in the continuum (labeled by color) at several instants of time. As a comparison we also plot the evolution under only reversal without the Bragg pulse, showing how the off resonant modes miss the origin and fail to be reversed.

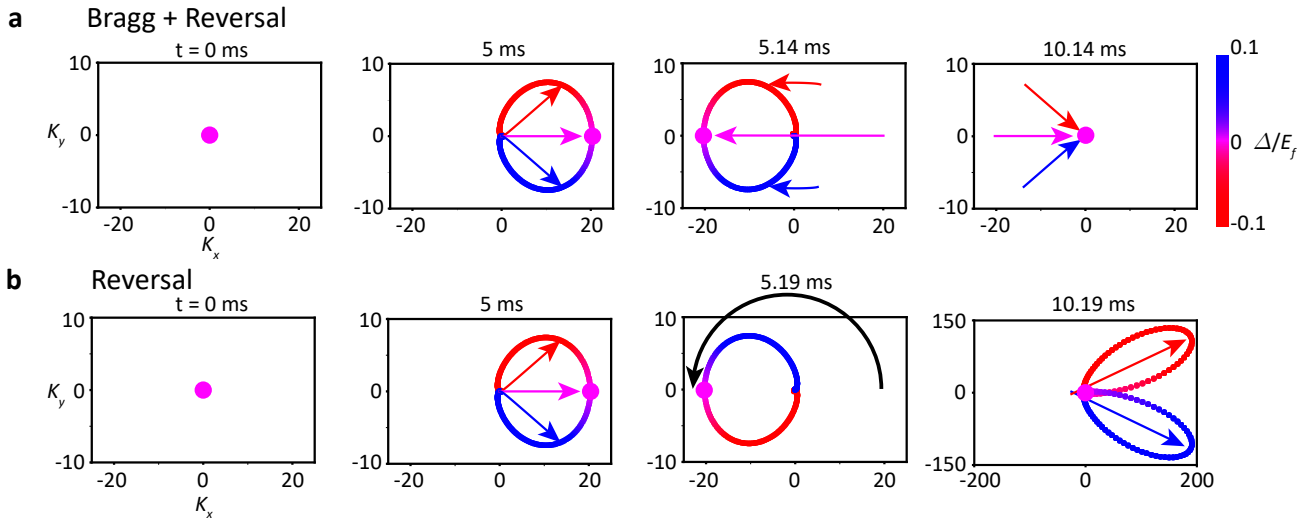

Figure 5.7: Visualization of many-body echo and reversal dynamics. Top: many-body echo dynamics at four different times. $t = 5$ ms is right before Bragg pulse. $t = 5.14$ ms is right after Bragg pulse. $t = 10.14$ ms is when the system is almost completely reversed. Bottom: Reversal dynamics without Bragg pulse. The off-resonant modes do not go back to the origin.

5.6.5 Loschmidt echo

Loschmidt echo is defined as the overlap of the initial and final states after imperfect time reversal. Here we theoretically calculate the Loschmidt echo for our system, described by Hamiltonian Eq. (5.2).

The Hamiltonian produces two-mode squeezed states. The initial state is the vacuum. The overlap with the vacuum $|0\rangle$ of a two-mode squeezed state $|k\rangle$ with mean population n_k is

$$|\langle 0|k\rangle|^2 = \frac{1}{1+n_k}. \tag{5.18}$$

Since the Hamiltonian describes independent pairs of modes, the Loschmidt echo of the entire system is the product

$$L = \prod_k \frac{1}{1+n_k}. \tag{5.19}$$

For a pair of modes with detuning Δ_k, the final population can be calculated to be

$$n_k = \frac{4g^2\Delta_k^2}{(g^2-\Delta_k^2)^2}\sinh^4\sqrt{g^2-\Delta_k^2}t. \tag{5.20}$$

Most modes have $n_k \gg 1$, except those with exponentially small detuning. Therefore, we can approximate the Loschmidt echo as

$$L \propto e^{-\sum_k 4\sqrt{g^2-\Delta_k^2}t} \approx e^{-\alpha M g t}, \tag{5.21}$$

where M is the number of modes and by taking the continuum limit of the sum over k we obtain $\alpha = \pi$.

An example of numerical calculation of time decay of Loschmidt echo is shown in Fig. 5.8 for the scenarios with no reversal, simple reversal and many-body echo. Exponential decay can be seen in all three scenarios.

5.6.6 Detection

The structure factor $S_{\mathbf{k}} = N^{-1}\int d\mathbf{r}_1 d\mathbf{r}_2 e^{-i\mathbf{k}(\mathbf{r}_1-\mathbf{r}_2)} n(\mathbf{r}_1)n(\mathbf{r}_2) = \langle (a_{\mathbf{k}} + a^\dagger_{-\mathbf{k}})(a_{-\mathbf{k}} + a^\dagger_{\mathbf{k}})\rangle$ measures the quadrature of mode $\mathbf{k}$, and is experimentally detected by Fourier transforming the atomic density. However, our limited imaging resolution results in a distortion of the measured density profile from the actual one. In particular, density modulations at different wave vectors are attenuated and phase shifted, according to the modulation transfer function

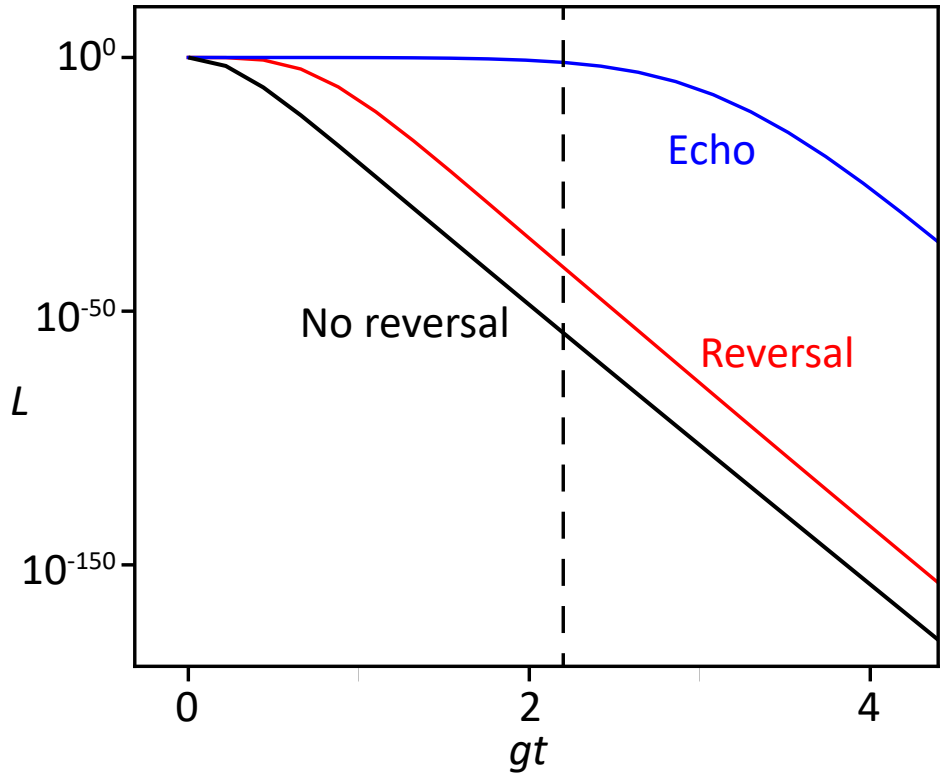

Figure 5.8: Numerical calculation of time decay of Loschmidt echo, for no reversal (black), reversal (red) and many-body echo (blue) schemes. Vertical dashed line denotes the parameters roughly corresponding to our experimental conditions.

[10]. More over, since our condensate has high optical density, the imaging suffers from additional saturation. To calibrate for all these distortions, we measure the structure factor for a ground state condensate in the same trap, with low chemical potential. In this case the structure factor is predicted to be 1 for all wave vectors except very close to $\mathbf{k} = 0$. This experimentally measured structure factor is smoothed using the MATLAB function `denoiseImage`, and used as the baseline. The experimental data shown in Fig. 5.2c is the measured structure factor divided by this baseline. Additionally, since the structure factor is 2D, we bin each momentum mode according to their kinetic energy, and plot the average of the structure factor in each bin. Even though the data is from only 2 experimental repetitions, each repetition gives a 2D grid of structure factors and each energy bin contains many data points.

For Fig. 5.3 and 5.4, we wait 28 ms until the excited atoms fly out of the condensate and form jets. When counting the excitation population, we only count the excitation along the $x-$direction, in the red boxes shown in Fig. 5.9.

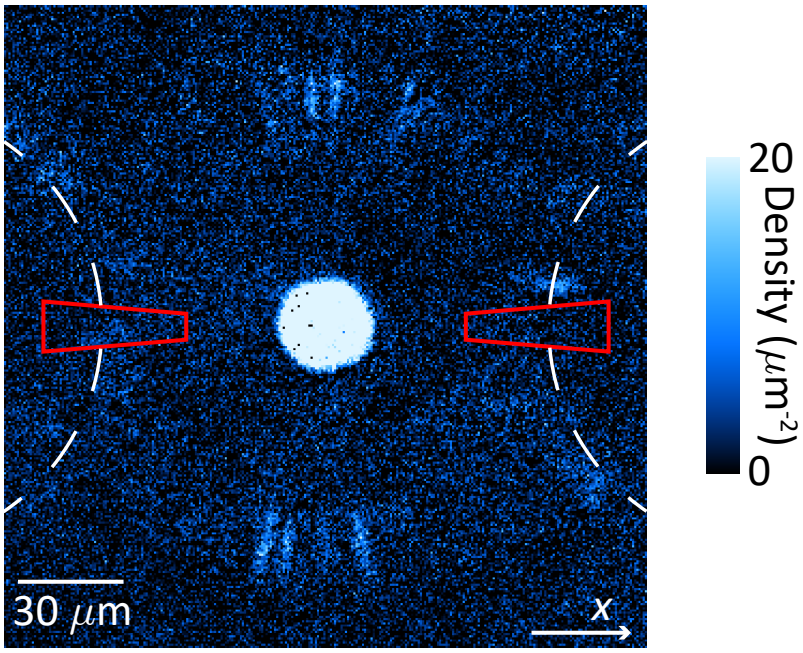

Figure 5.9: Red boxes mark the region of interest in which we count the excitation population. White dashed circles indicate the circular jet emissions diffracted by the Bragg pulse.

5.6.7 Experimental parameters

For the experiments shown in Fig. 5.2, the particle number is 4.5×10^4, the trap radius is 22 μm, the time averaged scattering length is 6 a_B, the peak-to-peak modulation amplitude of scattering length is 80 a_B, and the modulation frequency is 500 Hz. For the experiments shown in Fig. 5.3 and 5.4, the particle number is 3×10^4, the trap radius is 15 μm, the time

averaged scattering length is 1 a_B, the peak-to-peak modulation amplitude of scattering length is 50 a_B, and the modulation frequency is 2652 Hz.

5.6.8 Experimental calibration of Bragg pulse

In the experiment, the Bragg pulse is calibrated by first setting the pulse length to 140 μs, then scanning the light intensity to realize a $2\pi-$pulse on the BEC. There will be multiple maxima due to Rabi oscillation, and we find the one with the weakest light intensity. We then fix the pulse intensity and scan the pulse length to confirm that the jets experience a $\pi-$pulse.

Since the theory calculation assumes a square pulse, we want to make sure the rise time of the light intensity is minimal. An oscilloscope trace of the photodiode signal recording the retroreflected beam intensity is shown in Fig. 5.10. We can see that the rise time is rather short (~ 5 μs), and that the pulse length is 140 μs.

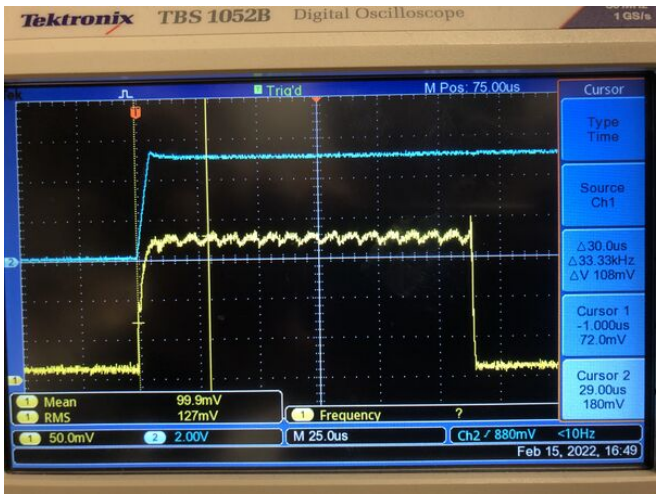

Figure 5.10: Pulse shape of the Bragg pulse.

We apply the Bragg pulse to a ground state BEC, fixing the pulse length and scanning the beam intensity, and measure the population in different Bragg diffraction orders. The Bragg orders are separated spatially by a short time-of-flight. Fig. 5.11 shows the dependence of the population in each Bragg order on the beam intensity, determined by the control voltage

to the retroreflection AOM. Several oscillations can be seen. The $2\pi-$pulse is realized at AOM control voltage 1.35V, as can be seen in Fig. 5.12.

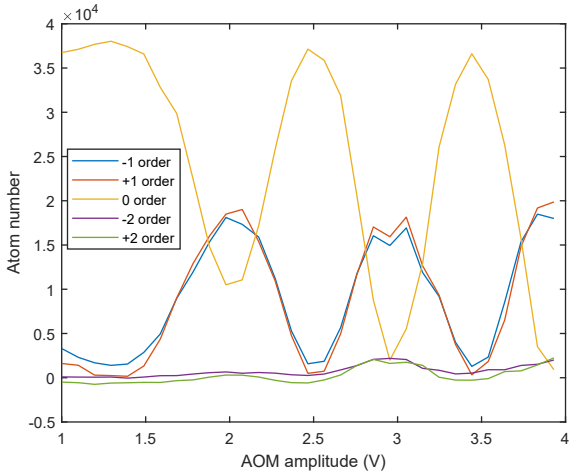

Figure 5.11: Bragg diffraction of the BEC at various beam intensities.

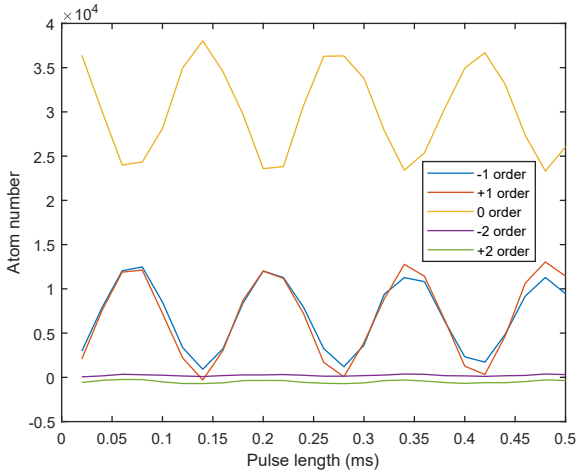

Figure 5.12: Rabi oscillation of the BEC under Bragg pulse with AOM control voltage 1.35V. The population in the 0-th Bragg order first returns to maximum at 140 μs.

The Bragg diffracted jets are actually spatially displaced from the un-diffracted jets after time-of-flight, because of their motion before the Bragg pulse. Left moving jets first fly to the left by some distance before being Bragg diffracted to the right, where as the un-diffracted

jets on the right side spend the entire time moving to the right. By delaying the Bragg pulse, we can exaggerate this displacement, see Fig. 5.13, allowing us to measure the diffracted and un-diffracted population separately. We can thus measure the Rabi oscillation and confirm the realization of a $\pi-$pulse, see Fig. 5.14.

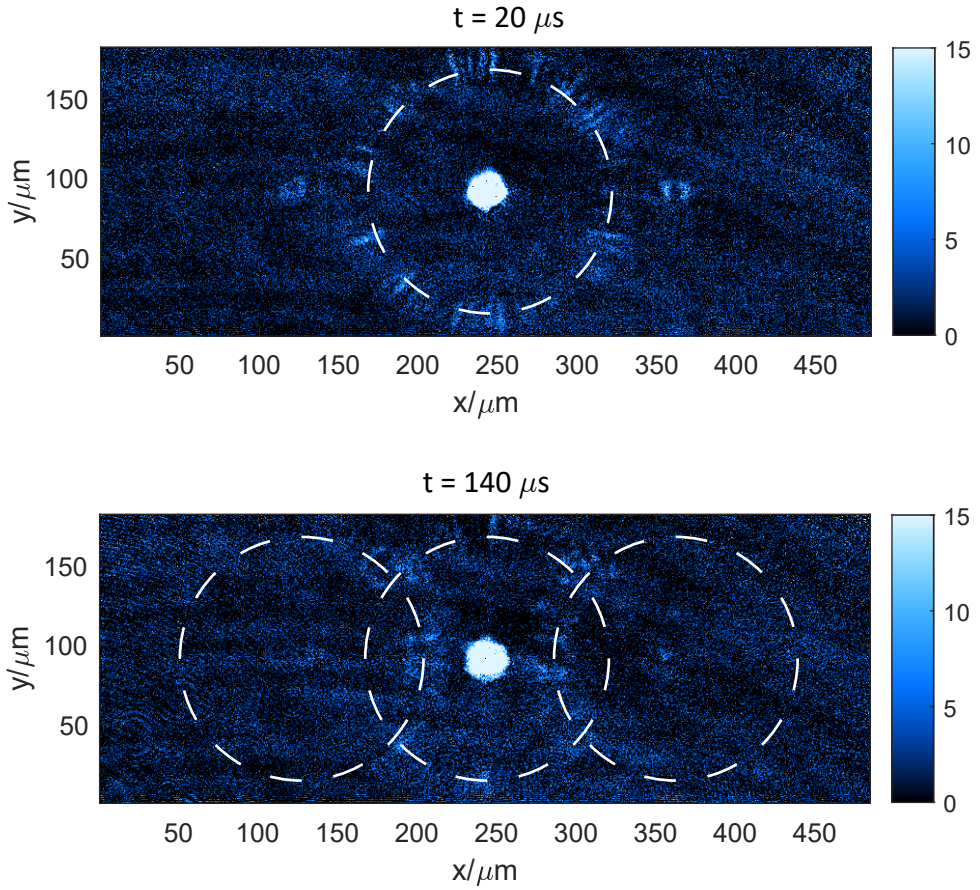

Figure 5.13: Spatial separation of Bragg diffracted jets. Colorbar shows atomic density in units of μm^{-2}.

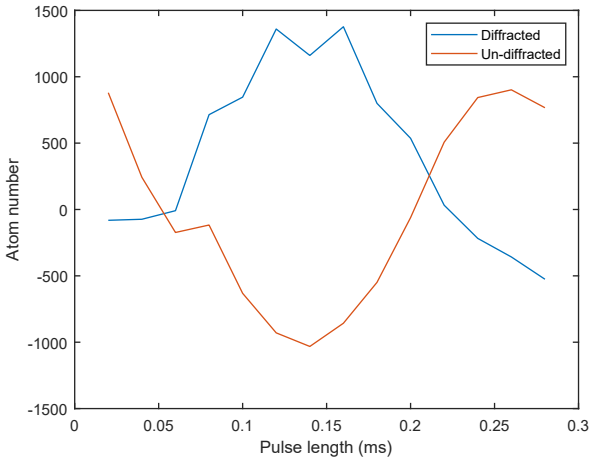

Figure 5.14: Rabi oscillation of jets under the Bragg pulse. Imaging background is not carefully calibrated, but the un-diffracted population clearly reaches minimum at 140 μs.

CHAPTER 6

OTHER PROJECTS

Over my years in Chin lab I have contributed to a few other projects. In this chapter I will present the technical details of my contributions in those projects, as well as some preliminary theoretical and numerical explorations of new proposals.

6.1 Superresolution microscopy of cold atoms in an optical lattice

Superresolution microscopy has revolutionized the fields of chemistry and biology by resolving features at the molecular level. In atomic physics, such a scheme can be applied to resolve the atomic density distribution beyond the diffraction limit and to perform quantum control. In this work we demonstrate superresolution imaging based on the nonlinear response of atoms to an optical pumping pulse. With this technique, the atomic density distribution can be imaged with a full-width-at-half-maximum resolution of 32(4) nm and a localization precision below 500 pm. The short optical pumping pulse of 1.4 μs enables us to resolve fast atomic dynamics within a single lattice site. A by-product of our scheme is the emergence of Moiré patterns on the atomic cloud, which we show to be immensely magnified images of the atomic density in the lattice.

The experimental details and main results can be found in our publication [66]. In this section I will present the derivations of some key theoretical formulas in the paper.

6.1.1 General setup

In our experiment, the Cesium atoms normally occupy the internal state $|F = 3\rangle$, which is the lowest magnetic state. Before we perform absorption imaging, we use optical pumping to transfer the atoms to the state $|F = 4\rangle$, after which the atoms can absorp the imaging light and cast a shadow on the camera. If the atoms remain in the state $|F = 3\rangle$, it is invisible

to the imaging. Constrained by the optical resolution $r \sim 1$ μm of our microscope, we can only measure the total number of atoms within each circle of radius r, but not resolve the finer distribution of atoms.

The main idea of our technique is as follows. Instead of optical pumping all the atoms, we form a standing wave with the optical pumping light by retroreflecting the beam. The standing wave is tuned carefully such that the light intensity at the nodes is precisely canceled. In this case, only atoms away from the nodes are optically pumped to $|F = 4\rangle$, while the atoms close to the nodes see very little optical pumping light and remain in $|F = 3\rangle$, which is a dark state to the imaging light. The population of atoms close to the nodes can then be measured as the deficit in the detected atom number. By scanning the position of the nodes across the atomic sample and repeating the imaging, we can map out the atomic distribution with a precision not constrained by the microscope resolution, but rather the width of the dark window around the nodes.

In the following sections I present the derivation of the shape and width of the dark window, as well as the fact that our detected signal gives the shape of the atomic distribution broadened by the dark window, which serves as a point spread function.

6.1.2 Three-state optical pumping model

Since we excite the atom using an optical pumping beam forming a standing wave (optical lattice), only atoms near the nodes of the standing wave remain unexcited in the dark state. The dark fraction as a function of the distance to the nodes is a 'window function' that we scan across the probed sample, and the width of the window function determines the spatial resolution of our imaging technique. Here quantitatively describe the optical pumping process, and derive the dark fraction of the atoms. We also derive the FWHM of the window function:

We consider the states $F = 3, 4, 4'$. Spontaneous emission of $F' = 4$ state does not always

result in state $F = 4$, but also state $F = 3$. The branching ratio for the desired decay into $F = 4$ is $\beta = 7/12$. In addition, we always operate in the regime where the pulse duration is much longer than the natural lifetime $1/\Gamma$ of the $F' = 4$ state, such that Rabi oscillations can be neglected. Therefore we employ a three state rate equation model:

$$\begin{aligned} \dot{p_{4'}} &= -\frac{s\Gamma}{2}(p_{4'} - p_3) - \Gamma p_{4'} \\ \dot{p_3} &= -\frac{s\Gamma}{2}(p_3 - p_{4'}) + (1-\beta)\Gamma p_{4'} \\ \dot{p_4} &= \beta\Gamma p_{4'} \\ f &= p_4, \end{aligned} \tag{6.1}$$

where p denote occupation probabilities for different internal states, the excitation fraction f is equal to the probability p_4 of the atom to be in $F = 4$ state, and $s = 2\Omega^2/\Gamma^2 = I/I_{\text{sat}}$ is the intensity in units of saturation intensity.

Such a first order linear differential equation can be easily solved by matrix diagonalization. The solution of f at pulse time t and intensity s corresponding to drive field Ω is found to be:

$$\begin{aligned} f &= 1 - \frac{\gamma_+}{\gamma_+ - \gamma_-}e^{-\gamma_- t} - \frac{\gamma_-}{\gamma_- - \gamma_+}e^{-\gamma_+ t} \\ \gamma_\pm &= \frac{\Gamma}{2}(s+1)\left(1 \pm \sqrt{1 - 2s\beta/(s+1)^2}\right). \end{aligned} \tag{6.2}$$

The optical pumping lattice formed by retro-reflecting a beam with intensity I gives rise to a drive field described by:

$$\Omega(x) = \sqrt{2s_0\Gamma^2}\sin(2\pi x/\lambda_{\text{op}}), \tag{6.3}$$

where $s_0 = I/I_{\text{sat}}$ and $\lambda_{\text{op}} = 852.335$ nm is the wavelength of the optical pumping light. In

the limit of long pulse time $t \gg 1/\Gamma$ where we operate, we can consider only the case with $s \ll 1$, as elsewhere $f \approx 1$. In this case,

$$f = 1 - e^{-\frac{\beta\Gamma}{2}\frac{s}{s+1}t}, \tag{6.4}$$

where $s = 2\Omega^2/\Gamma^2 = 4s_0 \sin^2(2\pi x/\lambda_{\text{op}})$. Therefore

$$g = e^{-\frac{\beta\Gamma}{2}\frac{s}{s+1}t}. \tag{6.5}$$

The full width at half maximum w of $g(x)$ is given by equation $g(w/2) = g(0)/2$. In the regime of super-resolution where $w \ll \lambda_{\text{op}}$, the solution is

$$w = \frac{\lambda_{\text{op}}}{2\pi}\sqrt{\frac{2\ln 2}{s_0 t\beta\Gamma}}. \tag{6.6}$$

This describes the predicted resolving power and its scaling with pumping power and pulse time in the strong pulse, long time limit.

The theoretical resolution shown in Fig. 2C in the main text is obtained differently, without making analytical approximations. Instead, the shown prediction is the FWHM of a numerically fitted Gaussian to the shape $f(x)$, the same way FWHM is extracted from experimental data.

6.1.3 Optical pumping under spatially dependent drive field

Here we derive the equation that states that the excitation fraction under a spatially dependent drive field is given by a convolution, just like how an image is the convolution of the ground truth with the point spread function.

$$1 - \mathcal{F}(\Delta x) = \int n(x) g\left(\Delta x - x\right) dx, \tag{6.7}$$

where $n(x)$ is the density distribution of the imaged atoms, $\mathcal{F}(\Delta x)$ is the fraction of atoms excited as a function of the optical pumping lattice displacement Δx, which is the imaging signal that we measure, and $g(x)$ is the window function Eq. (6.5). The derivation is given assuming a pure initial state for the atom. Generalization to mixed states is straight forward.

The atom has spatial and electronic degrees of freedom. Therefore, a state can be written as

$$|\psi\rangle = \sum_{i,j} \psi_{i,j} |i\rangle_x \otimes |j\rangle_e, \tag{6.8}$$

where $|i\rangle_x$ and $|j\rangle_e$ form a basis in the spatial and electronic subspace, respectively, and $\psi_{i,j}$ are the probability amplitudes.

A density matrix $\hat{\rho}$ can be written similarly:

$$\begin{aligned} \hat{\rho} &= \sum_{i_1,i_2,j_1,j_2} \rho_{i_1,i_2,j_1,j_2} |i_1\rangle_x \langle i_2|_x \otimes |j_1\rangle_e \langle j_2|_e \\ &= \sum_{\alpha,\beta} \rho_{\alpha,\beta} \hat{\alpha}_x \otimes \hat{\beta}_e. \end{aligned} \tag{6.9}$$

Here each $\hat{\alpha}_x = |i_1\rangle_x \langle i_2|_x$ for some i_1, i_2, and notates a basis for the density matrix in the spatial subspace. Similarly $\hat{\beta}_e$ denotes a basis in the electronic subspace.

Optical pumping is described by a linear first order differential equation for the density matrix $\hat{\rho}$, in the form

$$i\partial_t \hat{\rho} = \mathcal{L}\hat{\rho}, \tag{6.10}$$

where $\mathcal{L}$ is a linear operator on $\hat{\rho}$. This linear equation can be solved by matrix exponentiation:

$$\rho(t) = e^{-i\mathcal{L}t}\hat{\rho}(0) = U(t)\hat{\rho}(0), \tag{6.11}$$

where the evolution operator $U(t) = e^{-i\mathcal{L}t}$ is the matrix exponentiation of $\mathcal{L}$.

Given the basis of $\hat{\rho}$, we can expand the linear operator U:

$$\begin{aligned} U &= \sum_{\alpha_1,\alpha_2,\beta_1,\beta_2} A_{\alpha_1,\alpha_2,\beta_1,\beta_2} (\hat{\alpha}_{1,x}\hat{\alpha}_{2,x}) \otimes (\hat{\beta}_{1,e}\hat{\beta}_{2,e}) \\ &= \sum_{u,v} A_{u,v} \hat{u}_x \otimes \hat{v}_e. \end{aligned} \tag{6.12}$$

Here $\hat{u}_x$ and $\hat{v}_e$ again denote basis in the spatial and electronic subspace.

The excitation fraction is the probability of the atom to be found in a 'pumped' state $|p\rangle$ in the electronic subspace, and is given by

$$\mathcal{F} = \mathrm{Tr}(\hat{P}\hat{\rho}), \tag{6.13}$$

where $\hat{P} = |p\rangle\langle p|$ is the projection operator onto $|p\rangle$. Therefore the excitation fraction after evolution U from a initial pure state $\hat{\rho}_0 = \hat{\rho}_{x,0} \otimes \hat{\rho}_{e,0}$ is

$$\begin{aligned} \mathcal{F} &= \mathrm{Tr}(\hat{P}U\hat{\rho}_0) \\ &= \mathrm{Tr}(\sum_{u,v} A_{u,v}\hat{u}_x\hat{\rho}_{x,0} \otimes \hat{P}\hat{v}_e\rho_{e,0}) \\ &= \sum_{u,v} A_{u,v}\mathrm{Tr}(\hat{u}_x\hat{\rho}_{x,0})\mathrm{Tr}(\hat{P}\hat{v}_e\rho_{e,0}) \\ &= \mathrm{Tr}\left(\left[\sum_{u,v} A_{u,v}\mathrm{Tr}(\hat{P}\hat{v}_e\rho_{e,0})\hat{u}_x\right]\rho_{x,0}\right) \\ &= \mathrm{Tr}\left(f\rho_{x,0}\right), \end{aligned} \tag{6.14}$$

where we denote $f = \sum_{u,v} A_{u,v}\mathrm{Tr}(\hat{P}\hat{v}_e\rho_{e,0})\hat{u}_x$. This f is in fact the excitation fraction of atoms in a uniform drive field, as in that case spatial degree of freedom is decoupled and $\mathcal{F} = \mathrm{Tr}\left(f\rho_{x,0}\right) = f$. Noting that the action of f on $\rho_{x,0}$ is direct multiplication, we have

$$\mathcal{F}(\Delta x) = \int n(x) f(\Delta x - x) dx, \tag{6.15}$$

where $n(x)$ is the diagonal of $\rho_{x,0}$ and is the initial spatial distribution, and $f(\Delta x - x)$ is the local excitation fraction due to an optical pumping lattice displaced by Δx. As the remaining fraction $g \equiv 1 - f$ and $\int n(x)dx = 1$, we derive Eq. 1 in the main text.

$$\begin{aligned} 1 - \mathcal{F}(\Delta x) &= 1 - \int n(x) \left[1 - g(\Delta x - x)\right] dx \\ &= \int n(x) g(\Delta x - x) dx. \end{aligned} \tag{6.16}$$

6.1.4 Numerical simulation of motional dynamics

In this work we probe the dynamics of the atomic wavefunction in an optical lattice after a sudden shift of the lattice displacement, as a demonstration of the ability to spatial-temporally resolve nanometer-microsecond scale dynamics of our technique. The numerical prediction of the dynamics which we compare the experimental measurement against is described here.

Dynamics of a single particle in a sinusoidal optical lattice is given by the Schroedinger equation:

$$i\hbar\partial_t \psi = -\frac{\hbar^2}{2m}\partial_x^2 \psi - V_0 \cos(4\pi x/\lambda)\psi. \tag{6.17}$$

Given an initial condition ψ_0, this equation can be numerically solved by Fourier transform followed by matrix exponentiation, or projecting onto the basis of Mathieu functions, which are eigenstates of the Hamiltonian. We simulated the dynamics in a lattice with trap frequency 24 kHz, of an initial state that is the ground band Wannier function localized in one lattice site which is then shifted by 79 nm. The resulting $|\psi(\tau)|^2$ is plotted against τ in the left part of Fig. S2. Comparing with measured data in Fig. 3B, shown in the right

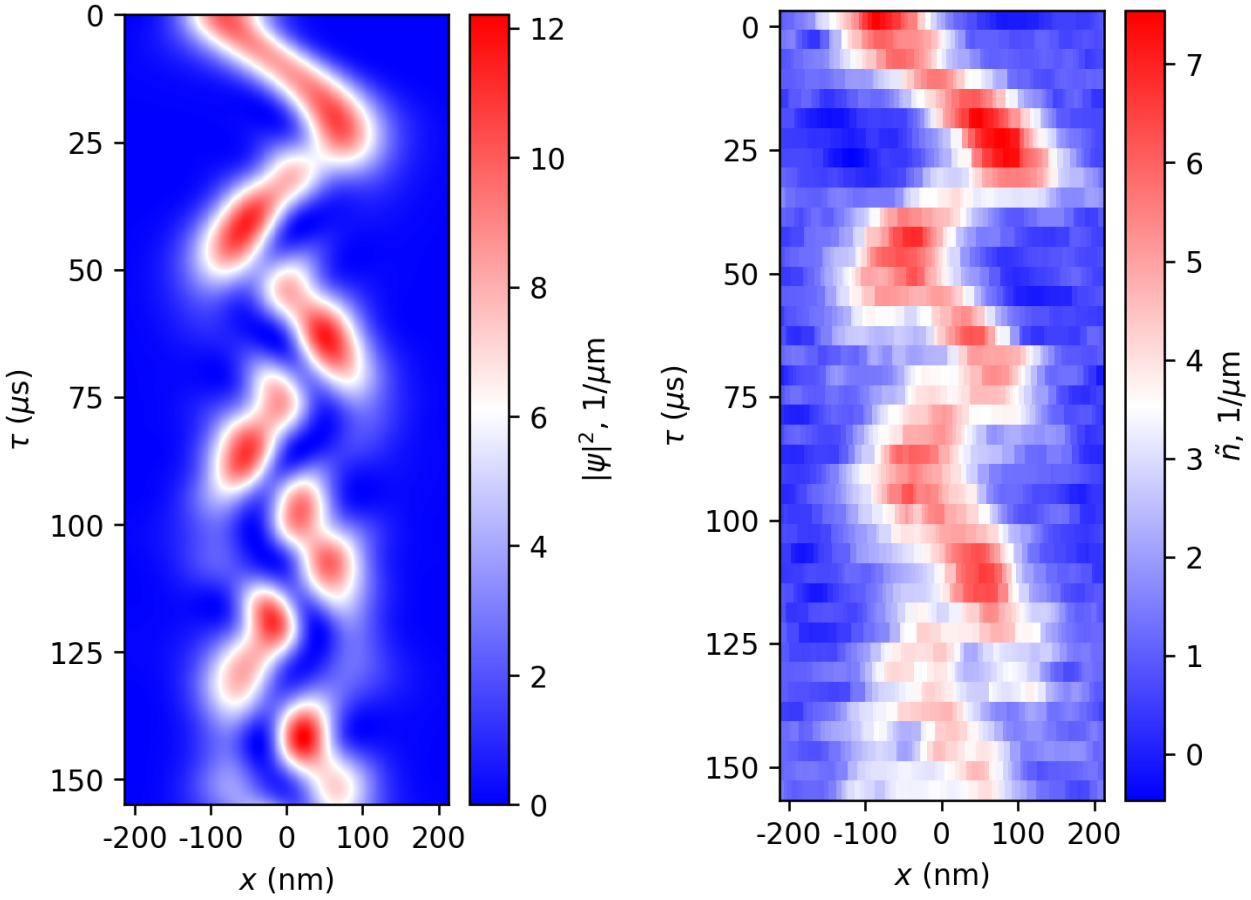

Figure 6.1: Dynamics of an atom in a lattice site. Left: numerical simulation. Right: experimental data.

part, simulation results reflect various features observed experimentally, including the non-sinusoidal motion of the peak, and the distortion of the wavefunction at later times. The simulation showed negligible tunneling to adjacent sites at 160 μs. Inhomogeneity of the traps along imaging direction is not included in simulation, and its contribution to damping of the observed dynamics cannot be reflected by the simulation.

6.2 Pattern formation in a driven Bose–Einstein condensate

Pattern formation is ubiquitous in nature at all scales, from morphogenesis and cloud formation to galaxy filamentation. How patterns emerge in a homogeneous system is a fundamental question across interdisciplinary research including hydrodynamics, condensed matter physics, nonlinear optics, cosmology and bio-chemistry. Paradigmatic examples, such as Rayleigh–Bénard convection rolls and Faraday waves, have been studied extensively and found numerous applications. How such knowledge applies to quantum systems and whether the patterns in a quantum system can be controlled remain intriguing questions. In this project we show that the density patterns with two- (D2), four- (D4) and six-fold (D6) symmetries can emerge in Bose–Einstein condensates on demand when the atomic interactions are modulated at multiple frequencies. The D6 pattern, in particular, arises from a resonant wave-mixing process that establishes phase coherence of the excitations that respect the symmetry. Our experiments explore a novel class of non-equilibrium phenomena in quantum gases, as well as a new route to prepare quantum states with desired correlations.

The experimental details and main results can be found in our publication [12]. In this section I will present the details of symmetry decomposition of density wave patterns.

6.2.1 Symmetry decomposition of density wave patterns

When driven with different modulation waveforms, the BEC develops different patterns. We would like to extract the relative strengths of D_2, D_4 and D_6 symmetry components

in the patterns. We use the following symmetry decomposition method. Given a pattern P, we consider it as a superposition of D_2, D_4 and D_6 symmetric components $P_{2,4,6}$ with amplitudes $c_{2,4,6}$ and a small offset c_0. In order to find the contribution of each symmetry component, we fit the patterns using the following function:

$$P = c_2 P_2 + c_4 P_4 + c_6 P_6 + c_0, \tag{6.18}$$

where

$$P_2 = \mathcal{R}_{\theta_2} \cos(k_f x + \phi_2), \tag{6.19}$$

$$P_4 = \frac{1}{\sqrt{2}} \mathcal{R}_{\theta_4} \left[\cos(k_f x + \phi_{4,1}) + \cos(k_f y + \phi_{4,2}) \right], \tag{6.20}$$

$$\begin{aligned} P_6 = \frac{1}{\sqrt{3}} \mathcal{R}_{\theta_6} \Bigg[& \cos(k_f x + \phi_{6,1}) \\ & + \cos(-\frac{1}{2} k_f x + \frac{\sqrt{3}}{2} k_f y - \frac{1}{2} \phi_{6,1} + \frac{\sqrt{3}}{2} \phi_{6,2}) \\ & + \cos(-\frac{1}{2} k_f x - \frac{\sqrt{3}}{2} k_f y - \frac{1}{2} \phi_{6,1} - \frac{\sqrt{3}}{2} \phi_{6,2}) \Bigg]. \end{aligned} \tag{6.21}$$

Here $\mathcal{R}_\theta[\cdot]$ denotes rotation by angle θ. The basis functions $P_{2,4,6}$ are l^2 normalized such that the strength coefficients $c_{2,4,6}$ are comparable. There are 12 fitting parameters in total: $\{c_2, c_4, c_6\}$ determine the strengths of the symmetry components, c_0 determines the overall offset, $\{\theta_2, \theta_4, \theta_6\}$ determine the orientations, and $\{\phi_2, \phi_{4,1}, \phi_{4,2}, \phi_{6,1}, \phi_{6,2}\}$ determine the displacements. The fitting parameters are initialized randomly and the optimization result with the lowest mean squared error is chosen as the final fit. The optimal fitting parameters are shown in Table 6.1. Decomposition of an example pattern is shown in Fig. 6.2, showing the original pattern, the decomposition into different symmetry components, and the residual.

Parameters	units	Scheme I	Scheme II	Scheme III
c_2	μm^{-2}	0.302(8)	-1.49(4)	-0.32(1)
c_4	μm^{-2}	-0.080(8)	-0.41(3)	-0.26(1)
c_6	μm^{-2}	0.070(6)	1.55(4)	0.072(8)
c_0	μm^{-2}	-0.009(3)	0.02(2)	0.005(4)
θ_2	rad	1.594(2)	-0.497(2)	0.274(2)
θ_4	rad	1.537(6)	-0.608(6)	0.206(2)
θ_6	rad	1.455(6)	-0.547(1)	0.008(7)
ϕ_2	rad	0.96(3)	5.96(3)	4.93(3)
$\phi_{4,1}$	rad	4.4(2)	6.2(1)	-1.72(5)
$\phi_{4,2}$	rad	5.6(1)	2.5(1)	3.84(4)
$\phi_{6,1}$	rad	1.2(1)	3.43(4)	2.6(2)
$\phi_{6,2}$	rad	2.7(1)	5.64(3)	3.8(2)

Table 6.1: Optimal fitting parameters for symmetry decomposition.

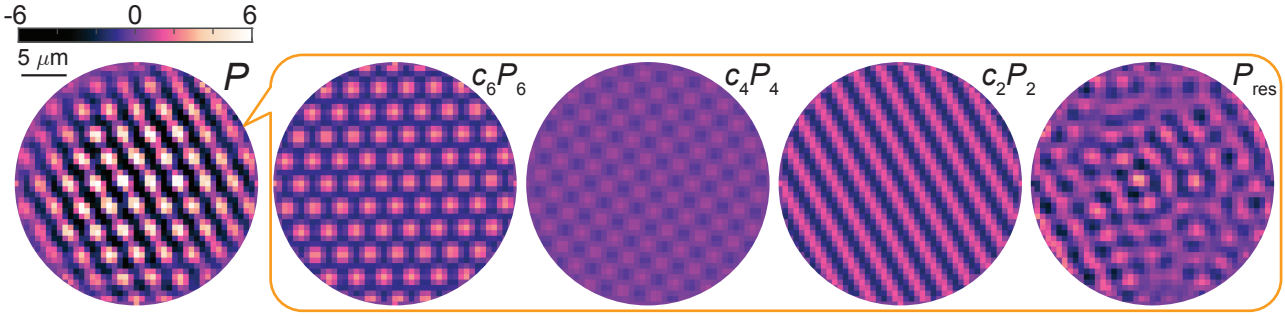

Figure 6.2: **Symmetry decomposition of density wave patterns.** The pattern $P = c_6P_6 + c_4P_4 + c_2P_2 + P_{res}$ is projected onto the bases P_6, P_4 and P_2 with weights c_6, c_4 and c_2. The residual P_{res} is dominated by the spatial inhomogeneity of the sample.

6.3 Artificial magnetic flux from modulated DMD potential

Projection of arbitrary time-dependent potential pattern with DMDs allows great flexibility in engineering the Hamiltonian of the system. One interesting application is creating artificial gauge fields. Creating artificial gauge fields with non-trivial magnetic flux has been experimentally challenging, with existing realizations either relying on external tilts or Raman transitions, both methods introducing significant heating. Here we investigate the possibility to create artificial flux on a square 2D lattice by adding periodic energy modulation to each site. Experimentally this corresponds to a scenario where an additional light

pattern is projected with DMD onto a lattice. The scheme in principle drives off-resonantly, which hopefully results in less heating.

6.3.1 Framework

We first consider four sites of the lattice, with bare tunneling J_0 and on site energy modulation $vf_n(t)$, where v has the unit of energy and $f(t)$ is dimensionless, and $f(t+T) = f(t)$. The tight binding Hamiltonian is

$$H = -\sum_{<nm>} J_0 a_n^\dagger a_m + v\sum f_n(t) a_n^\dagger a_n. \tag{6.22}$$

Define gauge transformation $U = e^{\sum iv\chi_n(t)a_n^\dagger a_n}$ where $\chi_n(t) = -\int^t f_n(\tau)d\tau$. The transformed Hamiltonian is

$$H' = U^\dagger H U - iU^\dagger \partial_t U = -\sum_{<nm>} J_0 e^{iv[\chi_m(t)-\chi_n(t)]} a_n^\dagger a_m. \tag{6.23}$$

If the modulation is far detuned (the driving frequency is much larger than the band width J_0), the effective Hamiltonian is the zeroth order Floquet Hamiltonian:

$$H_{eff} = \langle H' \rangle_T = -\sum_{<nm>} \tilde{J}_{nm} a_n^\dagger a_m, \tag{6.24}$$

with effective tunneling $\tilde{J}_{nm} = J_0 \langle e^{iv[\chi_m(t)-\chi_n(t)]} \rangle_T$, where $\langle\cdot\rangle_T$ denotes average over one period.

6.3.2 'Translationally invariant' modulation

It is natural to consider 'translationally invariant' modulation, where the modulation waveform is the same on all sites, while the phase differs from site to site. If the phase varies linearly through space the modulation corresponds to a traveling wave. Instead we will

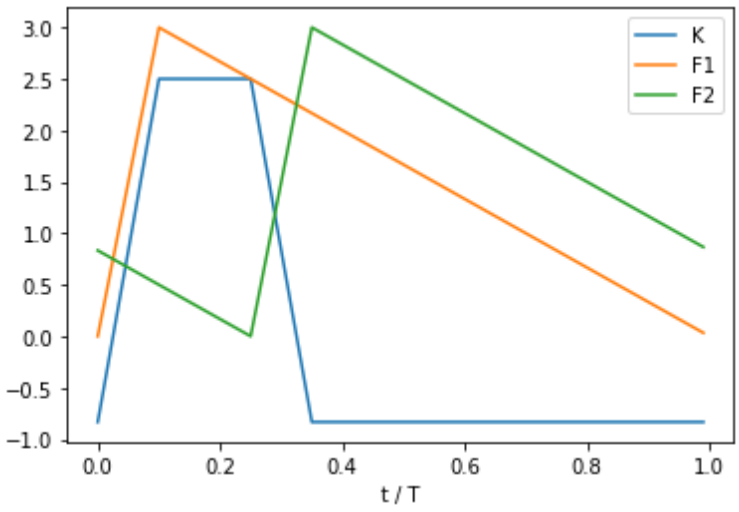

Figure 6.3: Time dependence of K,F_1 and F_2 for realizing a complex effective tunneling

consider general spatial phase dependence:

$$f_n(t) = f(t + \phi_n). \tag{6.25}$$

In this case

$$\chi_m(t) - \chi_n(t) = \int_{t+\phi_m}^{t+\phi_n} f(\tau)d\tau = T\left[F(t + \phi_n) - F(t + \phi_m)\right], \tag{6.26}$$

where $F(t) = \frac{1}{T}\int^t f(\tau)d\tau$ is the dimensionless integral of $f(t)$. We can add a constant offset to $f(t)$ such that $F(t) = F(t + T)$, which corresponds to shifting the energy of all sites by a constant amount, without affecting the physics.

The effective tunneling is thus given by

$$\tilde{J}_{nm}/J_0 = \langle e^{i\nu T[F(t+\phi_n)-F(t+\phi_m)]}\rangle_T = \langle e^{i\alpha K_{nm}(t)}\rangle_T, \tag{6.27}$$

where we define $K_{nm}(t) = F(t)-F(t+\phi_m-\phi_n)$ and $\alpha = vT$ is the dimensionless modulation strength. Obviously $\langle K_{nm}\rangle_T = 0$. Therefore, intuitively for the tunneling to be complex, K_{nm} must spend different amount of time being positive and negative, while averaging to 0.

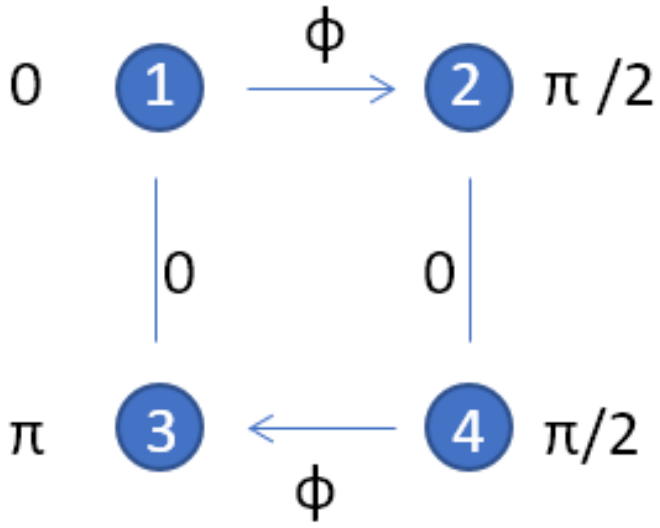

Figure 6.4: Schematics of a 4 site plaquette with artificial flux

Let's consider a simple case, where K_{nm} is either a positive constant or a negative constant:

$$K_{nm}(t) = \begin{cases} 1, & 0 < t/T < \epsilon \\ -\dfrac{\epsilon}{1-\epsilon}, & \epsilon < t/T < 1 \end{cases}. \tag{6.28}$$

The resulting tunneling is

$$\tilde{J}_{nm}/J_0 = \epsilon e^{i\alpha} + (1-\epsilon)e^{-i\frac{\epsilon}{1-\epsilon}\alpha}. \tag{6.29}$$

Experimentally this can be realized by pulsing f on for each site, making $F(t)$ a sawtooth, with various delays. The duty cycle is $\epsilon = (\phi_m - \phi_n)/2\pi$. See Fig. 6.3.

To realize artificial flux in a 4 site plaquette, consider the setting shown in Fig. 6.4. The phase of light pulse ϕ_n is labeled next to each site and the phase of tunneling is labeled next to each link. The dependence of the tunneling phase on α is shown in Fig. 6.5. This configuration can be extended into a 1D ladder horizontally, but extending into a 2D plane

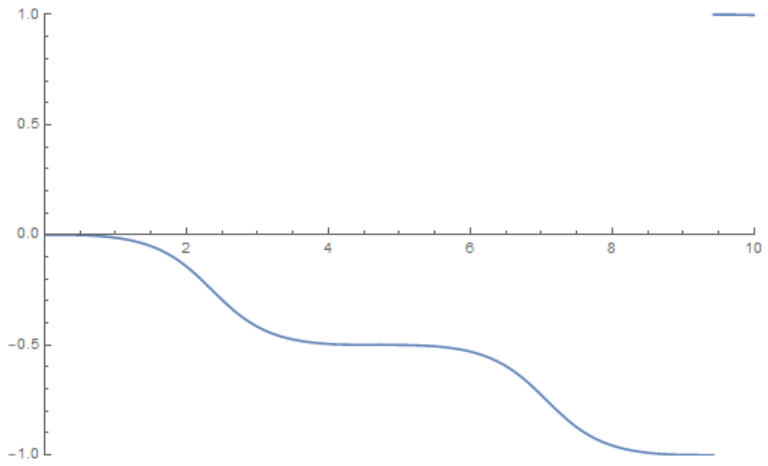

Figure 6.5: **Dependence of the tunneling phase on α.** Horizontal axis is modulation strength α. Vertical axis is tunneling phase divided by π.

with uniform flux is not straightforward.

Incidentally, since K_{nm} and thus the tunneling phase is an odd function in $\phi_m - \phi_n$, traveling wave modulation will never work, since opposing links will have the same tunneling phase, netting zero flux.

6.4 Rotating harmonic and Gaussian trap

Colioris force in a rotating frame simulates magnetic field felt by charged particles. Through rapid rotation near centrifugal limit, the ground state of a few body interacting atomic system transitions to highly correlated states. We would like to investigate the requirements for various experimental parameters for preparing such nontrivial states reliably. Most importantly we would like to calculate the ground state energy gap for various configurations, which determines the temperature requirement, as well as the time needed for adiabatic passage. Here we outline the steps for calculating the energy levels and show some preliminary numerical results. We will compare the cases with harmonic trap and Gaussian trap.

6.4.1 Theory and setup

For a given trap geometry, we formulate the many-body problem in terms of second quantization on the basis of single particle trap eigenstates. For exact treatment, all eigenstates must be included, which is numerically impossible since there are infinitely many of them. We must truncate the single particle Hilbert space to include only the 'most relevant' states, which we will discuss in detail for each specific trap geometry that we consider.

We label the included single particle eigenstates $|l\rangle$, each having wavefunction ψ_l and eigenenergy ϵ_l. The many-body Hamiltonian after second-quantization in the above basis is given by:

$$H = \sum_l (\epsilon_l - \mu) a_l^\dagger a_l + g \sum_{lkmn} V_{lkmn} a_l^\dagger a_k^\dagger a_m a_n, \tag{6.30}$$

where a_l destroys a (bosonic) particle in state $|l\rangle$, μ is the chemical potential, g is the interaction strength and V_{lkmn} describes the contact interaction between the states:

$$V_{lkmn} = \frac{1}{2} \int \psi_l^* \psi_k^* \psi_m \psi_n d^2 r \tag{6.31}$$

In order to inject angular momentum into the system we must introduce perturbation that breaks rotational symmetry. The easiest type of such perturbation is dipolar:

$$U = \lambda r \cos\theta, \tag{6.32}$$

written in polar coordinates, which is realized by moving the entire trap in a circle with radius $R = \lambda / m\Omega^2$ with frequency Ω. For reference, for $\lambda = 10$ kHz$/\mu m, \Omega = 100$ kHz, we have $R = 89$ nm. Such perturbation adds an additional term to the Hamiltonian:

$$H_1 = \lambda \sum_{mn} U_{mn} a_m^\dagger a_n T \tag{6.33}$$

$$U_{mn} = \int \psi_m^* U \psi_n d^2 r \tag{6.34}$$

We exactly diagonalize this Hamiltonian by writing it as a matrix in the Fock basis. As the Hamiltonian conserves particle number, we span our Hilbert space with Fock states with definite number of particles N. For example for $N = 4$, a Fock state

$$|\psi\rangle = |klmn\rangle \tag{6.35}$$

denotes a state where the four particles occupy single particle states labeled by k, l, m, n. If two labels are the same, the single particle state is occupied by two particles. Using this notation, the full Hilbert space considered is spanned by states with $k \leq l \leq m \leq n$. The dimension of this Hilbert space is roughly $O(M^N)$, where M is the number of included single particle eigenstates. The matrix elements $\langle k'l'm'n'|H|klmn\rangle$ are obtained from (6.30) according to bosonic operator algebra.

Harmonic trap

We start off with the well-studied case of harmonic trap. The single particle Hamiltonian is:

$$H_s = -\frac{1}{2}\partial^2 + \frac{1}{2}r^2 - \Omega \cdot L, \tag{6.36}$$

where the trap frequency ω is rescaled to be 1. The last term is due to rotation, at angular frequency $\Omega * \omega$.

In the ususal case where interaction is much smaller than trap frequency, we consider only the lowest landau level, with states given by:

$$\psi_l(z = x + iy) = (\pi l)^{-1/2} z^l e^{-|z|^2/2} \tag{6.37}$$

The energies are

$$\epsilon_l = (1-\Omega)l \tag{6.38}$$

The interaction matrix is

$$V_{lkmn} = \delta_{l+k-m-n} 2^{-(l+k+2)} \frac{(l+k)!}{\pi\sqrt{l!k!m!n!}} \tag{6.39}$$

The dipolar coupling is

$$U_{mn} = \delta_{m-n-1} \frac{(n+1)!}{\sqrt{2n!(n+1)!}} + \delta_{m-n+1} \frac{n!}{\sqrt{2n!(n-1)!}} \tag{6.40}$$

The interaction strength g is related to the 3D scattering length a and the harmonic oscillator length in the z-direction $l_z = \sqrt{\hbar/m\omega_\perp}$ by:

$$g = \sqrt{8\pi}a/l_z \tag{6.41}$$

For typical condition $a = 200a_B$ and $\omega_\perp = 2$ kHz, $l_z = 500$ nm, we have $g = 0.1$.

Since the Hamiltonian conserves angular momentum, many-particle states with different total angular momentum don't mix, and we can safely include single particle states only up to angular momentum $l_{\max}$. We can even truncate the many-body Hilbert space even further by including many-body states only up to total angular momentum $L_{\max}$. To see physics of the 1/2-Laughlin state, which has total angular momentum $L = N(N-1)$, we chose $l_{\max} = 2N + 2$ and $L_{\max} = N^2 + 8$.

Gaussian trap

Let's now turn to the Gaussian trap. The single particle Hamiltonian is:

$$H_s = -\partial^2 - \alpha e^{-r^2} - \Omega \cdot L \tag{6.42}$$

Here energy and frequency are in units of $\mathcal{E} = \hbar^2/4m\sigma^2$, σ is the 1-sigma width of the trap, and α is the trap depth. For Cesium with $\sigma = 1\ \mu m$, $\mathcal{E} = 120$ Hz, and λ is in units of $\mathcal{E}/\sqrt{2}\sigma = 85\ \text{Hz}/\mu m$. This time there is no analytic solution, but we can still numerically obtain the eigenstates. Since the Hamiltonian conserves angular momentum, we seek simultaneous eigenstates of both energy and angular momentum, satisfying the equation

$$-\partial_r^2\phi_l - \frac{1}{r}\partial_r\phi_l + \frac{l^2}{r^2}\phi_l - \alpha e^{-r^2/2\sigma^2}\phi_l = E\phi_l \tag{6.43}$$

$$\psi_l(r,\theta) = \phi_l(r)e^{-il\theta} \tag{6.44}$$

There is a subtlety in working with polar coordinates numerically, due to coordinate singularity at the origin. Instead of working with a grid $r_j = j\Delta r,\ \ j = 0, \cdots, r_{\max}/\Delta r$, we work with [67]

$$r_j = (j + 1/2)\Delta r,\ \ j = 0, \cdots, r_{\max}/\Delta r \tag{6.45}$$

with the condition $\phi(r_0) = \phi(r_{-1})$ due to its azimuthal symmetry.

Restricting to LLL in this case means taking the solution with smallest E for each $l \leq 0$. Denoting the solutions and eigenvalues ϕ_l and E_l, we have

$$\epsilon_l = E_l - \Omega l \tag{6.46}$$

$$V_{lkmn} = \frac{\delta_{l+k-m-n}}{2}\int_0^\infty \phi_l\phi_k\phi_m\phi_n 2\pi r dr \tag{6.47}$$

$$U_{mn} = \frac{\delta_{m-n-1} + \delta_{m-n+1}}{2}\int_0^\infty \phi_m\phi_n 2\pi r^2 dr \tag{6.48}$$

The interaction strength g is

$$g = \sqrt{32\pi}a/l_z \tag{6.49}$$

For typical condition $a = 200a_B$ and $\omega_\perp = 2$ kHz, $l_z = 500$ nm, we have $g = 0.2$.

There is a natural truncation of the single particle Hilbert space, as a finite sized trap

only supports a finite number of bound states $E_l < 0$. Discarding the free states is justified, because the interaction term couples states according to their spatial overlap, and free states occupy all of space while the bound states concentrate around the trap. Therefore the overlap between free and bound states is smaller than that between bound states by a factor of $\sim \sigma^2/A$, which is the ratio between the area of the trap and the area between traps. If the traps are distantly separated, the coupling is small, and the free states can be safely discarded. This observation is particuarly important, as the free states can have arbitrarily large angular momentum while only having energy slightly above 0, meaning their energy can quickly drop below that of the ground state for nonzero Ω. Intuitively the centrifugal force makes the area outside the trap anti-trapping, where these low energy states live, meaning they have small spatial overlap with the trap region.

In addition to discarding the free states, further truncation according to angular momentum can be performed, the same way as in the case of harmonic trap.

6.4.2 Numerical results

Harmonic trap

Shown in Fig. 6.6 is the numerical result for a harmonic trap, showing a sequence of ground state level crossings, due to different many body states having different interaction energy shift. To find an adiabatic passage sequence towards nontrivial ground states we need additional information about the widths of avoided level crossings in the presence of perturbation, similar to Fig. 6.7. Eventually we need to simulate the time dependent dynamics following the adiabatic sequence to find the optimum path and fidelity.

Gaussian trap

The situation with Gaussian trap is quite different from the harmonic trap case, as the anharmonicity breaks the degeneracy of the LLL at centrifugal limit. Instead, higher angular momentum state crosses the ground state sooner, as shown in Fig. 6.8. As a result the many particle spectrum is very different as well (Fig. 6.9). It is important to note that the first ground state crossings are between states composed of single particle levels with $l = 0$ and $l = 4$, which are coupled by dipolar perturbations through a fourth order process, making the coupling very small. Crossing between states with lower angular momentum occur later, but with a larger coupling. Therefore, by passing through the narrow avoided crossings quickly we can target level crossings at higher rotation frequency, avoiding transition to states with high angular momentum and lower energy.

As a side note, realistically all finitely deep traps are anharmonic, with higher angular momentum states having reduced energy. The above considerations provide justification for ignoring the effect of anharmonicity if it only starts to become important for very high angular momentum states, as the early ground state crossings will be very narrow, and transition at the crossings will be suppressed.

To identify an adiabatic passage sequence to a target state, again we need a plot like Fig. 6.7. Here it's technically more difficult as it's harder to tell which two states to calculate the gap between.

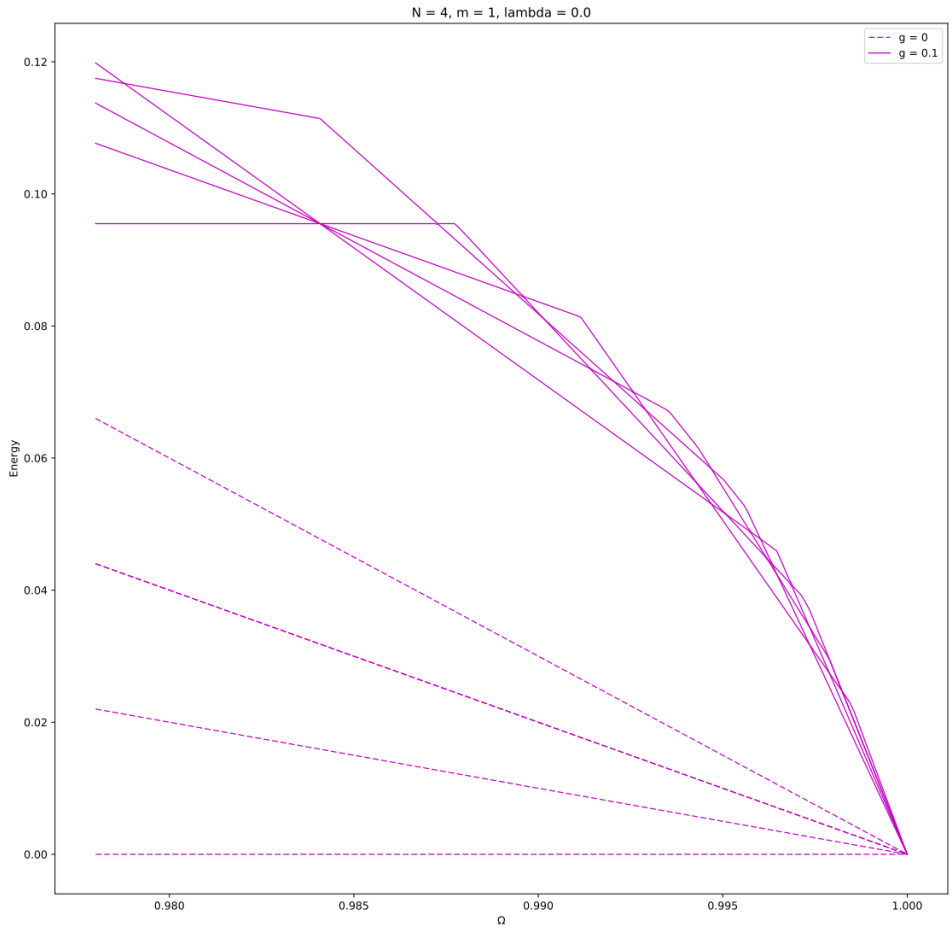

Figure 6.6: Lowest few energy levels versus rotation frequency for $N = 4$, with (solid line) and without (dashed line) interaction.

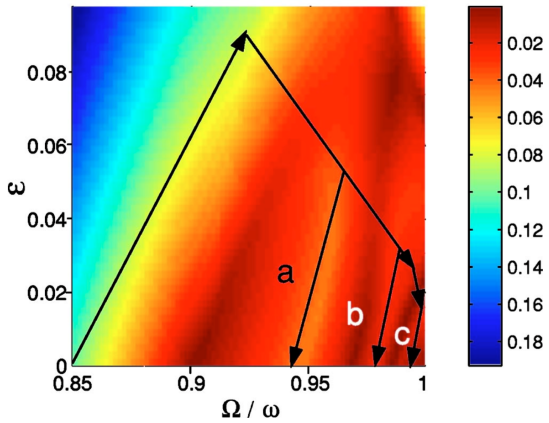

Figure 6.7: Map of ground state energy gap for various rotation frequency and perturbation strength. Reproduced from Fig 2 of PHYSICAL REVIEW A 70, 053612 (2004).

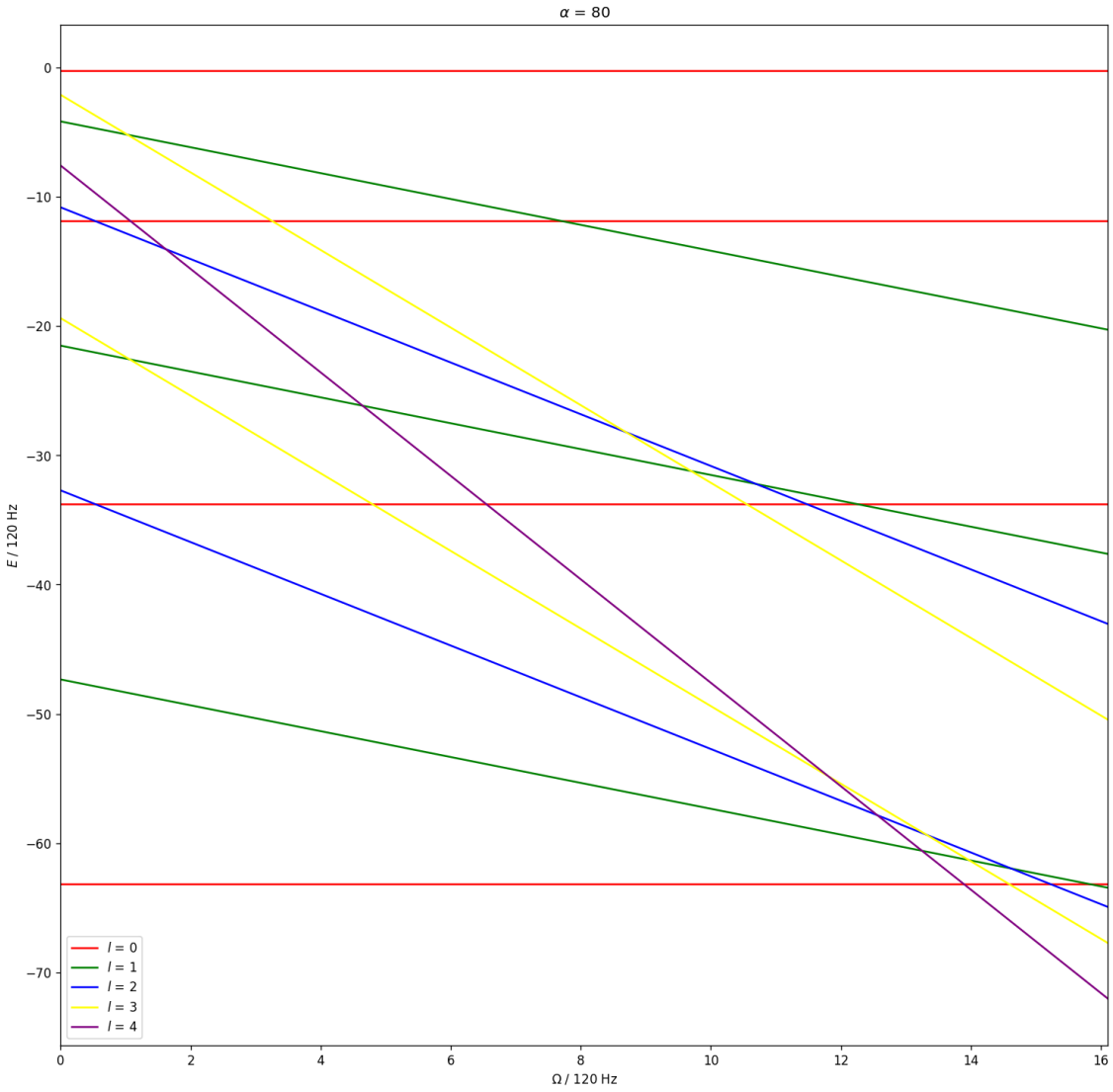

Figure 6.8: Single particle energy levels in a Gaussian trap with depth $\alpha = 80$. Anharmonicity causes states with higher angular momentum to cross with ground state sooner.

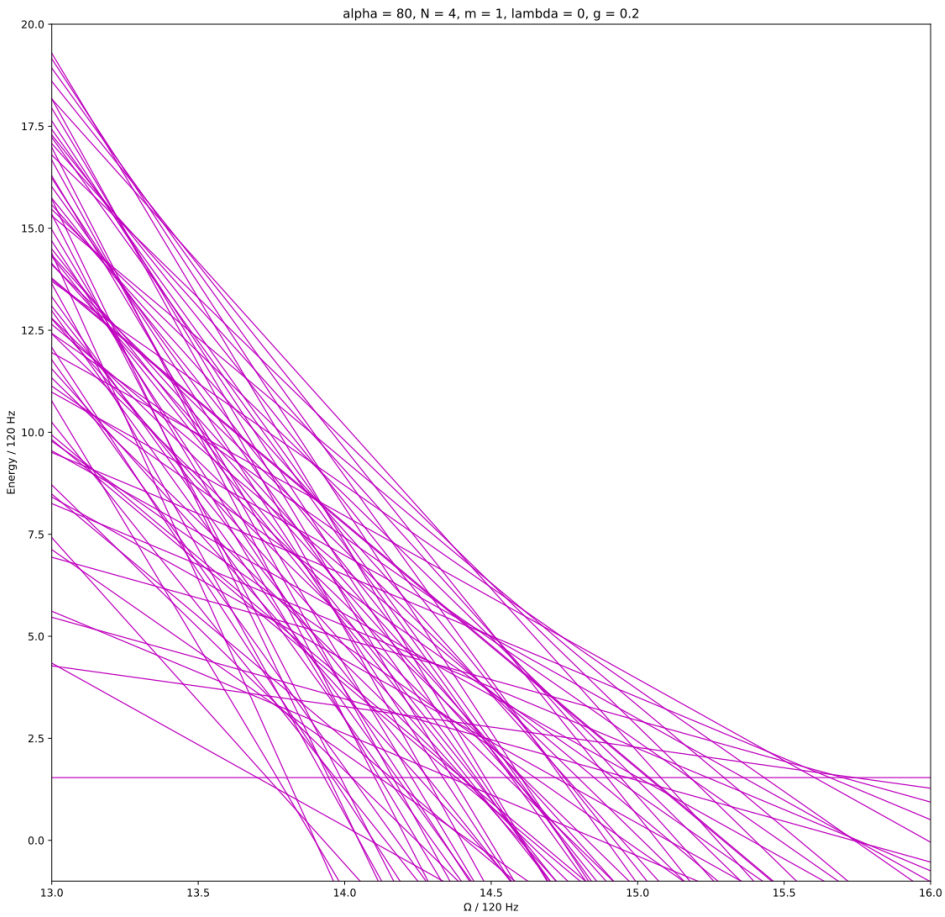

Figure 6.9: Many particle spectrum for $N = 4$ and $\alpha = 80$. Slopes of the lines indicate the total angular momentum for each many body state.

CHAPTER 7

OUTLOOK

7.1 Liquid-gas phase transition and vortex array from density-dependent gauge field

For the Bose-Einstein condensate subject to a density-dependent gauge field studied in chapter 4, theoretical and numerical investigations suggest that the system can exhibit a liquid-gas like phase transition under certain conditions, where the high and low density domains would be the liquid and gas phase, respectively. Moreover, the phase boundary (domain wall) can host an array of vortices, which is under certain conditions energetically favourable to having the domain wall perpendicular to the gauge field. In this section I present the theoretical and numerical study. Finding and realizing experimental parameters that allow us to observe these effects in the lab is an interesting future direction.

7.1.1 Introduction

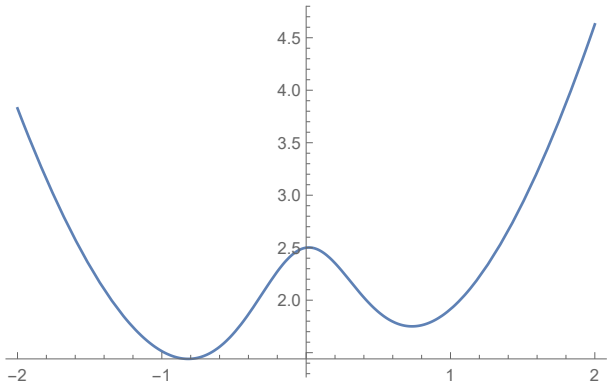

Figure 7.1: Tilted double well dispersion ε_k versus momentum k

Consider a condensate described by the mean field Hamiltonian

$$H = \sum_k \varepsilon_k |\psi_k|^2 + \frac{U}{2}|\psi|^4 + \frac{\eta}{2}|\psi|^2 \psi^* \vec{e} \cdot (-i\hbar\vec{\nabla})\psi \tag{7.1}$$

Here ψ is the condensate wavefunction. The first term is the kinetic energy with dispersion ε_k shown in Fig. 7.1. The dispersion exhibits two minima $\pm k_0$, and the two minima differ by an amount Δ. The second term is the interaction energy. The third term describes a density dependent gauge field $\vec{A} = \frac{\eta}{2}|\psi|^2\vec{e}$.

We'd like to consider the case where the density dependent gauge field causes the bias between the two minima to shift polarity when the density exceeds a critical value $n_c = \Delta/(2\eta)$, such that high and low density regions have opposite quasi-momentum. We are interested in whether droplets could form in this case.

7.1.2 Thermodynamic bulk treatment

Let's ignore surface effects for now. Suppose the gas has particle number N and occupies a volume V. Consider particles with quasi-momentum $\pm k_0$ as two different species, and assume each species have uniform density and do not spatially overlap. Let $N_1.V_1$ (N_2, V_2) be the particle number and volume of specie $+k_0$ $(-k_0)$, respectively. Then the total energy of the gas is given by

$$E = N_1\left(\frac{\eta}{2}n_1\right) + N_2\left(\Delta - \frac{\eta}{2}n_2\right) + \frac{U}{2}N_1 n_1 + \frac{U}{2}N_2 n_2, \tag{7.2}$$

where the first two terms are kinetic energy and the last two are interaction energy and $n_i = N_i/V_i$ are the densities.

We have constraints

$$N_1 + N_2 = N \tag{7.3}$$

$$V_1 + V_2 = V \tag{7.4}$$

Therefore we have

$$E = \frac{\eta}{2}\frac{N_1^2}{V_1} + (N - N_1)\left(\Delta - \frac{\eta}{2}\frac{N - N_1}{V - V_1}\right) + \frac{U}{2}N_1^2/V_1 + \frac{U}{2}\frac{(N - N_1)^2}{V - V_1}, \tag{7.5}$$

To minimize the energy, we have

$$\frac{\partial E}{\partial N_1} = \frac{\partial E}{\partial V_1} = 0 \tag{7.6}$$

The two equations reduce to

$$n_1 = \sqrt{\frac{U - \eta}{U + \eta}}n_2 \tag{7.7}$$

$$n_1 = \frac{\Delta}{U + \eta - \sqrt{U^2 - \eta^2}} \tag{7.8}$$

The constraints $N_1 + N_2 = N$ and $V_1 + V_2 = V$ can be rewritten as

$$n_2 = n_0 + (n_0 - n_1)\frac{\gamma}{1 - \gamma}, \tag{7.9}$$

where $n_0 = N/V$ and $\gamma = V_1/V$.

Eliminating n_1, n_2 from equations (7.7)(7.8)(7.9), we have

$$\gamma = \frac{\sqrt{1 + \alpha}}{\sqrt{1 + \alpha} - \sqrt{1 - \alpha}} - \frac{\sqrt{1 - \alpha}}{\sqrt{1 + \alpha} - \sqrt{1 - \alpha}}\frac{n_0 U}{\Delta}\left(1 + \alpha - \sqrt{1 - \alpha^2}\right), \tag{7.10}$$

where $\alpha = \eta/U$.

As γ is the fraction of volume occupied by specie $+k_0$, we can use it to characterize the phases of the gas. If $\gamma \geq 1$, the entire system is 'gaseous', having quasi-momentum $+k_0$ and density below critical density. If $\gamma \leq 0$, the entire system is 'liquid', having quasi-momentum $-k_0$ and density above critical density. If $0 < \gamma < 1$, the system is a mixture of 'liquid' and 'gas', with the 'gas' occupying a fraction γ of the volume. Plotting γ against α and

$\beta = n_c/n_0 = \Delta/(2\eta n_0)$ gives us the phase diagram shown in Fig. 7.2.

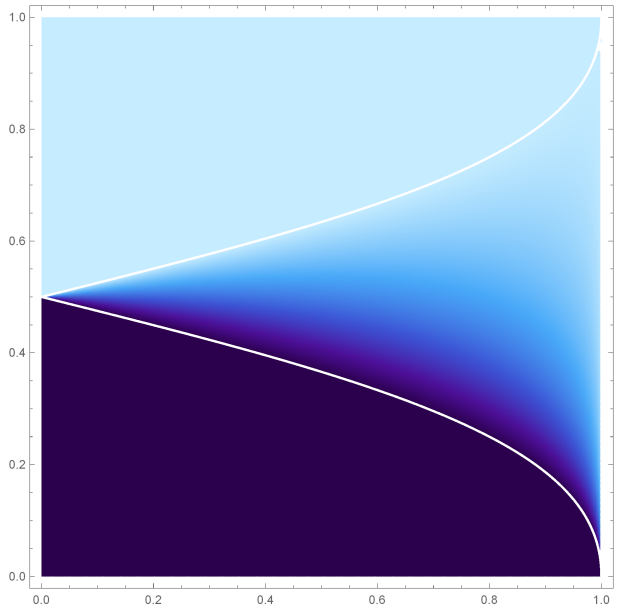

Figure 7.2: **Phase diagram of the liquid-gas transition.** The horizontal axis is α, the strength of the density-dependent gauge field. The vertical ais is β, the critical density over the mean density. The colorbar shows γ, the fraction of volume occupied by the 'gas' phase. We see a pure liquid phase (dark blue), a pure gas phase (light blue), and a coexistence phase in between. When $\alpha > 1$ the system is unstable and undergoes collapse.

The phase boundaries are given by

$$\beta_{c1} = \frac{1}{2}\left(1 + 1/\alpha - \sqrt{1/\alpha^2 - 1}\right) \tag{7.11}$$

$$\beta_{c2} = \frac{1}{2}\left(1 - 1/\alpha + \sqrt{1/\alpha^2 - 1}\right) \tag{7.12}$$

7.1.3 Equation of state and finite-pressure droplet

Consider the equation of state of the system, expressed in terms of the dependence of the chemical potential $\mu = \partial E/\partial N$ on the mean particle density $n = N/V$. From the previous section we can derive that

$$\mu = \begin{cases} (U+\eta)n, & 0 < n < \frac{\Delta}{U+\eta-\sqrt{U^2-\eta^2}} \\ \frac{\Delta(U+\eta)}{U+\eta-\sqrt{U^2-\eta^2}}, & \frac{\Delta}{U+\eta-\sqrt{U^2-\eta^2}} < n < \frac{\Delta}{\sqrt{U^2-\eta^2}-(U-\eta)} \\ (U-\eta)n+\Delta, & n > \frac{\Delta}{\sqrt{U^2-\eta^2}-(U-\eta)} \end{cases} \tag{7.13}$$

We can see that the chemical potential is constant in the liquid-gas mixture phase. Since the compressibility is given by $\beta = \frac{1}{n^2}\frac{\partial n}{\partial \mu}$, in the liquid-gas mixture phase the compressibility is infinite, meaning the pressure of the system stays constant when it is compressed. Therefore, in the liquid-gas phase we can consider the system to form finite-pressure droplets of liquid, surrounded by gas.

There is an alternative, more general way to derive the existence of the finite-pressure droplet. Consider an equation of state expressed as the energy density $\epsilon(n)$ as a function of particle density n. Consider the case where the system is composed of two regions with different density, region 1 with density n_1 and volume V_1, and region 2 with density n_2 and volume V_2. The total energy of the system is

$$E = \epsilon(n_1)V_1 + \epsilon(n_2)V_2, \tag{7.14}$$

subject to the constraints that $V_1 + V_2 = V$ and $n_1V_1 + n_2V_2 = n_0V$, where n_0 is the mean density of the whole system. The constraints can be solved,

$$V_1 = V\frac{n_2 - n_0}{n_2 - n_1} \tag{7.15}$$

$$V_2 = V\frac{n_0 - n_1}{n_2 - n_1} \tag{7.16}$$

Therefore the total energy is

$$\begin{aligned} E &= \epsilon(n_1)V\frac{n_2-n_0}{n_2-n_1} + \epsilon(n_2)V\frac{n_0-n_1}{n_2-n_1} \\ &= \tilde{\epsilon}(n_1,n_2,n_0)V \end{aligned} \tag{7.17}$$

with

$$\tilde{\epsilon}(n_1,n_2,n) = \epsilon(n_1)\frac{n_2-n}{n_2-n_1} + \epsilon(n_2)\frac{n-n_1}{n_2-n_1} \tag{7.18}$$

The result Eq. (7.17) means that the system can obtain a new energy density $\tilde{\epsilon}(n_1,n_2,n_0)$ at mean density n_0 by forming a mixture of domains with density n_1 and n_2. Upon closer inspection, the new energy density is on the line connecting $\epsilon(n_1)$ and $\epsilon(n_2)$, see Fig. 7.3. This means that if at any point the equation of state curve $\epsilon(n)$ is non-convex, one can draw a line connecting two points on the curve that lies under the curve itself, which means lowering energy by forming domains. Furthermore, the linear nature of the equation of state implies constant chemical potential and infinite compressibility, meaning that the domains are finite-pressure droplets. The chemical potential plot $\mu(n)$ is counter-intuitive since the system does not transition to the red species as soon as the chemical potential line crosses the blue species. Rather, the formation of droplets can be intuitively seen from the equation of state plot $\epsilon(n)$.

The results of the previous section can be readily derived by drawing a tangent line to the bare equations of state of the two species, $\epsilon_1(n) = (U+\eta)n^2/2$, $\epsilon_2(n) = (U-\eta)n^2/2 + \Delta n$. More generally, beyond our simple two species model, as long as the bare equation of state of any system develops a non-convex section, the system can support finite pressure droplets.

This derivation does not consider the energy cost of droplet surfaces. To observe the droplets in an experiment, the surface energy must be paid by the energy gain from droplet formation in the bulk, which is the difference between the magenta and red dot at density

n_0 in Fig. 7.3. Since the surface energy scales as the system size L whereas the bulk energy scales as L^2, going to larger system size is favorable. In our previous experiment, the system size is primarily limited by the parasitic harmonic trapping from the optical lattice. An anti-harmonic compensation projected by the DMD can help combat this effect. A less tight harmonic trap also allows for a lower chemical potential, which is also favorable in reducing surface energy.

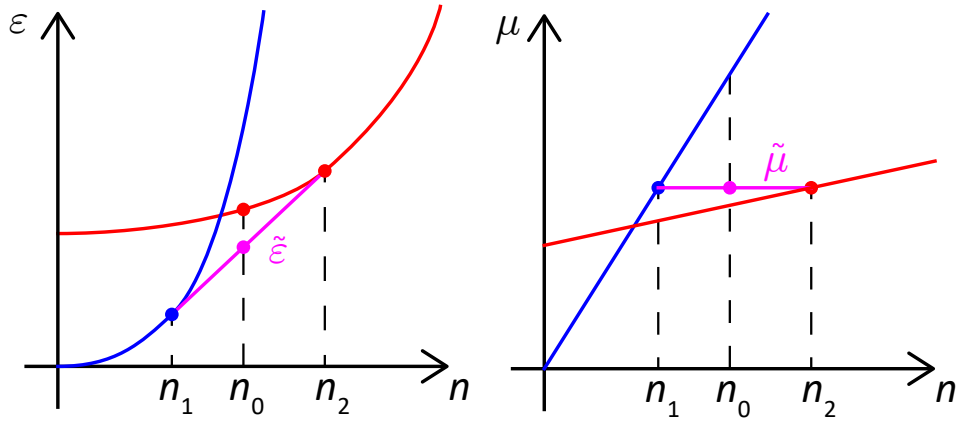

Figure 7.3: **Non-convex equation of state leads to finite-pressure droplets.** If the equation of state $\epsilon(n)$ (red and blue) is non-convex between n_1 (blue dot) and n_2 (red dot), the system can lower its energy density to $\tilde{\epsilon}$ (magenta) by forming a mixture of domains with density n_1 and n_2 (magenta dot). The chemical potential μ is constant in the mixture phase ($\tilde{\mu}$, indicating that the domains are finite-pressure droplets.

7.1.4 Simulation

We can derive a GPE from the mean-field Hamiltonian as shown in section 3.4.2, and use imaginary time evolution to numerically find the ground state. An example is shown in Fig. 7.4. Here Eq (7.10) predicts a gas fraction of 96%, but simulation gives about 45%. This is understandable, because the gas is not really uniform inside the box because of the dispersion, and the effective volume is smaller, meaning the actual β is smaller. A smaller β

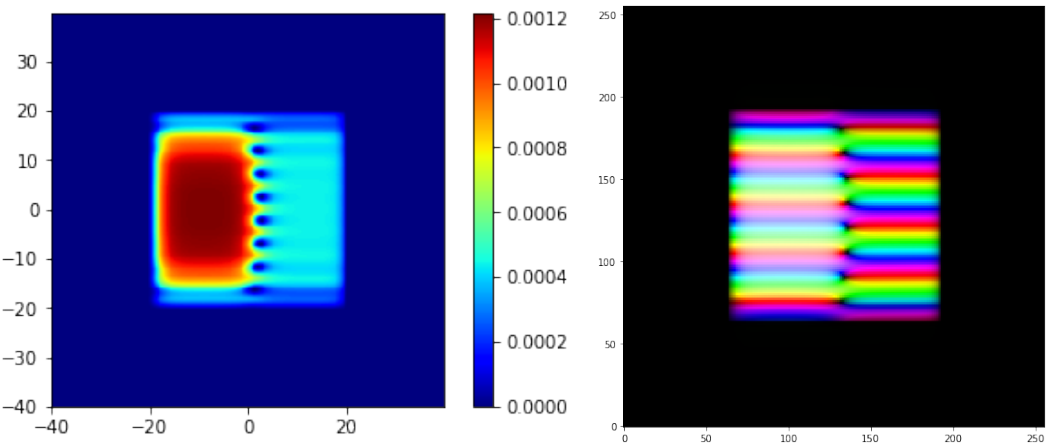

Figure 7.4: **GPE simulation of density-dependent gauge field induced roplet.** Here $\alpha = 0.999, \beta = 0.8, Un_0 = 4E_R$. Left is density profile; right is phase profile. The box is $\pm 20 \times 532$ nm in both directions.

is indeed predicted to result in a smaller gas fraction.

From the simulation, it is apparent that the contribution from the surface is never negligible, because the boundary between the 'liquid' and 'gas' is formed by an array of vortices, and they cost a lot of energy. For this reason, actual numbers of k_0 and Un_0 changes the condition for droplet formation. We can map this dependence out more carefully with the numerical simulation.

7.2 Squeezing edge states of a Floquet topological insulator

Topological insulators have attracted the interest of condensed matter physicsts for more than a decade, and the study of the topological physics is a major goal of quantum simulation with ultracold atoms. Ultracold atomic platforms like ours offer greater degree of control and more detailed detection compared to solid state systems. A standing challenge in this direction is the excitation and detection of edge states, which result from the bulk-boundary correspondence, a cornerstone result in topological physics. Unlike solid state systems where the edge states can be populated with electrons in the nearby Fermi sea and detected with resistive measurements, in ultracold atoms it is difficult to populate these excited states with

bosons, and to reach sufficiently low temperatures with fermions.

In this section, I describe a proposal to overcome this challenge utilizing Bose fireworks, which populates excited states with squeezed pairs of atoms excited by interaction modulation. I describe a framework that predicts the squeezing dynamics in a general basis of states (rather than the plane wave basis like in the previous chapters). To create a Floquet-topological insulator that supports edge states in our system, we may follow the proposal [68; 69] which employs resonant shaking of a 1D lattice. Sharp edges in the system can be created with walls projected through the DMD.

7.2.1 Bose fireworks in general basis

Consider a system with single particle Hamiltonian H_0, with single particle eigenstates $|\psi_i\rangle$ and eigenenergies E_i. The second quantized Hamiltonian of the system is then

$$\mathcal{H}_0 = \sum_i E_i a_i^\dagger a_i, \tag{7.19}$$

where a_i is the annihilation operator of a boson in state $|\psi_i\rangle$. Now let's turn on interparticle interaction, in particular a contact interaction like that found in our experiment. The interaction Hamiltonian is

$$\mathcal{H}_1 = \frac{g}{2}\int dx\ a(x)^\dagger a(x)^\dagger a(x) a(x). \tag{7.20}$$

The local bosonic annihilation operator $a(x)$ is related to the eigenstate annihilation operator as

$$a(x) = \sum_i \psi_i^*(x) a_i, \tag{7.21}$$

where $\psi_i(x)$ is the spatial wavefunction of state $|\psi_i\rangle$. The total Hamiltonian is then

$$\mathcal{H} = \sum_i E_i a_i^\dagger a_i + \frac{g}{2} \sum_{ijkl} F_{ij,kl} a_i^\dagger a_j^\dagger a_k a_l, \tag{7.22}$$

where $F_{ij,kl} = \int dx\ \psi_i(x)\psi_j(x)\psi_k^*(x)\psi_l^*(x)$.

Now lets consider that there is a BEC in the state $|\psi_0\rangle$ with particle number N, and employ Bogoliubov approximation. The Hamiltonian becomes

$$\mathcal{H} = \sum_i E_i a_i^\dagger a_i + \frac{g}{2} \sum_{ij} N(F_{ij,00} a_i^\dagger a_j^\dagger + F_{00,ij} a_i a_j + 4F_{i0,j0} a_i^\dagger a_j). \tag{7.23}$$

Under periodic driving $g(t) = \gamma \cos \omega t$, we can repeat the treatment in section 3.2, and arrive at the RWA Hamiltonian

$$\mathcal{H} = \sum_i (E_i - \frac{\hbar\omega}{2}) a_i^\dagger a_i + \frac{\gamma N}{2} \sum_{ij} (F_{ij,00} a_i^\dagger a_j^\dagger + F_{00,ij} a_i a_j). \tag{7.24}$$

We can see that it is formally the same as the fireworks system we considered before, except that now all the modes are generally coupled together, rather than separated into independent pairs. Still, one can define a new basis to diagonalize the quadratic Hamiltonian, and we conclude that the resulting dynamics is squeezing of the near resonant excited states.

In the context of Floquet-topological edge states, since the edge states live in a gap, as long as the driving strength is small compared to the band gap, only the edge states will have exponentially growing population, and the bulk states in the bands are far enough off-resonant to not be excited. Therefore, we can selectively populate the edge states, if we start from a BEC and periodically modulate the interaction.

In terms of detection, generally in the absence of edge states the eigenstates are delocalized bulk states in the band, which are localized in momentum space. If we perform imaging after time-of-flight, or focused time-of-flight, we would see localized peaks in each Brillouin

zone. On the other hand, the edge states are localized in real space on the edges, and thus delocalized in momentum space. We would see a smeared background of atoms in the entire Brillouin zone. This can be potentially a clear signature of population of the edge states.

7.2.2 Creating topological edge states with shaken 1D lattice

Shaken lattices has long been regarded as one of the most feasible ways to create Floquet-topological insulators with ultracold atom quantum simulators. A detailed study was given in [68], where among other schemes it was proposed that resonantly shaking the 1D lattice with a 'two photon' transition (shaking at half the resonance frequency) results in a topologically nontrivial band. The system could be effectively described with the Su–Schrieffer–Heeger model. The paper also discussed in detail how to characterize the Zak phase, the 1D 'topological invariant', as well as how to numerically predict edge states in a finite system. A more detailed investigation of this shaking scheme was given in [69], which described the system in terms of a Creutz ladder, with more intuitive pictures of what makes the system topological. These references are a great starting point to investigate the feasibility to realizing a Floquet-topological insulator in our shaken lattice system.

REFERENCES

[1] J. R. Abo-Shaeer, C. Raman, J. M. Vogels, and W. Ketterle. Observation of vortex lattices in Bose-Einstein condensates. *Science*, 292(5516):476–479, 2001.

[2] M. Aidelsburger, M. Atala, M. Lohse, J. T. Barreiro, B. Paredes, and I. Bloch. Realization of the Hofstadter hamiltonian with ultracold atoms in optical lattices. *Phys. Rev. Lett.*, 111:185301, 2013.

[3] C. Schweizer, F. Grusdt, M. Berngruber, L. Barbiero, E. Demler, N. Goldman, I. Bloch, and M. Aidelsburger. Floquet approach to $\mathbb{Z}_2$ lattice gauge theories with ultracold atoms in optical lattices. *Nature Physics*, 15(11):1168–1173, 2019.

[4] N. Navon, A. L. Gaunt, R. P. Smith, and Z. Hadzibabic. Emergence of a turbulent cascade in a quantum gas. *Nature*, 539(7627):72–75, 2016.

[5] C. J. Pethick and H. Smith. *Bose–Einstein condensation in dilute gases*. Cambridge university press, 2008.

[6] L. W. Clark. *Quantum many-body dynamics with driven Bose condensates: Kibble-Zurek mechanism and Bose fireworks*. The University of Chicago, 2017.

[7] C. Chin, R. Grimm, P. Julienne, and E. Tiesinga. Feshbach resonances in ultracold gases. *Reviews of Modern Physics*, 82(2):1225, 2010.

[8] X. Zhang. *Observation of quantum criticality with ultracold atoms in optical lattices*. The University of Chicago, 2012.

[9] G. Reinaudi, T. Lahaye, Z. Wang, and D. Guéry-Odelin. Strong saturation absorption imaging of dense clouds of ultracold atoms. *Optics letters*, 32(21):3143–3145, 2007.

[10] C.-L. Hung, X. Zhang, L.-C. Ha, S.-K. Tung, N. Gemelke, and C. Chin. Extracting density–density correlations from in situ images of atomic quantum gases. *New Journal of Physics*, 13(7):075019, 2011.

[11] C.-A. Chen, S. Khlebnikov, and C.-L. Hung. Observation of quasiparticle pair production and quantum entanglement in atomic quantum gases quenched to an attractive interaction. *Physical Review Letters*, 127(6):060404, 2021.

[12] Z. Zhang, K.-X. Yao, L. Feng, J. Hu, and C. Chin. Pattern formation in a driven Bose–Einstein condensate. *Nature Physics*, 16(6):652–656, 2020.

[13] L. Feng, J. Hu, L. W. Clark, and C. Chin. Correlations in high-harmonic generation of matter-wave jets revealed by pattern recognition. *Science*, 363(6426):521–524, 2019.

[14] P. Van Loock and A. Furusawa. Detecting genuine multipartite continuous-variable entanglement. *Physical Review A*, 67(5):052315, 2003.

[15] N. R. Cooper, J. Dalibard, and I. B. Spielman. Topological bands for ultracold atoms. *Rev. Mod. Phys.*, 91:015005, 2019.

[16] A. Eckardt and E. Anisimovas. High-frequency approximation for periodically driven quantum systems from a Floquet-space perspective. *New journal of physics*, 17(9): 093039, 2015.

[17] L. W. Clark, A. Gaj, L. Feng, and C. Chin. Collective emission of matter-wave jets from driven Bose–Einstein condensates. *Nature*, 551(7680):356–359, 2017.

[18] J. Hu, L. Feng, Z. Zhang, and C. Chin. Quantum simulation of Unruh radiation. *Nature Physics*, 15(8):785–789, 2019.

[19] H. Fu, L. Feng, B. M. Anderson, L. W. Clark, J. Hu, J. W. Andrade, C. Chin, and K. Levin. Density waves and jet emission asymmetry in Bose fireworks. *Physical review letters*, 121(24):243001, 2018.

[20] Y.-Y. Chen, P. Zhang, W. Zheng, Z. Wu, and H. Zhai. Many-body echo. *Physical Review A*, 102(1):011301, 2020.

[21] C. Lyu, C. Lv, and Q. Zhou. Geometrizing quantum dynamics of a Bose-Einstein condensate. *Physical Review Letters*, 125(25):253401, 2020.

[22] J. Maldacena. Eternal black holes in anti-de Sitter. *Journal of High Energy Physics*, 2003(04):021, 2003.

[23] P. Hosur, X.-L. Qi, D. A. Roberts, and B. Yoshida. Chaos in quantum channels. *Journal of High Energy Physics*, 2016(2):1–49, 2016.

[24] C. Yang, K. Chan, R. Harper, W. Huang, T. Evans, J. Hwang, B. Hensen, A. Laucht, T. Tanttu, F. Hudson, et al. Silicon qubit fidelities approaching incoherent noise limits via pulse engineering. *Nature Electronics*, 2(4):151–158, 2019.

[25] M. Mueller, R. S. Said, F. Jelezko, T. Calarco, and S. Montangero. One decade of quantum optimal control in the chopped random basis. *Reports on Progress in Physics*, 2022.

[26] A. Paszke, S. Gross, S. Chintala, G. Chanan, E. Yang, Z. DeVito, Z. Lin, A. Desmaison, L. Antiga, and A. Lerer. Automatic differentiation in pytorch. 2017.

[27] J. Bradbury, R. Frostig, P. Hawkins, M. J. Johnson, C. Leary, D. Maclaurin, G. Necula, A. Paszke, J. VanderPlas, S. Wanderman-Milne, et al. JAX: composable transformations of Python+ NumPy programs. *Version 0.2*, 5:14–24, 2018.

[28] H. Fu, Z. Zhang, K.-X. Yao, L. Feng, J. Yoo, L. W. Clark, K. Levin, and C. Chin. Jet substructure in fireworks emission from nonuniform and rotating Bose-Einstein condensates. *Physical Review Letters*, 125(18):183003, 2020.

[29] X.-B. Wang, T. Hiroshima, A. Tomita, and M. Hayashi. Quantum information with Gaussian states. *Physics Reports*, 448(1):1–111, 2007.

[30] T. R. Taha and M. I. Ablowitz. Analytical and numerical aspects of certain nonlinear evolution equations. II. Numerical, nonlinear Schrödinger equation. *Journal of Computational Physics*, 55(2):203–230, 1984.

[31] J. Javanainen and J. Ruostekoski. Symbolic calculation in development of algorithms: split-step methods for the Gross–Pitaevskii equation. *Journal of Physics A: Mathematical and General*, 39(12):L179, 2006.

[32] A. Sinatra, C. Lobo, and Y. Castin. The truncated Wigner method for Bose-condensed gases: limits of validity and applications. *Journal of Physics B: Atomic, Molecular and Optical Physics*, 35(17):3599, 2002.

[33] D. Griffiths. *Introduction to elementary particles*. 2008.

[34] H. L. Stormer, D. C. Tsui, and A. C. Gossard. The fractional quantum Hall effect. *Rev. Mod. Phys.*, 71:S298–S305, 1999.

[35] K.-X. Yao, Z. Zhang, and C. Chin. Domain-wall dynamics in Bose–Einstein condensates with synthetic gauge fields. *Nature*, 602(7895):68–72, 2022.

[36] J. B. Kogut. An introduction to lattice gauge theory and spin systems. *Rev. Mod. Phys.*, 51:659–713, 1979.

[37] K. G. Wilson. Confinement of quarks. *Phys. Rev. D*, 10:2445–2459, 1974.

[38] M. G. Alford, A. Schmitt, K. Rajagopal, and T. Schäfer. Color superconductivity in dense quark matter. *Rev. Mod. Phys.*, 80:1455–1515, 2008.

[39] M. Troyer and U.-J. Wiese. Computational complexity and fundamental limitations to fermionic quantum Monte Carlo simulations. *Phys. Rev. Lett.*, 94:170201, 2005.

[40] N. Goldman, G. Juzeliūnas, P. Öhberg, and I. B. Spielman. Light-induced gauge fields for ultracold atoms. *Reports on Progress in Physics*, 77(12):126401, 2014.

[41] E. Zohar, J. I. Cirac, and B. Reznik. Quantum simulations of lattice gauge theories using ultracold atoms in optical lattices. *Reports on Progress in Physics*, 79(1):014401, 2015.

[42] Y. Lin, R. Compton, K. Jiménez-García, J. V. Porto, and I. B. Spielman. Synthetic magnetic fields for ultracold neutral atoms. *Nature*, 462:628, 2009.

[43] G. Jotzu, M. Messer, R. Desbuquois, M. Lebrat, T. Uehlinger, D. Greif, and T. Esslinger. Experimental realization of the topological Haldane model with ultracold fermions. *Nature*, 515(7526):237–240, 2014.

[44] H. Miyake, G. A. Siviloglou, C. J. Kennedy, W. C. Burton, and W. Ketterle. Realizing the Harper hamiltonian with laser-assisted tunneling in optical lattices. *Phys. Rev. Lett.*, 111:185302, 2013.

[45] G. Baskaran and P. W. Anderson. Gauge theory of high-temperature superconductors and strongly correlated fermi systems. *Phys. Rev. B*, 37:580–583, 1988.

[46] T.-P. Cheng and L.-F. Li. *Gauge theory of elementary particle physics*. Oxford university press, 1994.

[47] M. Levin and X.-G. Wen. Colloquium: Photons and electrons as emergent phenomena. *Rev. Mod. Phys.*, 77:871–879, 2005.

[48] U.-J. Wiese. Ultracold quantum gases and lattice systems: quantum simulation of lattice gauge theories. *Annalen der Physik*, 525(10-11):777–796, 2013.

[49] L. Savary and L. Balents. Quantum spin liquids: a review. *Reports on Progress in Physics*, 80(1):016502, 2016.

[50] L. W. Clark, B. M. Anderson, L. Feng, A. Gaj, K. Levin, and C. Chin. Observation of density-dependent gauge fields in a Bose-Einstein condensate based on micromotion control in a shaken two-dimensional lattice. *Phys. Rev. Lett.*, 121:030402, 2018.

[51] F. Görg, K. Sandholzer, J. Minguzzi, R. Desbuquois, M. Messer, and T. Esslinger. Realization of density-dependent Peierls phases to engineer quantized gauge fields coupled to ultracold matter. *Nature Physics*, 15(11):1161–1167, 2019.

[52] V. Lienhard, P. Scholl, S. Weber, D. Barredo, S. de Léséleuc, R. Bai, N. Lang, M. Fleischhauer, H. P. Büchler, T. Lahaye, and A. Browaeys. Realization of a density-dependent peierls phase in a synthetic, spin-orbit coupled rydberg system. *Phys. Rev. X*, 10:021031, 2020.

[53] M. J. Edmonds, M. Valiente, G. Juzeliūnas, L. Santos, and P. Öhberg. Simulating an interacting gauge theory with ultracold Bose gases. *Phys. Rev. Lett.*, 110:085301, 2013.

[54] B. Yang, H. Sun, R. Ott, H.-Y. Wang, T. V. Zache, J. C. Halimeh, Z.-S. Yuan, P. Hauke, and J.-W. Pan. Observation of gauge invariance in a 71-site Bose–Hubbard quantum simulator. *Nature*, 587(7834):392–396, 2020.

[55] A. Mil, T. V. Zache, A. Hegde, A. Xia, R. P. Bhatt, M. K. Oberthaler, P. Hauke, J. Berges, and F. Jendrzejewski. A scalable realization of local U(1) gauge invariance in cold atomic mixtures. *Science*, 367(6482):1128–1130, 2020.

[56] T. Liu, L. W. Clark, and C. Chin. Exotic domain walls in Bose-Einstein condensates with double-well dispersion. *Phys. Rev. A*, 94:063646, 2016.

[57] A. Eckardt. Colloquium: Atomic quantum gases in periodically driven optical lattices. *Rev. Mod. Phys.*, 89:011004, 2017.

[58] J. Struck, C. Ölschläger, M. Weinberg, P. Hauke, J. Simonet, A. Eckardt, M. Lewenstein, K. Sengstock, and P. Windpassinger. Tunable gauge potential for neutral and spinless particles in driven optical lattices. *Phys. Rev. Lett.*, 108:225304, 2012.

[59] I. Shvarchuck, C. Buggle, D. S. Petrov, K. Dieckmann, M. Zielonkowski, M. Kemmann, T. G. Tiecke, W. von Klitzing, G. V. Shlyapnikov, and J. T. M. Walraven. Bose-Einstein condensation into nonequilibrium states studied by condensate focusing. *Phys. Rev. Lett.*, 89:270404, 2002.

[60] L. W. Clark, L. Feng, and C. Chin. Universal space-time scaling symmetry in the dynamics of bosons across a quantum phase transition. *Science*, 354(6312):606–610, 2016.

[61] C. V. Parker, L.-C. Ha, and C. Chin. Direct observation of effective ferromagnetic domains of cold atoms in a shaken optical lattice. *Nature Physics*, 9(12):769–774, 2013.

[62] N. D. Mermin. The topological theory of defects in ordered media. *Rev. Mod. Phys.*, 51:591–648, 1979.

[63] V. A. Gani, A. E. Kudryavtsev, and M. A. Lizunova. Kink interactions in the $(1+1)$-dimensional φ^6 model. *Phys. Rev. D*, 89:125009, 2014.

[64] A. Vilenkin. Cosmic strings and domain walls. *Physics Reports*, 121(5):263–315, 1985.

[65] L. Barbiero, C. Schweizer, M. Aidelsburger, E. Demler, N. Goldman, and F. Grusdt. Coupling ultracold matter to dynamical gauge fields in optical lattices: From flux attachment to $\mathbb{Z}_2$ lattice gauge theories. *Science advances*, 5(10):eaav7444, 2019.

[66] M. McDonald, J. Trisnadi, K.-X. Yao, and C. Chin. Superresolution microscopy of cold atoms in an optical lattice. *Physical Review X*, 9(2):021001, 2019.

[67] K. Mohseni and T. Colonius. Numerical treatment of polar coordinate singularities. *Journal of Computational Physics*, 157(2):787–795, 2000.

[68] W. Zheng and H. Zhai. Floquet topological states in shaking optical lattices. *Physical Review A*, 89(6):061603, 2014.

[69] J. H. Kang, J. H. Han, and Y.-i. Shin. Topological Creutz ladder in a resonantly shaken 1D optical lattice. *arXiv preprint arXiv:1902.10304*, 2019.